博士論文

Analysis of planetary fluid images considering local rotation
(局所回転を考慮した新たな惑星流体画像解析)

武藤　圭史朗

Analysis of planetary fluid images considering local rotation

(局所回転を考慮した新たな惑星流体画像解析)

東京大学大学院新領域創成科学研究科

複雑理工学専攻

Department of Complexity Science and Engineering
Graduate School of Frontier Sciences
The University of Tokyo

武藤　圭史朗

Keishiro Muto

Abstract

Planetary motion in the atmosphere occurs simultaneously on various scales in time and space. Movement at each scale is not independent; movement at a smaller scale affects movement at a larger scale, and vice versa. When trying to understand the motion of the planetary atmosphere, it is important to understand not only the motion of the atmosphere on a large scale but also the motion on a smaller scale.

Cloud tracking has been used to measure motions of planetary atmospheres remotely without direct observations. Cloud tracking is a method to track the movements of cloud parcels using temporally-continuous cloud images to obtain cloud motion vectors. Since it is considered in most of the cases that clouds move at the same speed and the same direction as the surrounding atmosphere, the wind direction and wind velocity can be obtained by tracking the movement of clouds. This method has been used to measure the motion of other planets, such as Venus and Jupiter, where direct observation is difficult as well as that of the Earth's atmosphere.

Cloud tracking has been performed by two types of cloud tracking methods: cross correlation method and phase correlation method. In each method, only the parallel movement of the characteristic pattern is assumed, and the rotation, of the characteristic pattern cannot be detected. In the actual atmospheric motion of planets, there are rotational movements of characteristic patterns and expansion and contraction of characteristic patterns of clouds due to updrafts and downdrafts, and it is important to track these movements. In this study, I improved the cloud tracking algorithm used so far and developed a new algorithm to track the clouds of the planet using the rotation invariant phase-only correlation method. In this method, the tracking region is Fourier-transformed before applying the phase correlation method for measuring parallel movement, and logarithmic polar coordinate conversion is performed to the amplitude spectra so that the rotation and enlargement/reduction motions can be obtained as parallel movements. With this rotation invariant phase-only correlation method, not only the parallel movement but also the rotational movement of the characteristic pattern can be detected at the same time.

When detecting the rotational motion of the atmosphere based on cloud tracking, the procedure was to calculate the vorticity from the wind speed field obtained by cloud tracking assuming parallel movement. Therefore, the required spatial scale is larger than the tracking region. In addition, if the tracking region is made small to measure the motion on a small spatial scale, there is a problem that the characteristic pattern that can be tracked in the tracking region is scarce and cloud tracking cannot be performed. However, by using the method used in this study, it is possible to measure

the rotation on the same spatial scale as the tracking region.

The accuracy of cloud tracking is about 1 pixel in any of the cross correlation method, the phase correlation method, and the rotation invariant phase-correlation method, and it is usually not possible to estimate the amount of movement in subpixel units. In order to measure atmospheric motion with a small spatial scale, it is considered that there is a large error in the unit of one pixel and no significant fluctuation can be obtained. In this study, I performed sub-pixel estimation by increasing the number of data points using upsampling. Thereby, the number of data points near the local maximum value on the correlation surface increases, and the local maximum position can be obtained with high accuracy.

I performed the newly-developed method to a simulated image pair. In this study, the rotation rate of the cloud pattern and the vorticity derived from the velocity field were calculated in the three case where the velocity field is solid body rotation, irrotational vortex, and sinusoidal velocity field in the latitude and longitude directions. As a result, in the case of a solid body rotation, the wind speed field and the rotation angle were determined correctly. Large-scale rotations can be measured more accurately by the new method than by the calculation of vorticity from the cloud-tracked velocity. However, if the velocity field includes vortex-like structures, the rotation rates at those vortices can be relatively well retrieved even if the spatial scale is smaller than the tracking region. When the scale of the velocity structure is decreased, the number of missing cloud tracking vectors increases, and thus the spatial pattern of the vorticity becomes difficult to obtain. Even in this case, however, the spatial pattern of the rotation rate can be relatively well retrieved although its amplitude is underestimated.

The new method was applied to Jupiter and Venus images based on the results above. For Jupiter, many small eddies were found to be distributed in the equatorial region. The spatial scales and the strengths of the eddies resemble those seen in the numerical simulation by Schneider and Liu (2009). It is considered that the observed vortex chains are involved in the formation of Jupiter's equatorial jet.

For Venus, though small-scale eddies are less prominent, a planetary-scale distribution of the rotation rate with a north-south reflection symmetry was seen, such that anti-clockwise rotation occurs in the northern hemisphere and clockwise rotation in the southern hemisphere. Since the large-scale rotation pattern is consistent with the latitudinal shear of the mean zonal wind, the result means that the rotation of small-scale clouds is caused by the large-scale wind. This result suggests that the small-scale streaky features at mid-latitudes, whose origin is poorly understood, are created by the deformation of clouds by large-scale winds.

The amplitude of the rotational velocity of the small vortices observed in this study is larger in Jupiter than in Venus, which is considered to be due to the difference in the Coriolis parameter (rotation rate) and whether the convective layer reaches the cloud top.

The newly-developed method has extracted even smaller scale eddies than previous studies, thereby extending the spectral coverage. The method has enabled investigation of the interaction between different scales in a wider wavelength range. The method would also enable studies of mesoscale weather systems such as deep convection and also studies of upward energy cascade from small-scale convective storms to planetary scale motions in planetary atmospheres.

Contents

1. Introduction

1.1 Importance of cloud tracking

Atmospheric motions and the associated momentum transport occur at various scales in time and space in planetary atmospheres (Figure 1). The motions at different scales are not independent with each other: small-scale motions affect large-scale motions, and vice versa. In order to understand the atmospheric dynamics, it is important to understand atmospheric motions not only at large scales but also at small scales.

Cloud tracking has been used to measure motions of planetary atmospheres remotely without direct observations. Cloud tracking is a method to track the movements of cloud parcels using temporally-continuous cloud images to obtain cloud motion vectors. Since it is considered in most of the cases that clouds move at the same speed and the same direction as the surrounding atmosphere, the wind direction and wind velocity can be obtained by tracking the movement of clouds. This method has been used to measure the atmospheric motions of other planets, where direct observation is difficult (Rossow et al.1990; Galperin et al. 2014; Oyama et al. 2016), as well as that of the Earth's atmosphere. Especially the atmospheres of Jupiter and Venus have been extensively studied with this technique because of the complete cloudiness of these planets.

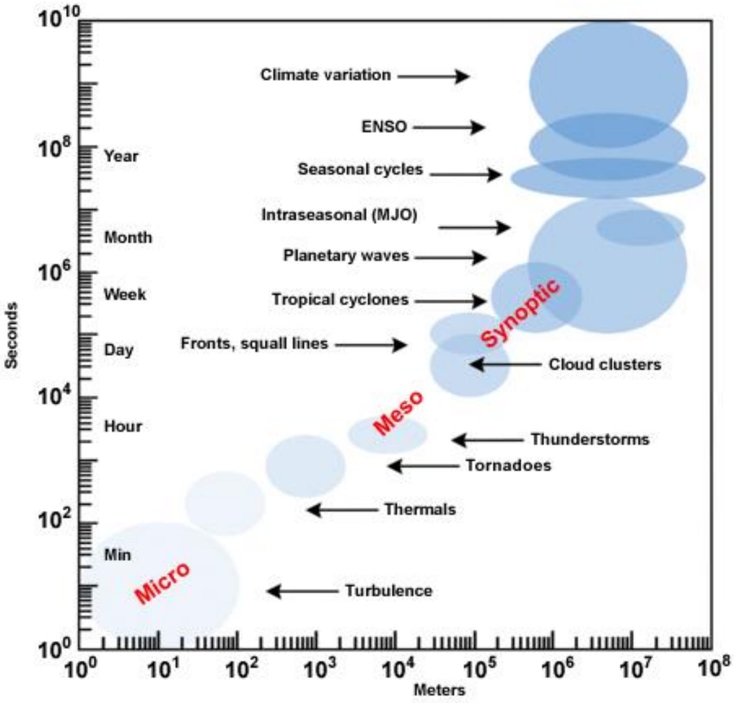

©The COMET Program

Figure 1. Space and time-scales of dynamical atmospheric processes (Laing and Evans 2011).

For Jupiter, temporally-averaged zonal jet structures were first obtained by cloud tracking using images taken by Voyager 1 and 2 (e.g., Ingersoll et al. 1979; Beebe et al. 1980; Ingersoll et al. 1981; Limaye et al. 1986); the locations of the jets are correlated with the banded structures of the cloud color (e.g., Fletcher et al. 2020). At smaller scales, vortex-like winds associated with the Great Red Spot were studied by cloud tracking using images taken by Voyager 1, Voyager 2 and Galileo (e.g., Mitchell et al. 1981; Dowling and Ingersoll 1988; Choi et al. 2007). However, atmospheric motions at scales much smaller than the planet have been unclear, although mesoscale turbulent features are ubiquitously seen in the cloud morphology (Figure 2). Mesoscale in atmospheric dynamics is the scale smaller than synoptic scale, which is the length scale of high- and low-pressure systems, and is typically 1/1000–1/100 of the planetary scale. On Earth, typhoons and squall lines are examples of mesoscale weather systems. Such small vortices might supply energy to the zonal jets via inverse energy cascade (e.g., Williams 1978) or generation of waves that transport zonal momentum (Schneider and Liu, 2009). The same is true for Venus; planetary-scale atmospheric motions such as the westward circulation called “superrotation” (e.g.,Bougher et al. 1997) and planetary-scale waves (e.g., Kouyama et al. 2013; Imai et al. 2019) have been studied using cloud tracking, while the velocity structures of smaller-scale motions have been unknown. Mesoscale vortices on Venus are of interest in that they might be related to streaky or turbulent cloud features that are ubiquitously seen at the cloud top (Figure 3) (Titov et al. 2012); such features are expected to reflect cloud forming processes and play roles in the climate system.

In this study, I aim to improve cloud tracking technique to derive mesoscale atmospheric motions which have not been detected successfully. In the following subsections I briefly review two types of cloud tracking methods that have widely been used: cross correlation method and phase correlation method.

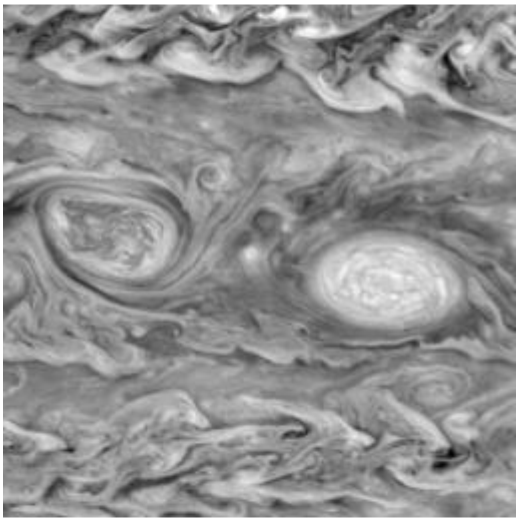

Figure 2. Near infrared images of the southern hemisphere of Jupiter taken by SSI onboard Galileo spacecraft (provided by NASA/JPL-Caltech).

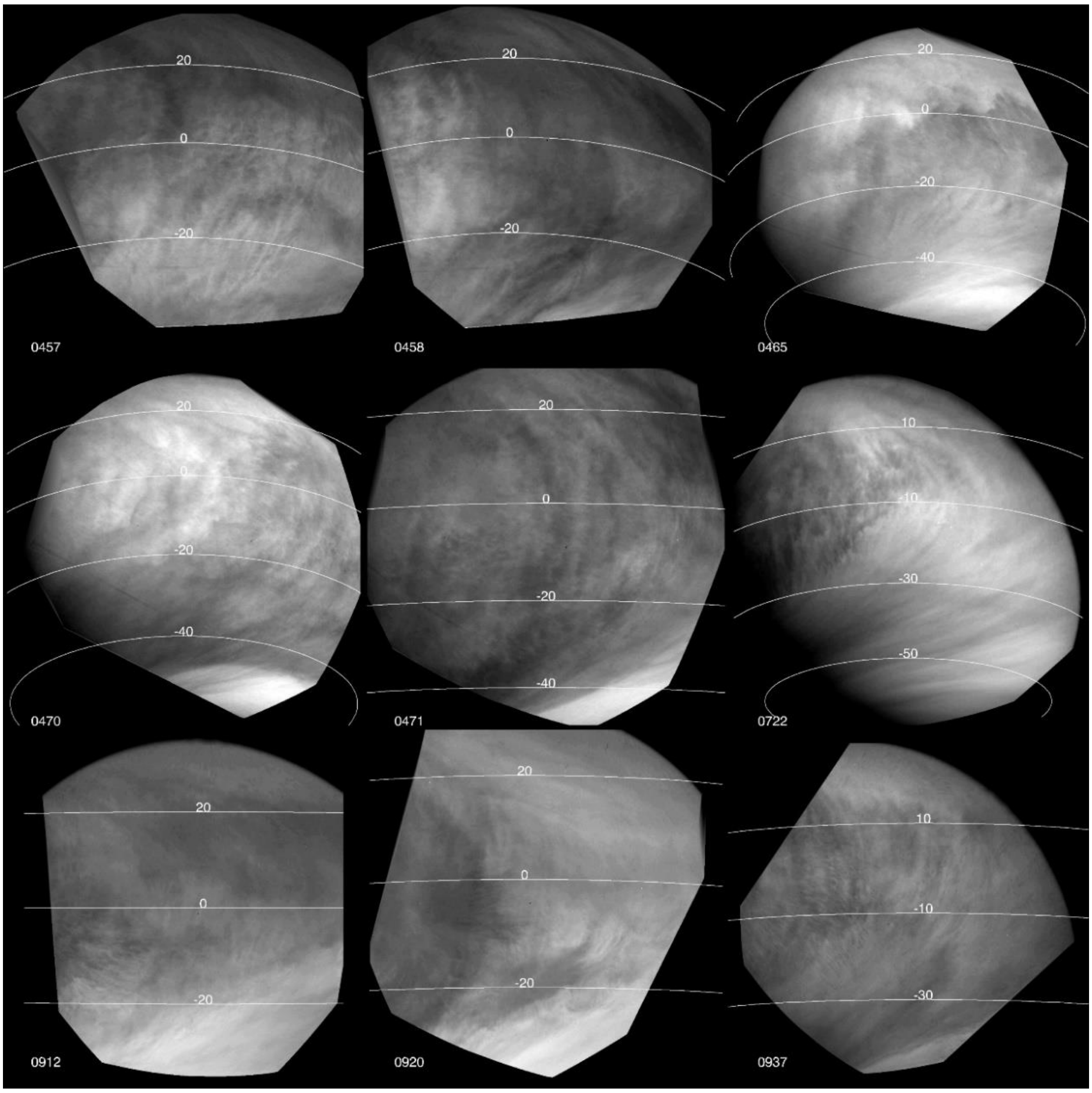

Figure 3. UV (365 nm) images of the equatorial region of Venus taken by VMC onboard Venus Express (Tiotv et al. 2012).

1.2 Cross correlation method

The cloud tracking studies conducted so far have mainly been carried out using the cross correlation method (Kouyama et al. 2012; Khatuntsev et al. 2013; Choi et al. 2007; Ikegawa and Horinouchi 2016; Galperin et al. 2014). The cross correlation method is a technique to locate the position of a specific cloud pattern in successive images using the cross correlation between subimages.

The procedure of is explained below. First, a pair of images separated by a short time interval is prepared, and a small tracking region is placed in the first image. (Figure 4 left)

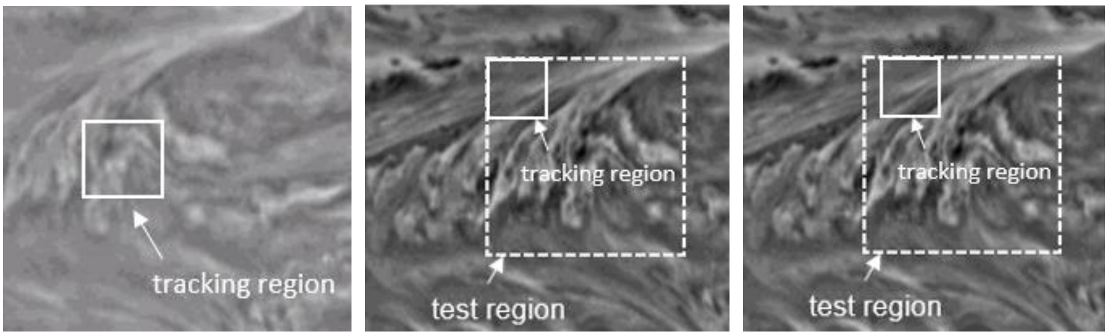

Figure 4. An example of the pair of images separated by a short time interval. (left) First image, in which the tracking region is indicated by an open box. (middle) Second image, in which the test region is indicated by a dashed line and a tracking region indicated by an open box is placed at a corner of the test region. (right) The location of the tracking region was shifted in the second image. The data used are 750-nm images of Jupiter taken by VIMS on board the Cassini spacecraft on 21:01 on December 11, 2000.

Then, a tracking region having the same size as the tracking region is placed in the second image (Figure 4 middle) and the cross correlation between the brightness patterns in the two tracking regions is calculated. This procedure is repeated while the tracking region is shifted sequentially in the test region (Figure 4 right) to create a two-dimensional distribution of the correlation coefficient (correlation surface). Figure 5 shows an example of the correlation surface. The position where the correlation coefficient takes the maximum is regarded as the position to which the cloud pattern in the tracking region in the first image has moved. The wind velocity is obtained by dividing the displacement vector by the time interval between first and the second image.

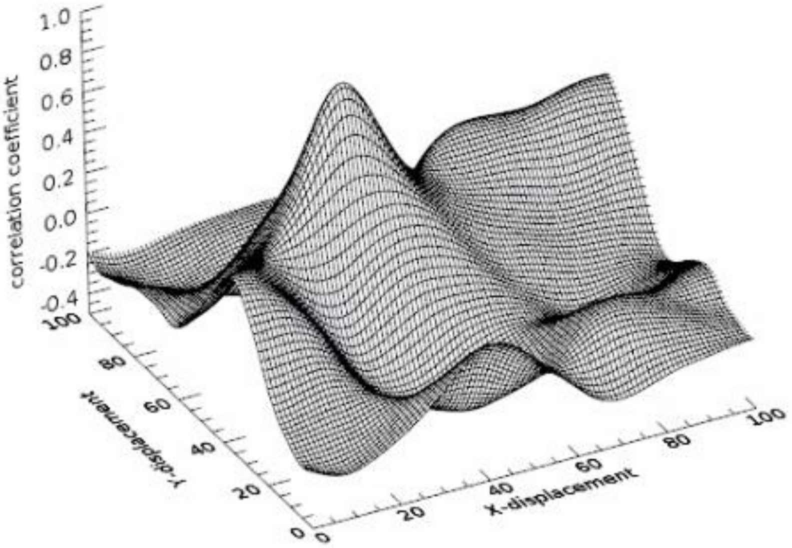

Figure 5. Correlation surface for the case shown in Figure 4. The horizontal axes are the displacements of the tracking region in the test region in the middle and the right panels of Figure 4.

1.3 Phase correlation method

Unlike the cross correlation method, the phase correlation method is a method that applies Fourier transform to the tracking regions and determine the movement of the cloud pattern between the regions using the phase information.

Let us consider a pair of images separated by a certain time interval. Tracking regions $\alpha(x,y)$ and $\beta(x,y)$ are placed in the first and the second images, respectively, as functions of the coordinates (x,y). If $\beta(x,y)$ is obtained by shifting $\alpha(x,y)$ by a in the x direction and by b in the y direction, then $\beta(x,y)=\alpha(x-a,y-b)$. The elements of the Fourier transform of $\beta(x,y)$, denoted by $B(k,l)$, and the Fourier transform of $\alpha(x,y)$, denoted by $A(k,l)$, are written as follows.

$$A(k,l) = \int \alpha(x,y)e^{-i(kx+ly)}\,dx\,dy \tag{1}$$

$$
\begin{aligned}
B(k,l) &= \int \beta(x,y)e^{-i(kx+ly)}\,dx\,dy \\
&= \int \alpha(x,y)e^{-i\left(k\left(x'+a\right)+l\left(y'+b\right)\right)}\,dx'\,dy' \\
&= A(k,l)e^{-i(ka+lb)}
\end{aligned}
\tag{2}
$$

To identify a and b, a normalized cross power spectrum between A and B is calculated to identify the phase correlation matrix F_{AB}:

$$
F_{AB}(k,l) = \frac{\mathrm{B}(k,l)\mathrm{A}(k,l)^*}{|\mathrm{B}(k,l)||\mathrm{A}(k,l)^*|} = \mathrm{e}^{-\mathrm{i}(ka+lb)}. \tag{3}
$$

The phase correlation function Q is calculated by the inverse Fourier transform of F_{AB}:

$$
\begin{aligned}
Q(x,y) &= \int F_{AB}(k,l)\, e^{-i(kx+ly)}\,dk\,dl \\
&= \int e^{-i(ka+lb)}e^{-i(kx+ly)}\,dk\,dl \\
&= \delta(x-a, y-b).
\end{aligned}
\tag{4}
$$

If the cloud patterns in the two tracking regions under comparison are similar, this representation would be a delta function, where the location of the function peak identifies the cloud motion.

This method uses phase information only and is less susceptible to changes in overall luminance and noise. This technique has an advantage that the accuracy of pattern matching is higher than that of the cross correlation method.

1.4 Cloud tracking applied to planetary atmospheres

For the earth, cloud tracking has been used to obtain wind velocity data especially over the ocean, where it is difficult to obtain data by in-situ measurements such as sondes and aircraft. For example, the Meteorological Research Center retrieves cloud motion vectors every hour using continuous images of clouds and water vapor observed by the meteorological satellite Himawari (Oyama et al. 2016) (Figure 6).

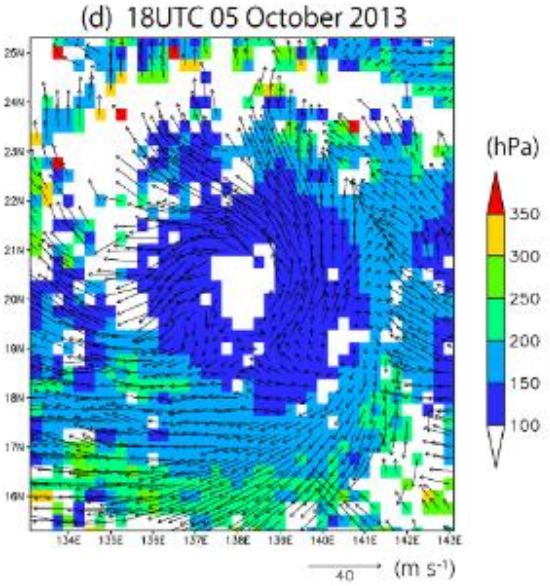

Figure 6. Spatial distributions of wind vectors of the upper tropospheric within a 10° latitude × 10° longitude box at 18:00 on October 5 (Oyama et al. 2016).

Cloud tracking has widely been used also for planetary atmospheres. For example, cloud tracking was applied to Jupiter's atmosphere using images taken by NASA's planetary probe Voyager 1, Voyager 2 and Galileo (e.g., Mitchell et al. 1981; Dowling and Ingersoll 1988; Choi et al. 2007) and Cassini (Galperin et al. 2014) during their Jupiter flyby (Figure 7).

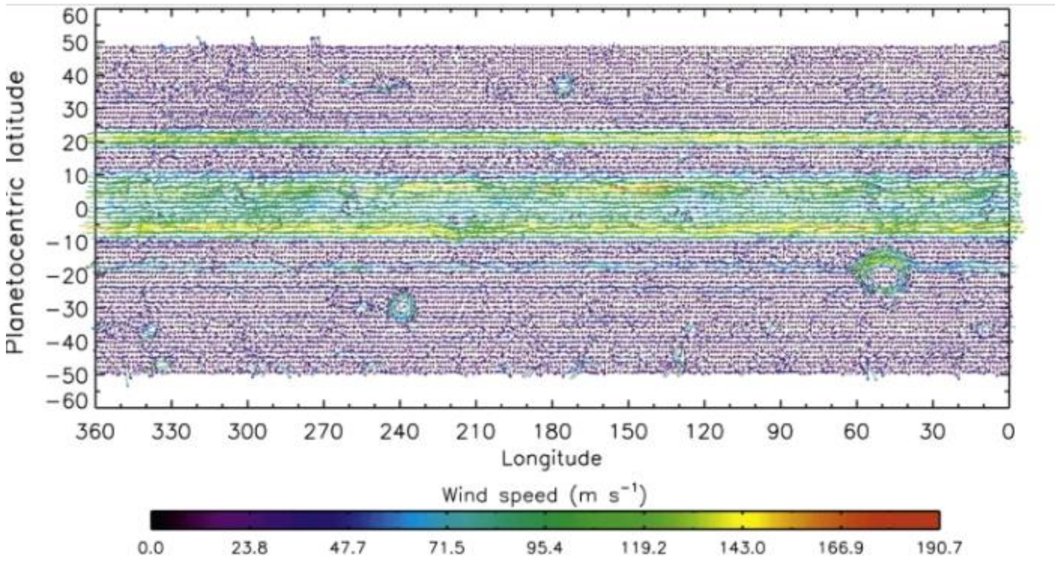

Figure 7. Velocity obtained by cloud tracking using 750 nm images taken by Cassini between December 11, 2000 and December 12, 2000 (Galperin et al. 2014).

For Venus, cloud tracking was used in NASA’s Mariner 10 (Limaye and Suomi 1981) and Pioneer Venus (Rossow et al. 1990), and wind fields at multiple altitudes have been obtained using images taken by ESA’s spacecraft Venus Express (Hueso et al. 2012; Ikegawa and Horinouchi 2016) (Figures 8 and 9) and JAXA's spacecraft Akatsuki (Horinouchi et al. 2018; 2017). The detailed velocity structures such as the existence of jets have been revealed (Horinouchi et al. 2017).

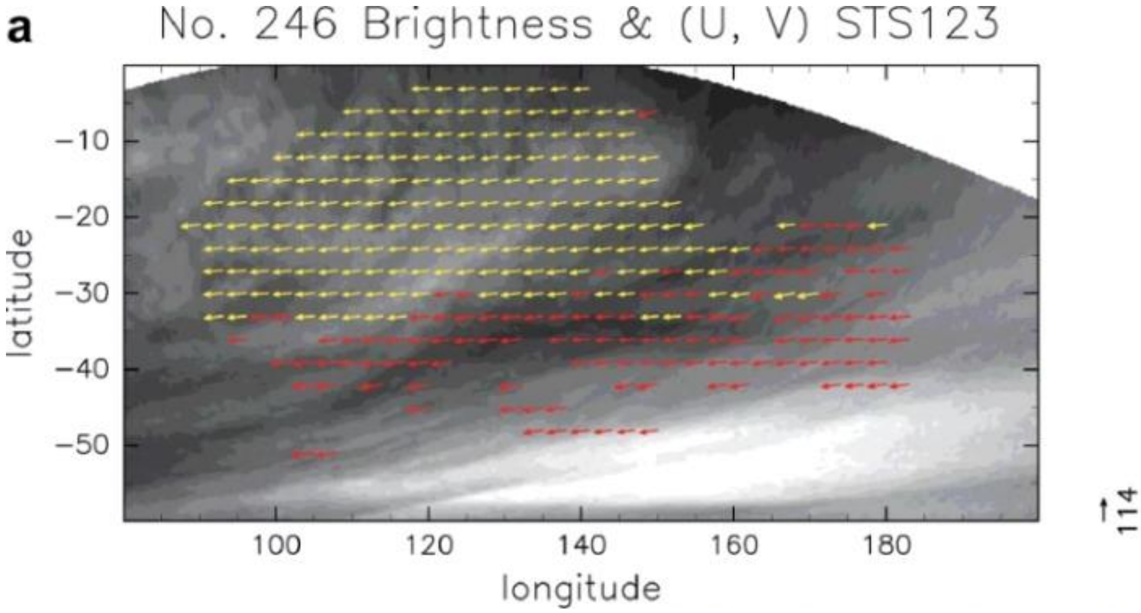

Figure 8. The cloud motion vectors (arrows) obtained by cross correlation method for the VMC UV orbit 246 images (Ikegawa and Horinouchi 2016).

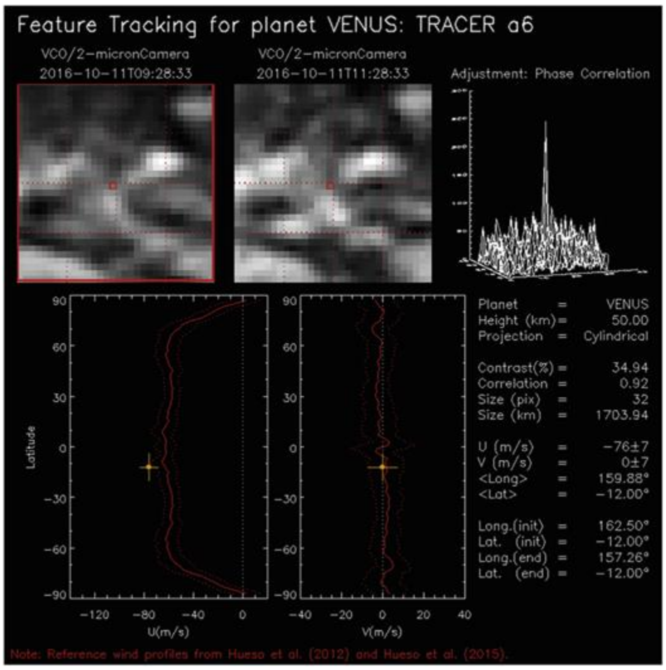

```
Planet         =        VENUS
Height (km)=            50.00
Projection     =  Cylindrical

Contrast(%) =           34.94
Correlation    =         0.92
Size (pix)     =           32
Size (km)      =      1703.94

U (m/s)        =       -76±7
V (m/s)        =         0±7
<Long>         =      159.88°
<Lat>          =      -12.00°

Long.(init)    =      162.50°
Lat.   (init)  =      -12.00°
Long.(end)     =      157.26°
Lat.   (end)   =      -12.00°
```

Figure 9. Example of positive identification of a cloud tracer on Venus using phase correlation in a pair of near-infrared images taken by Akatsuki spacecraft (Peralta et al. 2018).

2. Rotation invariant phase-only correlation method

2.1 The principle of the analysis

Both in the cross correlation method and the phase correlation method, only the parallel movement of the tracking region can be detected, and thus the peak of the correlation surface would become low or the matching would fail when there exists a rotation or an enlargement/reduction of the cloud pattern. The rotation invariant phase-only correlation method is a technique developed from the phase correlation method mentioned previously. In this method, the tracking region is Fourier-transformed before applying the phase correlation method for measuring parallel movement, and logarithmic polar coordinate conversion is performed to the amplitude spectra so that the rotation and enlargement/reduction motions can be obtained as parallel movements (Figure 10). The transformation from the Cartesian coordinate $(x,\ y)$ to the logarithmic polar coordinate (θ, ρ) is expressed by

$$\begin{aligned} \rho &= \log\sqrt{x^2 + y^2}, \\ \theta &= \arctan(y/x). \end{aligned} \tag{5}$$

Rotation of the image in the cartesian coordinate system is represented by the parallel movement in the θ direction in the logarithmic polar coordinate system (Figure 10). However, if we apply logarithmic polar coordinate conversion to the original image, the magnitude of θ depends on the choice of the origin of the coordinate. To avoid this ambiguity, the original image is Fourier transformed, and the zero frequency bin of the resultant two-dimensional amplitude spectrum is adopted as the origin of the log-polar transform (Figure 11). When the original image is rotated around an arbitrary rotation center, the amplitude spectrum is rotated by the same magnitude with respect to the origin (zero frequency). This has the advantage that the center of rotation does not have to be the center of the tracking region when applying the rotation invariant phase-only correlation method. As a result, it is possible to track the rotation and the enlargement/reduction of the image, which were not obtained by the cross-correlation method and the phase correlation method. Once the rotation angle is obtained, the original image is rotated by this angle and then the phase correlation method for parallel movement can be used. The method has been used in the field of biometrics such as dental radiograph images (Nikaido et al. 2006).

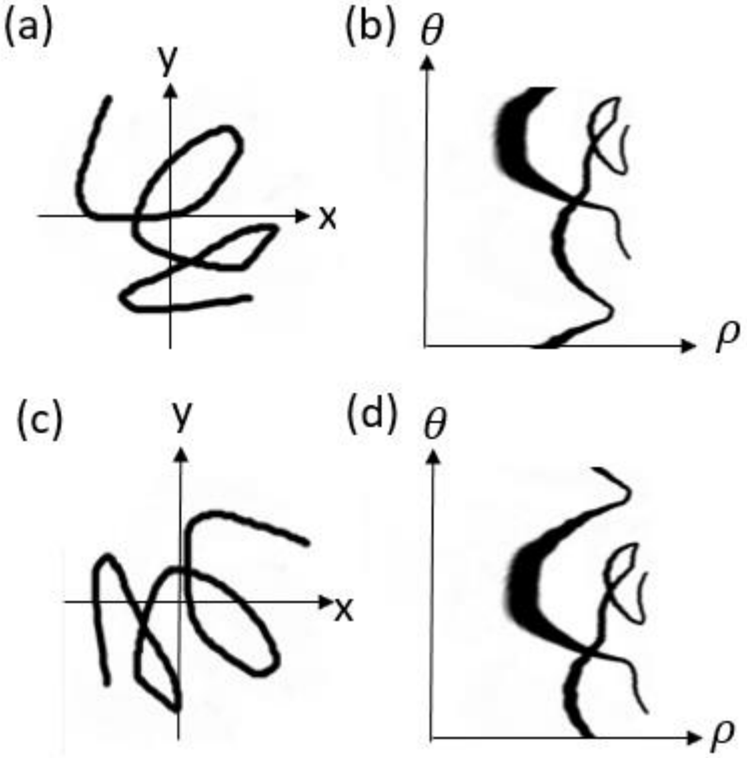

Figure 10. (a) Example image in the cartesian coordinate system and (b) logarithmic polar coordinate conversion of (a). (c) Image rotated (a) by 90°, and (d) logarithmic polar coordinate conversion of (c).

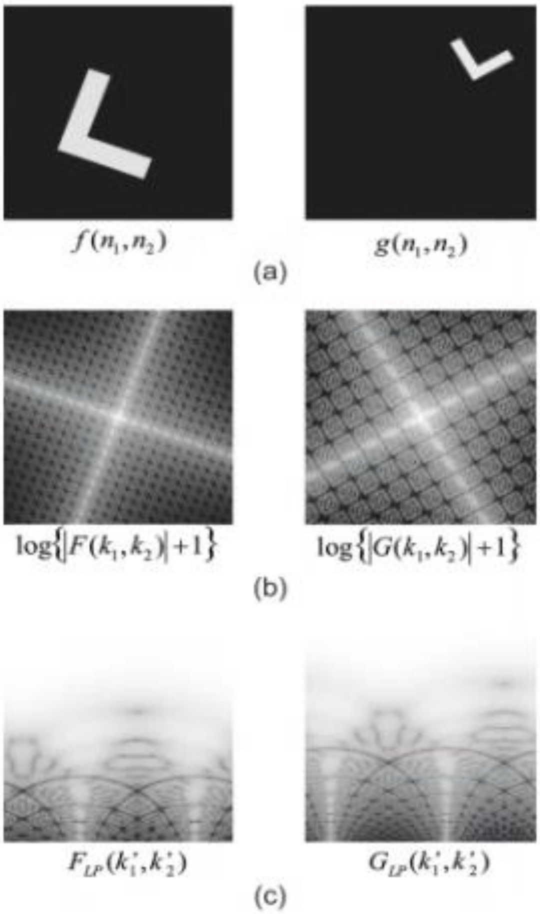

Figure 11. (a) Input image (b) Logarithmic amplitude spectrum (c) Spectrum after logarithmic polar coordinate conversion (Aoki et al. 2007).

2.2 Application to cloud tracking

In this study, the rotation invariant phase-only correlation method is applied to cloud tracking. The details are described below.

First, high-pass filter is applied to emphasize fine patterns in the image. The image is smoothed by a Gaussian filter with HWHM of 16 × 16 pixels that correspond to 2° in longitude and latitude for Venus and 0.8° for Jupiter, and the smoothed image is subtracted from the original to produce an image in which detailed patterns were emphasized. (Figure 12)

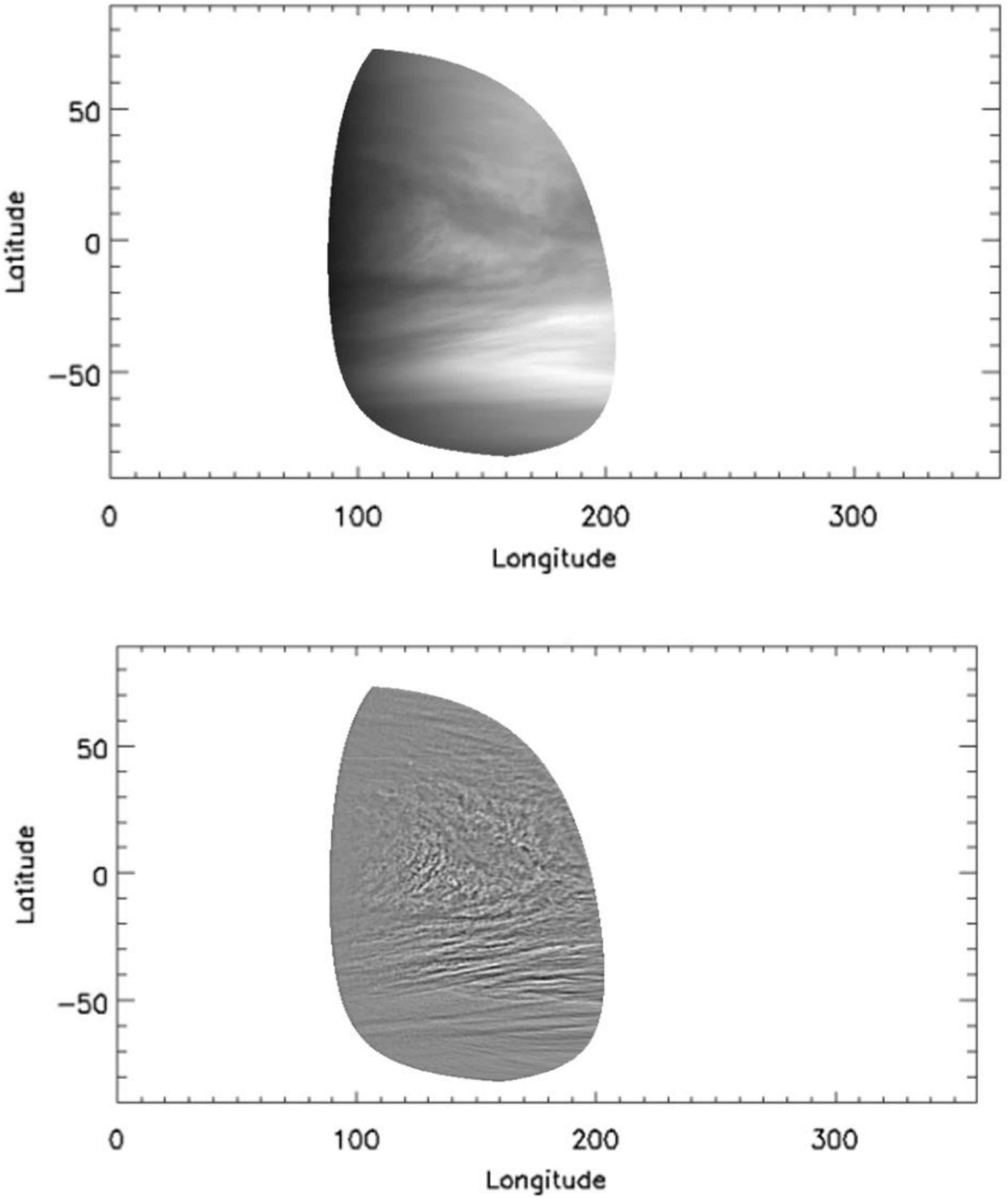

Figure 12. (top) Image of Venus at 365-nm wavelength projected onto the longitude-latitude coordinate and (bottom) the high-pass filtered image

After high-pass filtering, for a given tracking region in the first image, the tracking region in the second image is determined by the cross correlation method so that common cloud patterns are included (Figure 13-a,b). Then, Fourier transform with hanning window is performed on each tracking region to obtain two-dimensional amplitude spectra (Figure 13-c,d). Placing the zero frequency of the amplitude spectrum at the center of the image, logarithmic polar coordinate conversion (Eq. 5) is performed to the amplitude spectra (Figure 13-e,f).

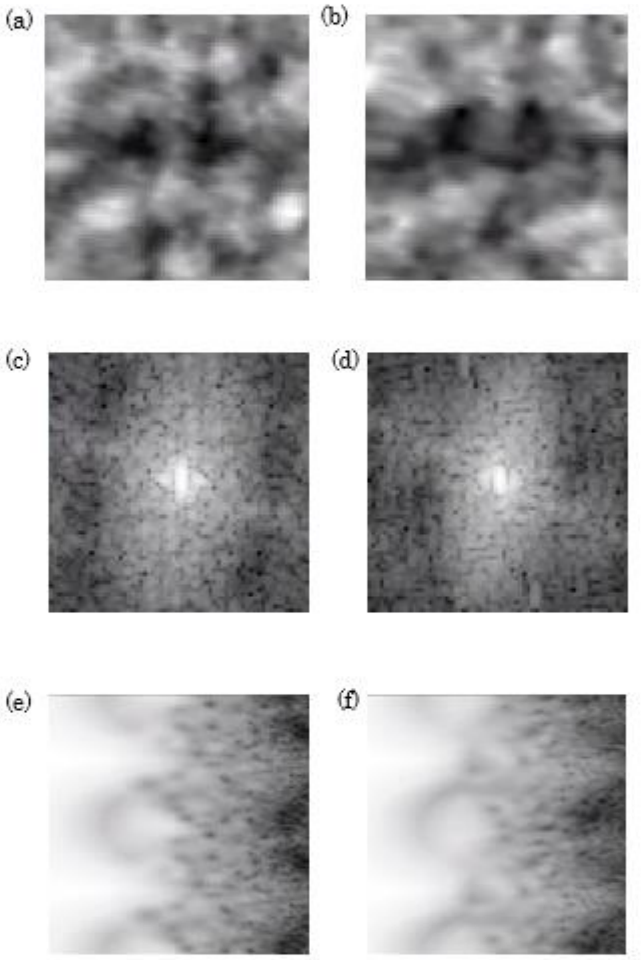

Figure 13. (a) Tracking region in the first image,, (b) Tracking region in the second image, (c) amplitude spectrum of (a), (d) amplitude spectrum of (b), (e) logarithmic polar transformation of (c) and (f) logarithmic polar transformation of (d). These images used the Venus 365-nm image.

The rotation angle is obtained by finding the displacement that gives the maximum cross correlation between the spectra converted by the logarithmic polar coordinate transformation. In this study, only the rotation angle was obtained assuming that there is no detectable enlargement/reduction, because large scale motion in a stable stratified atmosphere is expected to be dominated by horizontal two-dimensional motion (Nastrom and Gage 1985). Next, the tracking region in the original second image is rotated based on the obtained rotation angle, and then the tracking regions in the image pair are

Fourier-transformed to extract the phase spectra, which are used to determine the amount of parallel translation using the phase correlation method (Eq. 4).

The accuracy of cloud tracking in any of the cross-correlation method, the phase correlation method, and the rotation invariant phase-only correlation method is usually limited by one pixel unit, and it is not possible to estimate the movement in sub-pixel units. In the phase correlation method, it is known that an ideal correlation peak is represented by a sinc function, and thus sub-pixel estimation by fitting a sinc function to the correlation surface is considered possible. However, in the case of the images used in this study, the correlation peak is not well represented by a sinc function due to the influence of noise and possibly the deformation of cloud patterns. Therefore, in this study, subpixel estimation was achieved by increasing the number of data points using up-sampling. In this method, the number of apparent data points is increased by inserting zeros alternately into the phase correlation matrix (Eq.4), and then inverse Fourier transform is performed to increase the amount of data points near the peak of the correlation surface, thereby obtaining the peak position in sub-pixel units. In this study, the velocity was derived in 0.5 pixel units. The velocity is obtained by dividing the determined translation by the time interval between the images.

The accuracy of cloud tracking is often significantly lowered by the deformation of cloud patterns. To detect such erroneous results, the tracking region in the second image is resampled based on the retrieved rotation angle and the retrieved translation, and then the cross correlation between the tracking regions in the first and the second image is calculated. The result is rejected if the peak value of the correlation is smaller than 0.5.

3. Test with simulated data

3.1 Setup

The proposed method was tested using simulated image pairs. An ultraviolet image of Venus cloud, that was taken at the wavelength of 365-nm by the Venus orbiter Akatsuki on October 3, 2016 and mapped onto the longitude-latitude coordinate with grid intervals of 0.125° both in the latitude and the longitude (Ogohara et al., 2017), was adopted as the first image (Figure 14), and the second image was created from the first one by transporting the cloud pattern following the specified wind field. The curvature of the planetary surface is ignored. The time interval between the two images is assumed to be 2 hours. As the wind filed, the following three types are assumed:

(1) a solid body rotation centered at a certain point on the equator

(2) an irrotational vortex in which the flow speed is inversely proportional to the distance from the rotation center and the vorticity is zero everywhere

(3) sinusoidal velocity field with wavelengths of 5°×5° and 10°×10° in longitude and latitude

The size of the tracking region is 64×64 pixels (corresponding to 8° ×8° in the latitude and the longitude) in the first and the second experiment. In the third experiment the sizes of 80×80 pixels (10° ×10°) and 40x40 pixels (5° ×5°) are tested.

The derived rotation rate is compared with the vorticity calculated from the cloud-tracked velocity to evaluate the merit of the rotation detection proposed in this thesis. The vorticity ζ is defined as

$$\zeta = \frac{\partial V}{\partial x} - \frac{\partial U}{\partial y}\,, \tag{6}$$

where U is the eastward velocity, V is the northward velocity, x is the eastward distance and y is the northward distance. According to the concept of continuum mechanics, the velocity gradient is represented by the sum of the deformation rate and the rotational rate, and the rotation rate ω is written as

$$\omega = \frac{1}{2}\left(\frac{\partial V}{\partial x} - \frac{\partial U}{\partial y}\right) = \frac{\zeta}{2}. \tag{7}$$

Therefore, the rotation rate is 1/2 of the vorticity.

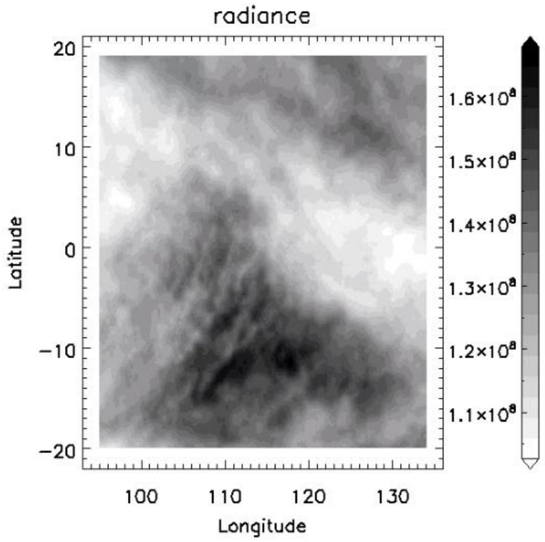

Figure 14. An ultraviolet image of Venus cloud used as the first image in the tests. The data was taken at the wavelength of 365-nm by the Venus orbiter Akatsuki on October 3, 2016

3.2 Solid body rotation

Simulated data for solid body rotation, i.e. rotation at a constant angular velocity everywhere, was prepared. The second image is rotated relative to the first image clockwise by 5° in a circular area with a radius of 20° in latitude and longitude centered at the rotation center located at the longitude of 115° on the equator. This rotation is assumed to occur in 2 hours. Then, the true value of the rotation rate is 1.2×10^{-5} rad s^{-1} and that of the vorticity is uniformly $2.3 \times 10^{-5}\ s^{-1}$. Figure 15 shows the velocity obtained by cloud tracking. The accuracy of the velocity is limited by the 0.5 pixel size and is estimated to be 1.8 m s^{-1}; the measured velocities are correct within the error. Figure 16 shows the rotation rate of the cloud pattern obtained by the newly-developed method and the vorticity calculated from the cloud-tracked velocity. The rotation rate is -1.2×10^{-5} rad s^{-1} in all regions with the discretization step (error) of 0.12×10^{-5} rad s^{-1} and the vorticity is $-2.3 \pm 0.9 \times 10^{-5} s^{-1}$. The accuracy of the rotation rate is limited by the pixel size in the amplitude spectrum space (section 2.2) and is estimated to be 0.5 degrees, corresponding to the rotation rate error of 0.12×10^{-5} rad s^{-1}. The vorticity error is estimated to be $1.1 \times 10^{-5}\ s^{-1}$ from the velocity measurement error. The vorticity and rotation rate are correctly obtained within the range of the error. Given the magnitude of the estimated error, the rotational rate obtained by the newly-developed method is much more accurate than the vorticity obtained from the velocity; this merit was confirmed by the simulation.

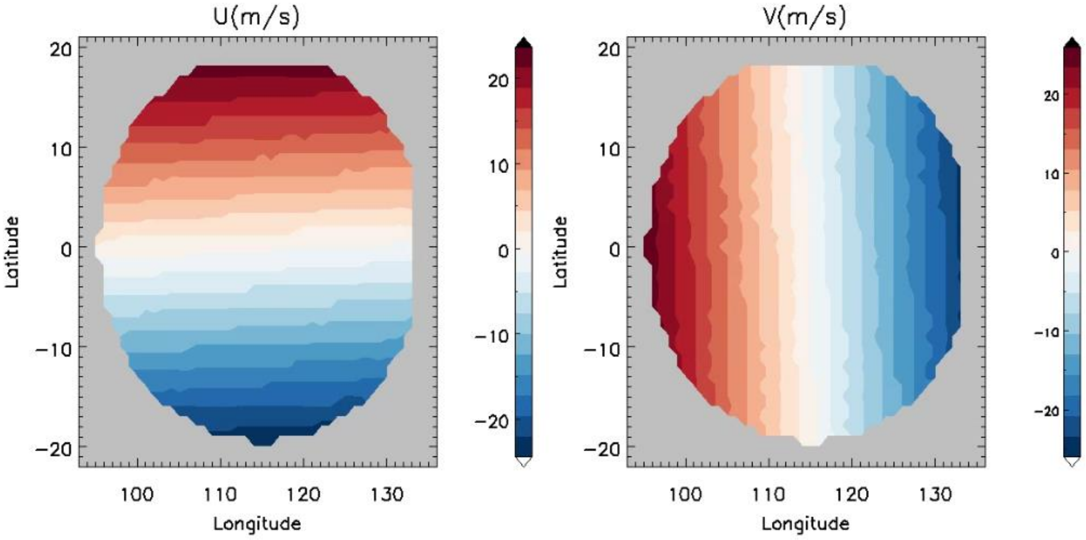

Figure 15. (left) Eastward and (right) northwad velocity obtained by cloud tracking in the test of the solid body rotation.

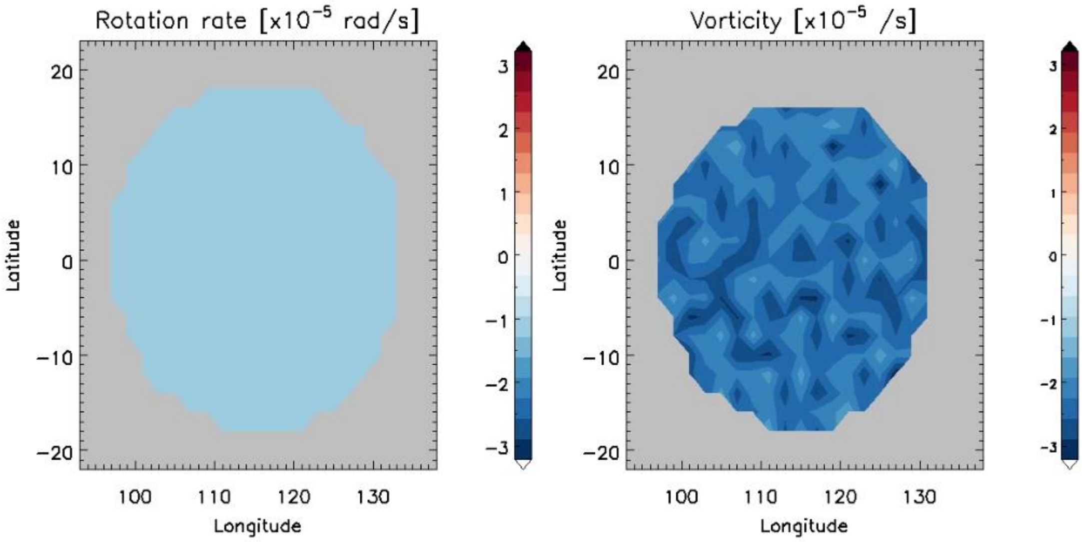

Figure 16. (left) Rotation rate of the cloud pattern obtained by the newly-developed method and (right) the vorticity calculated from the cloud-tracked velocity shown in Fig. 4 in the test of the solid body rotation.

3.3 Irrotational vortex

Simulated data for irrotational vortex was prepared. The second image is deformed relative to the first image by the velocity expressed as $100 \times r^{-1}\, m\, s^{-1}$, where r is the distance from the center of rotation in a circular area with a radius of 20°. The rotation center is located at the longitude of 115° on the equator. In the case of irrotational vortex, both the rotation rate and the vorticity should be zero.

Figure 17 shows the rotation rate of the cloud pattern obtained by the newly-developed method and the vorticity calculated from the cloud-tracked velocity. Cloud tracking is not possible near the center of the rotation because the deformation of the cloud pattern is too large. The rotation rate is 0.0×10^{-5} rad s^{-1} in all regions with the discretization step (error) of 0.12×10^{-5} rad s^{-1} and the vorticity $0.0 \times 10^{-5} \pm 1.6 \times 10^{-5}\,\mathrm{s}^{-1}$. The expected error in the rotation rate is 1.2×10^{-6} rad s^{-1} and that in the vorticity is $1.1 \times 10^{-5}\,\mathrm{s}^{-1}$ (section 3.2). The rotation rate is correctly obtained within the range of the error. On the other hand, the error of the obtained vorticity exceeds the expected error range. The error of the vorticity can arise from the finite grid size as well as the cloud tracking error considered above. To evaluate the effect of the grid size, the vorticity was calculated from the given (ideal) velocity field using the discrete grid and shown in Figure 18. The vorticity error here is $\pm 0.5 \times 10^{-5}\,\mathrm{s}^{-1}$, suggesting that combination of the cloud tracking error and the error from the grid size can explain the error in the obtained vorticity. From the above results, the rotation rate obtained by the new method can be much more accurate than the vorticity calculated from the velocity.

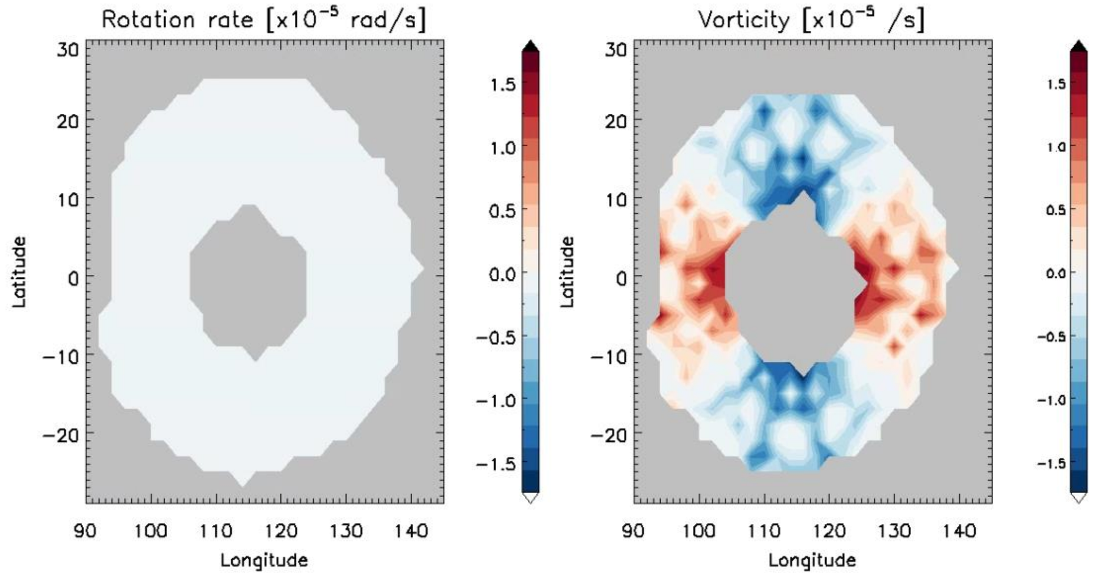

Figure 17. Same as Figure 16, but for the test of the irrotational vortex.

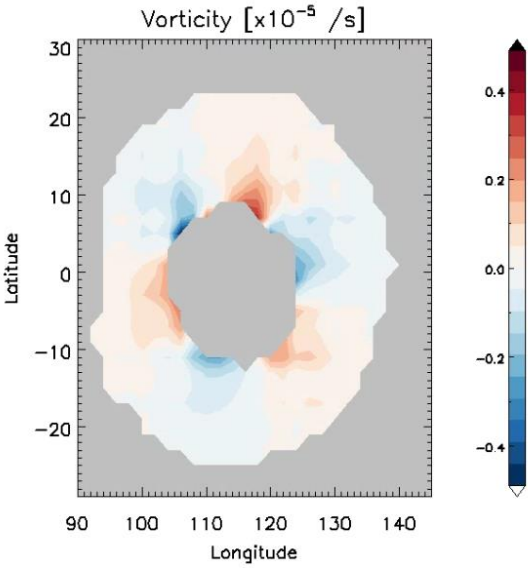

Figure 18. Vorticity calculated from the ideal velocity field

3.4 Sinusoidal structure in latitudinal or longitudinal direction

The zonal (east-west) wind that oscillates sinusoidally in the meridional (north-south) direction was tested (Table 1). This wind field is divergence free.

Table 1. Setup of the test for the zonal velocity oscillating sinusoidally in the meridional direction.

Size of tracking region (Latitude×longitude)	Zonal velocity (m s^{-1})	Meridional velocity (m s^{-1})
8°×8°	5×sin(2π ×latitude/10°)	0

The true amplitude of the rotation rate is 1.5×10^{-5} rad s^{-1} and that of the vorticity is $3.0 \times 10^{-5}\ s^{-1}$. Figure 19 shows the velocity obtained by cloud tracking, and Figure 20 shows the rotation rate of the cloud pattern obtained by the newly-developed method and the vorticity calculated from the cloud-tracked velocity. The north-south velocity is uniformly zero, which is consistent with the assumed velocity. The amplitude of the east-west velocity is ~4.8 m s^{-1}, which is consistent with the true velocity within the error of 1.8 m s^{-1} (section 3.2). The vorticity amplitude is ~$3.0 \times 10^{-5}\ s^{-1}$, which is consistent with the true vorticity. The rotation rate shows a pattern similar to that of the vorticity, but its amplitude of ~0.5×10^{-5} rad s^{-1} is about 33% of the true amplitude. This is attributed to (1) the deformation of cloud patterns which has a magnitude similar to the local rotation and (2) the size of the tracking region exceeding the spatial scale of the wind shear, which is given by 10°/2π ~ 1.6°. The random error of the obtained rotation rate is estimated to be ~1.0×10^{-6} rad s^{-1} from the standard deviation in the longitudinal profiles; this value is consistent with the expected error (section 3.2).

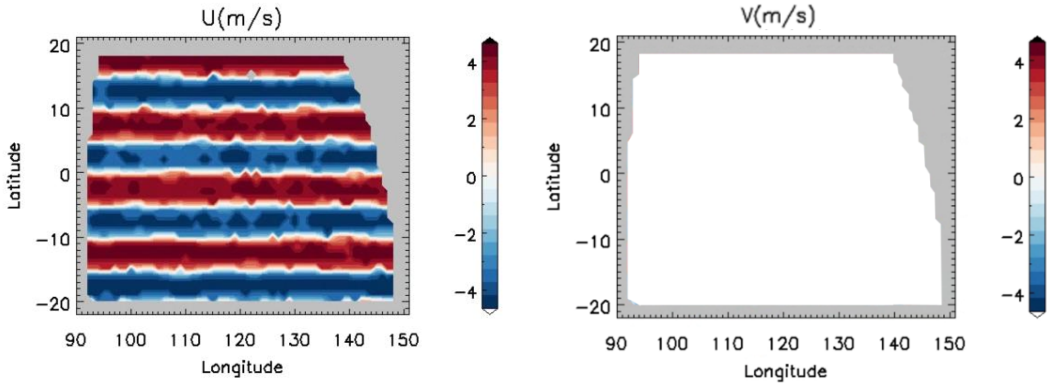

Figure 19. Same as Figure 15, but for the zonal velocity oscillating sinusoidally in the meridional direction.

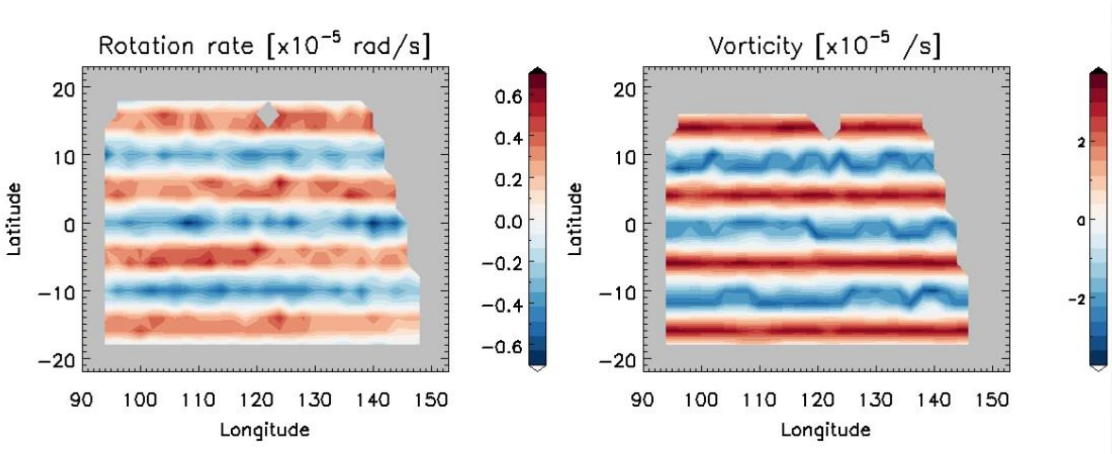

Figure 20. Same as Figure 16, but for the zonal velocity oscillating sinusoidally in the meridional direction.

Similarly, the zonal (east-west) wind that oscillates sinusoidally in the latitudinal direction was tested (Table 2).

Table 2. Setup of the test for the meridional velocity oscillating sinusoidally in the zonal direction.

Size of tracking region (Latitude×longitude)	Zonal velocity (m s^{-1})	Meridional velocity (m s^{-1})
8°×8°	0	5×sin(2π ×longitude/10°)

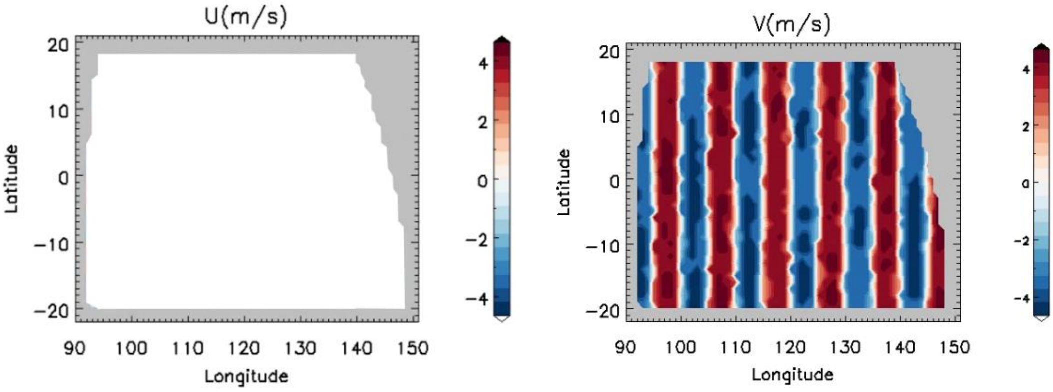

Figure 21. Same as Figure 15, but for the meridional velocity oscillating sinusoidally in the zonal direction.

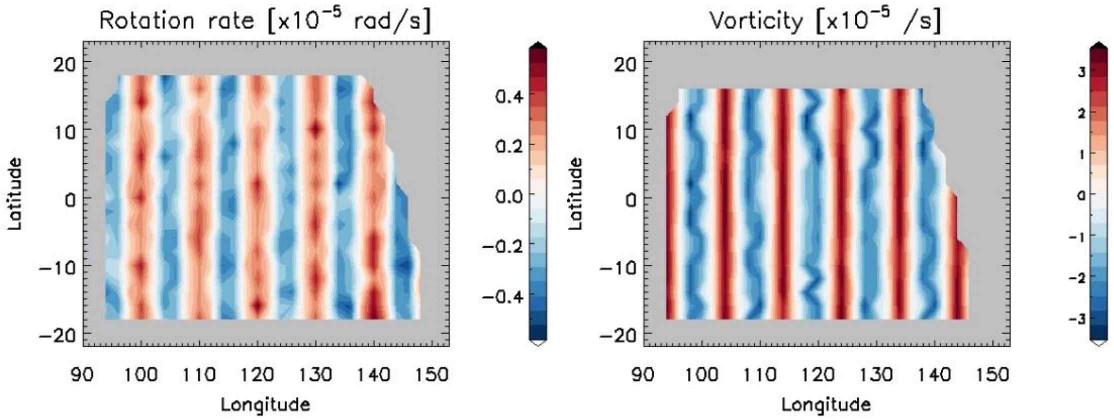

Figure 22. Same as Figure 16, but for the meridional velocity oscillating sinusoidally in the zonal direction.

Figure 21 shows the velocity obtained by cloud tracking and Figure 22 shows the rotation rate of the cloud pattern obtained by the newly-developed method and the vorticity calculated from the cloud-tracked velocity. Both results are similar to the previous case.

3.5 Sinusoidal velocity structure in latitudinal and longitudinal direction

A zonal wind that oscillates sinusoidally in the meridional direction and a meridional wind that oscillates sinusoidally in the zonal direction are superposed. The wavelengths of 10° and 5° are adopted to investigate the spatial scale of the wind disturbance that can be captured by the proposed method. The size of the tracking region, that determines the spatial resolution of the analysis, is 8°×8° and 4°×4°. The following three cases were examined (Table 3).

Table 3. Setup of the test for the combination of the meridional velocity oscillating sinusoidally in the zonal direction and the meridional velocity oscillating sinusoidally in the zonal direction.

Case	Size of tracking region (Latitude×longitude)	Zonal velocity (m s^{-1})	Meridional velocity (m s^{-1})
1	8°×8°	5×sin(2π ×latitude/10°)	5×sin(2π ×longitude/10°)
2	8°×8°	5×sin(2π ×latitude/5°)	5×sin(2π ×latitude/5°)
3	4°×4°	5×sin(2π ×latitude/5°)	5×sin(2π ×latitude/5°)

Case 1:

The true amplitude of the rotation rate and the vorticity are 3.0×10^{-5} rad s^{-1} and 6.0×10^{-5} s^{-1}, respectively. Figure 23 shows the obtained velocity and Figure 24 shows the rotation rate of the cloud pattern obtained by the newly-developed method and the vorticity calculated from the cloud-tracked velocity. The amplitude of the velocity is 4.5 m s^{-1}, which is the same as the true velocity within the error of 1.8 m s^{-1} (section 3.2). The vorticity amplitude is $\sim 3.0 \times 10^{-5}$ s^{-1} that is 50% of the true value. The rotation rate shows a pattern similar to the vorticity, but its amplitude of $\sim 1.8 \times 10^{-5}$ rad s^{-1} is 60% of the true amplitude. This is attributed to the size of the tracking region that is larger than the spatial scale of the wind disturbance.

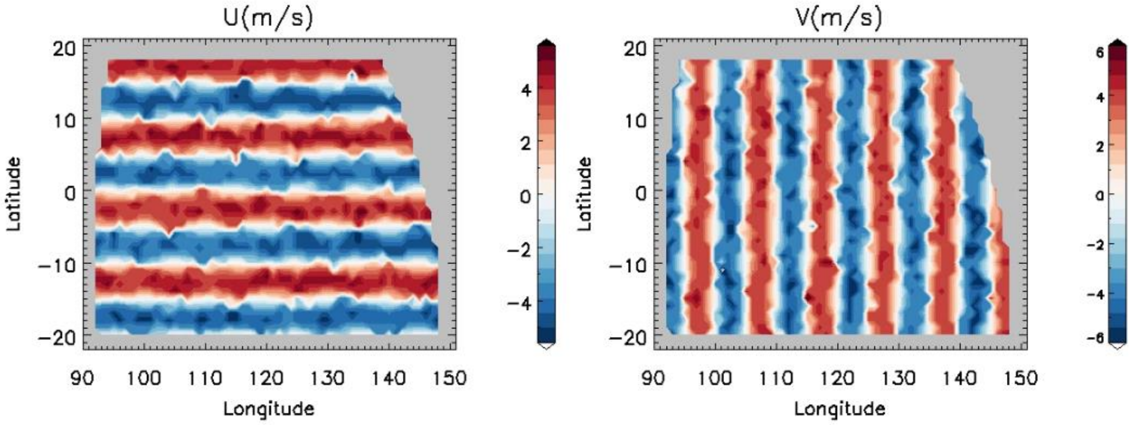

Figure 23. Same as Figure 15, but for the case where the meridional velocity oscillating sinusoidally in the zonal direction and the zonal velocity oscillating sinusoidally in the meridional direction are superposed.

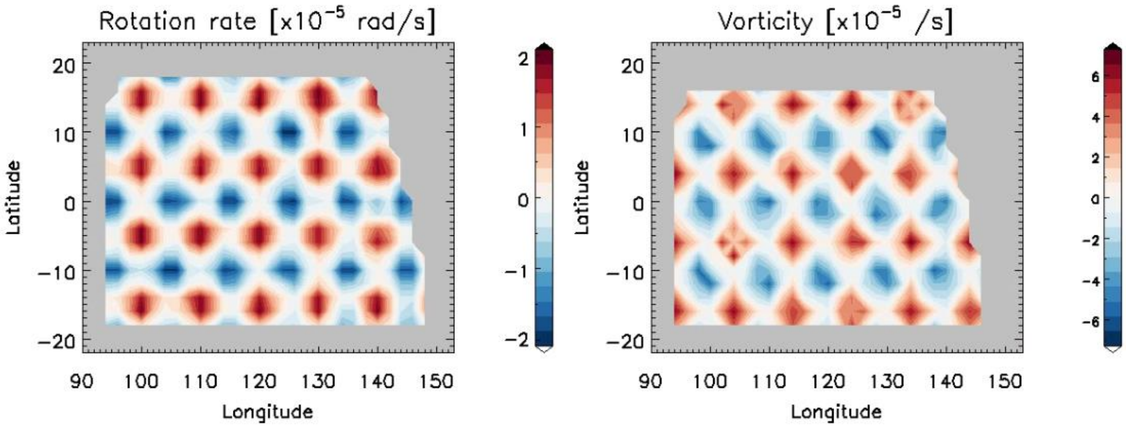

Figure 24. Same as Figure 16, but for the case where the meridional velocity oscillating sinusoidally in the zonal direction and the zonal velocity oscillating sinusoidally in the meridional direction are superposed.

Case 2:

The true amplitude of the rotation rate and the vorticity are $6.0 \times 10^{-5}\ \mathrm{rad\ s^{-1}}$ and $12.0 \times 10^{-5}\ \mathrm{s^{-1}}$, respectively. Figure 25 shows the obtained velocity and Figure 26 shows the rotation rate of the cloud pattern obtained by the newly-developed method and the vorticity calculated from the cloud-tracked velocity. The amplitude of the velocity is ~4 m $\mathrm{s^{-1}}$, which is consistent with the true velocity within the error of 1.8 m $\mathrm{s^{-1}}$ (section 3.2). The vorticity amplitude is $\sim 3.3 \times 10^{-5}\ s^{-1}$ that is 27.5% of the true value The rotation rate shows a spatial pattern similar to the vorticity, but its amplitude of $\sim 0.5 \times 10^{-5}\ \mathrm{rad\ s^{-1}}$ is about 8% of the true amplitude. This is attributed to the size of the tracking region being much larger than the spatial scale of the wind disturbance.

When the spatial scale of the velocity structure is much smaller than the size of the tracking region like this experiment, the area where velocities are not properly obtained increases, and thus the coverage of the vorticity derived from the velocity is reduced. Even in such a case the rotation rate is obtained in most of the domain, although the amplitude is significantly underestimated.

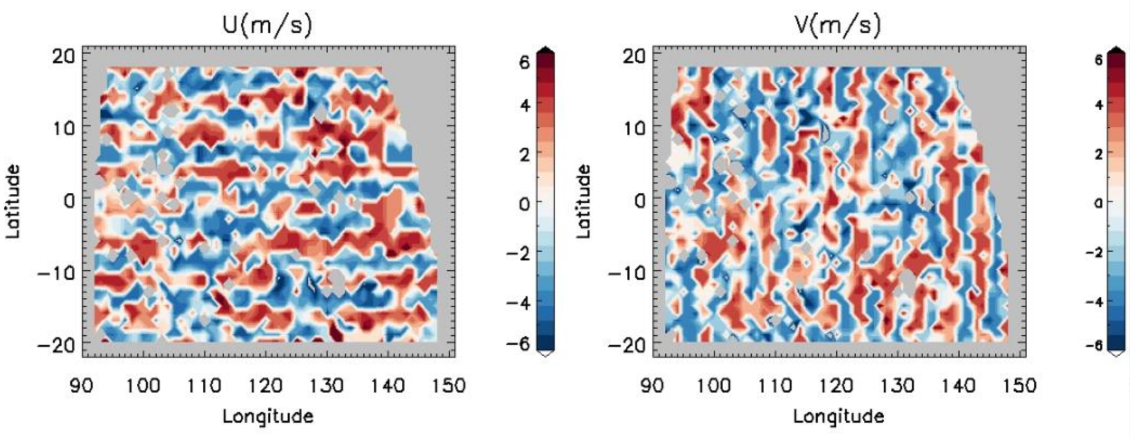

Figure 25. Same as Figure 23, but for a shorter wavelength.

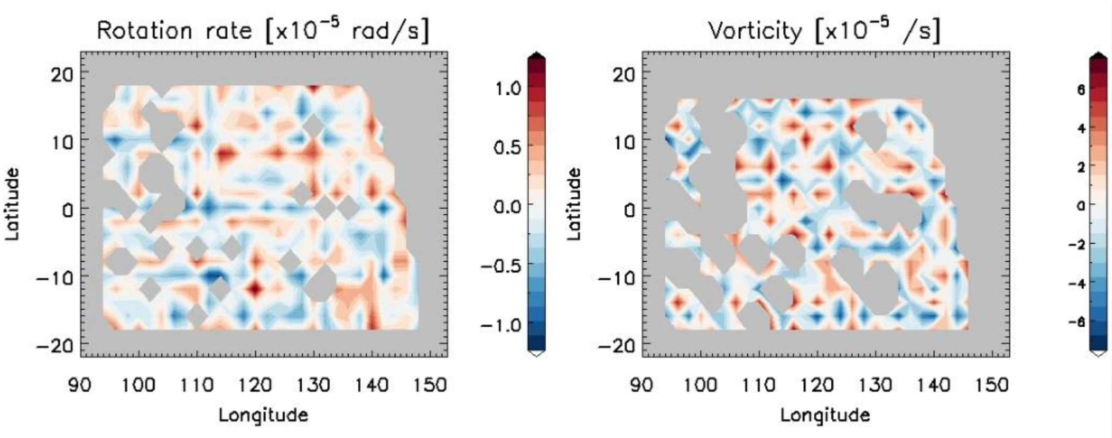

Figure 26. Same as Figure 24, but for a shorter wavelength.

Case 3

The true amplitude of the rotation rate and the vorticity are 6.0×10^{-5} rad s^{-1} and 12.0×10^{-5} s^{-1}, respectively. Figure 27 shows the obtained velocity and Figure 28 shows the rotation rate of the cloud pattern obtained by the newly-developed method and the vorticity calculated from the cloud-tracked velocity. The amplitude of the velocity is 5.6 m s^{-1}, which is consistent with the true velocity within the error of 1.8 m s^{-1} (section 3.2). The vorticity is hardly obtained, although a qualitatively reasonable structure is seen with the amplitude of ~4.2×10^{-5} s^{-1} that is 35% of the true value. The amplitude of the rotation rate is ~1.9×10^{-5} rad s^{-1}, which is about 15% of the true amplitude. This is because the size of the tracking region is larger than the spatial scale of the wind disturbance. Similarly to Case 2, the spatial pattern of the rotation rate is obtained to some extent even when the vorticity is hardly obtained.

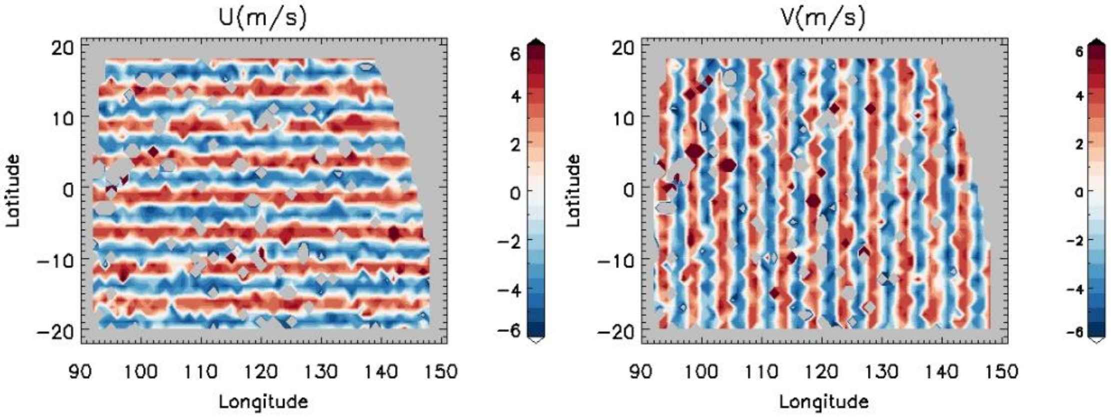

Figure 27. Same as Figure 23, but for a smaller tracking region size.

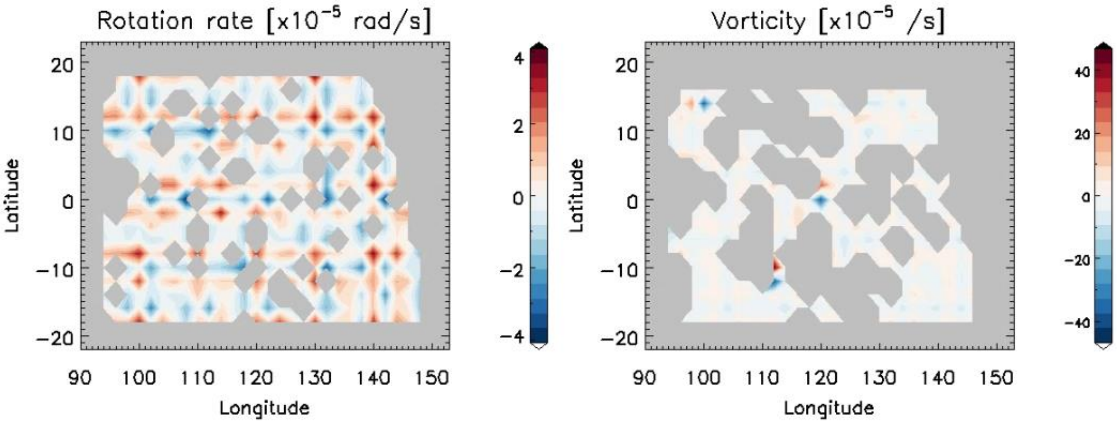

Figure 28. Same as Figure 24, but for a smaller tracking region size.

3.6 Summary of the tests

From the results above, I conclude:

1) From solid body rotation experiment (section 3.2): Large-scale rotations can be measured more accurately by the new method than by the calculation of vorticity from the cloud-tracked velocity.
2) From irrotational vortex experiment (section 3.3): Even if the velocity field is not a solid body rotation, the rotation can be correctly evaluated by this method as long as the spatial scale of the velocity gradient (shear) is large.
3) From the experiment with a sinusoidal oscillation in a single direction (section 3.4): If the spatial scale is smaller than the tracking region and the velocity structure is not vortex-like, the amplitude of the rotation rate is considerably underestimated,

while spatial patterns are well reproduced.

4) From the experiment with the combination of the sinusoidal oscillations in latitudinal and longitudinal directions (section 3.5): If the velocity field includes vortex-like structures, the rotation rates at those vortices can be relatively well retrieved even if the spatial scale is smaller than the tracking region (Case 1). When the scale of the velocity structure is decreased, the number of missing cloud tracking vectors increases, and thus the spatial pattern of the vorticity becomes difficult to obtain. Even in this case, however, the spatial pattern of the rotation rate can be relatively well retrieved although its amplitude is underestimated (Cases 2 and 3).

It was demonstrated that the newly-developed method can directly extract the spatial pattern of rotational motions. Although the amplitudes of small-scale vortices can be underestimated, it is possible to visualize spatial patterns that cannot be observed in the vorticity map that is constructed from cloud-tracked velocities.

4. Applications to planetary atmosphere images

4.1 Cloud tracking for Jupiter

4.1.1 Data set

The newly-developed method was applied to Jupiter using near-infrared (750-nm) images taken by the Imaging Science Subsystem (ISS) during its Jupiter flyby in December 11, 2000 to December 13, 2000 on the way to Saturn. This data was taken when Cassini was closest to Jupiter and was approximately 140 Jupiter radii away. In this study, cloud tracking was performed using 750-nm images. The data was downloaded from NASA's data archive (https://atmos.nmsu.edu/PDS/review/Jupiter/Cassini_Maps/).

The images have been mapped onto the System III longitude-latitude coordinate with grid intervals of 0.05° both in the latitude and the longitude, matching the effective resolution of the original images. In this study, cloud tracking was performed using images taken at a time interval of approximately 63 min; Jupiter rotates by about 38° during this time. As a pre-process, high-pass filter is applied. The images were smoothed by a Gaussian filter with HWHM of 16 × 16 pixels that correspond to 0.8 ° longitude and latitude for Jupiter, and the smoothed image is subtracted from the original to produce an image in which fine structures are emphasized. The size of the tracking region is 64×64 pixels, that correspond to 3.2° ×3.2° in latitude and longitude.

4.1.2 Results

Figure 29 shows a result of applying the new method to the low latitude region within ± 20° latitude. The high-pass processed image, the rotation rate and the velocity obtained by cloud tracking are shown. A rotation rate of 1×10^{-5} rad s^{-1} corresponds to 2 deg h^{-1}. Longitudinally-elongated banded structures peculiar to Jupiter are seen both in the velocity and the rotation rate. It is noteworthy that intense small-scale vortices with sizes of ~1° (1250 km) exist near the equator. I focus on this region below.

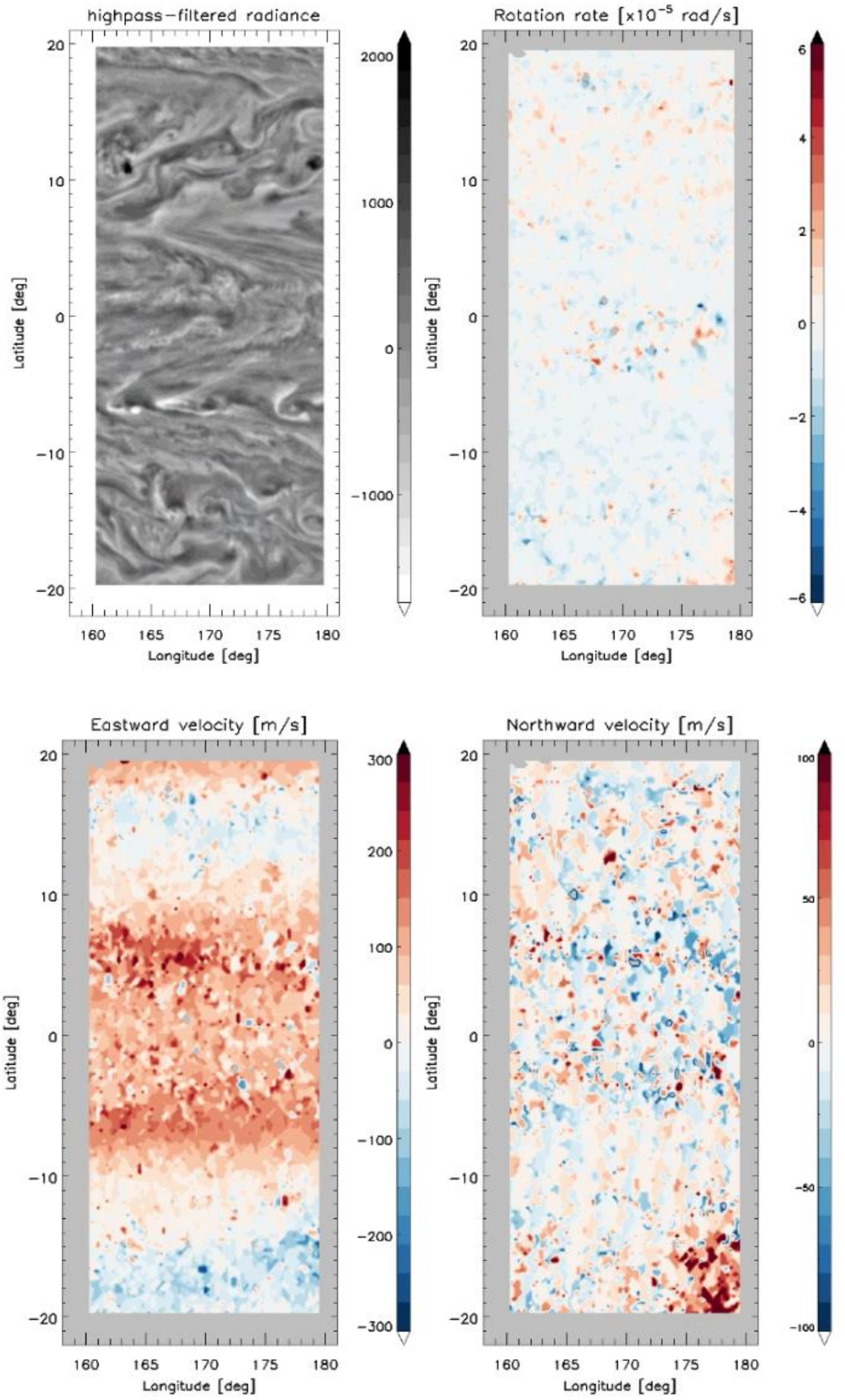

Figure 29. (top left) High-pass processed 750-nm image of Jupiter, (top right) the rotation rate obtained by the proposed method, (bottom left) the zonal velocity obtained by cloud tracking and (bottom right) the meridional velocity. A pair of images taken at 18:54 and 19:51 on December 11, 2000 were used.

Figures 30-36 show results for the equatorial region with a wider longitudinal coverage. The time interval between the image pairs is ~1 h. Chains of small-scale vortices with sizes of about 1° in latitude and longitude tend to appear around 5°N and 2-5°S. Such small vortices are not seen in the past cloud tracking results (Figure 7). The typical magnitude of the rotation rate in the small vortices is $\sim\mathbf{3.0 \times 10^{-5}\ rad\ s^{-1}}$, which is greater than the expected error of $\mathbf{0.12 \times 10^{-5}\ rad\ s^{-1}}$. As for the correspondence with the cloud pattern, small vortices tend to exist in regions where streaky patterns are less prominent. The cloud-tracked wind field shows a westward wind of about 100 m/s in this region, and the zonal wind peaks around the latitudes around ± 5°, being consistent with the previous results (e.g., Simon et al. 2015). It is noteworthy that the locations of small-scale vortices seem to roughly correspond to the zonal wind maxima. This point will be discussed in section 5.

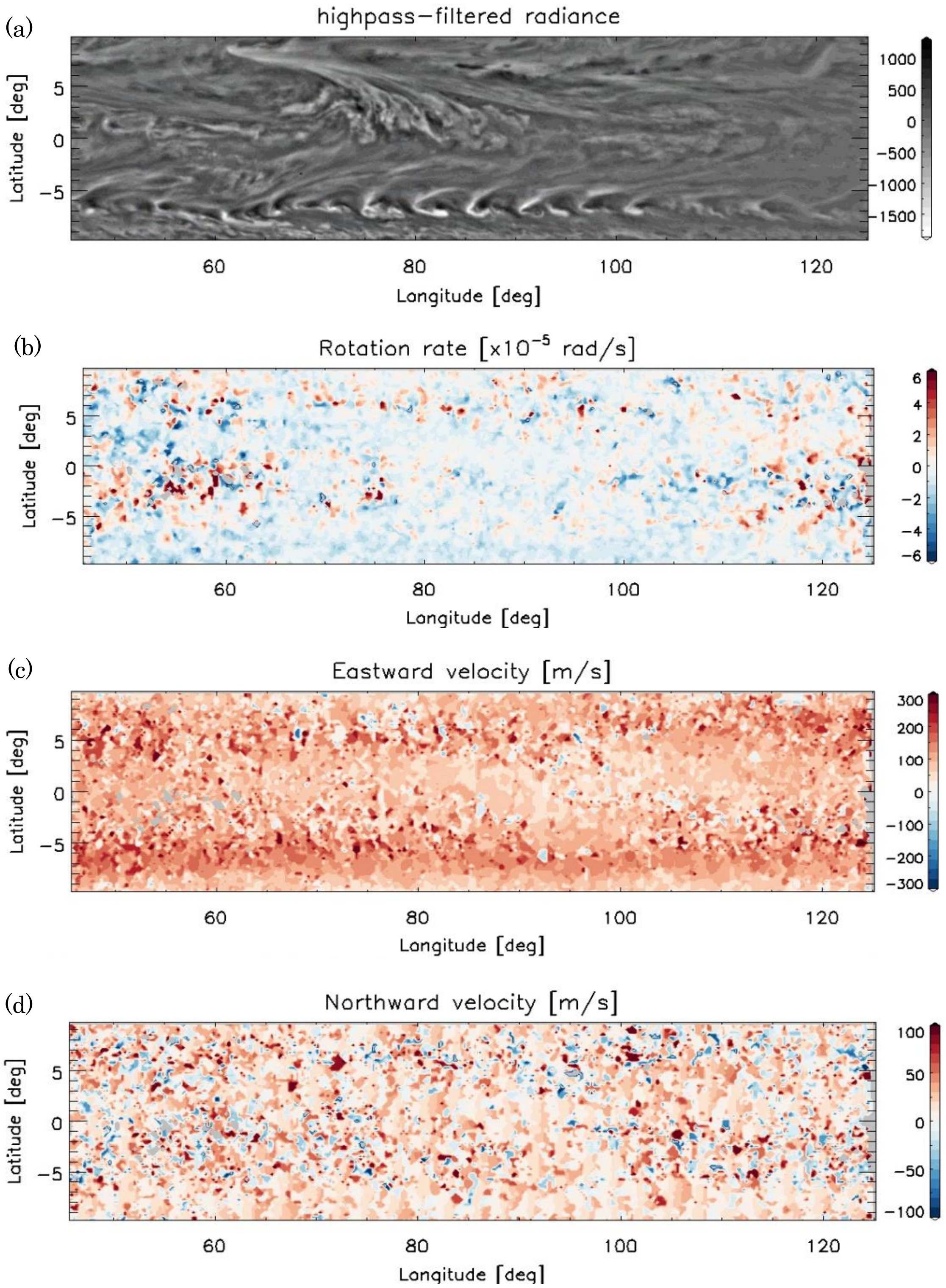

Figure 30. (a) High-pass processed 750-nm image of Jupiter, (b) the rotation rate obtained by the proposed method, (c) the zonal velocity obtained by cloud tracking and (d) the meridional velocity obtained by cloud tracking. A pair of images taken at 21: 01 and 21:57 on December 11, 2000 were used.

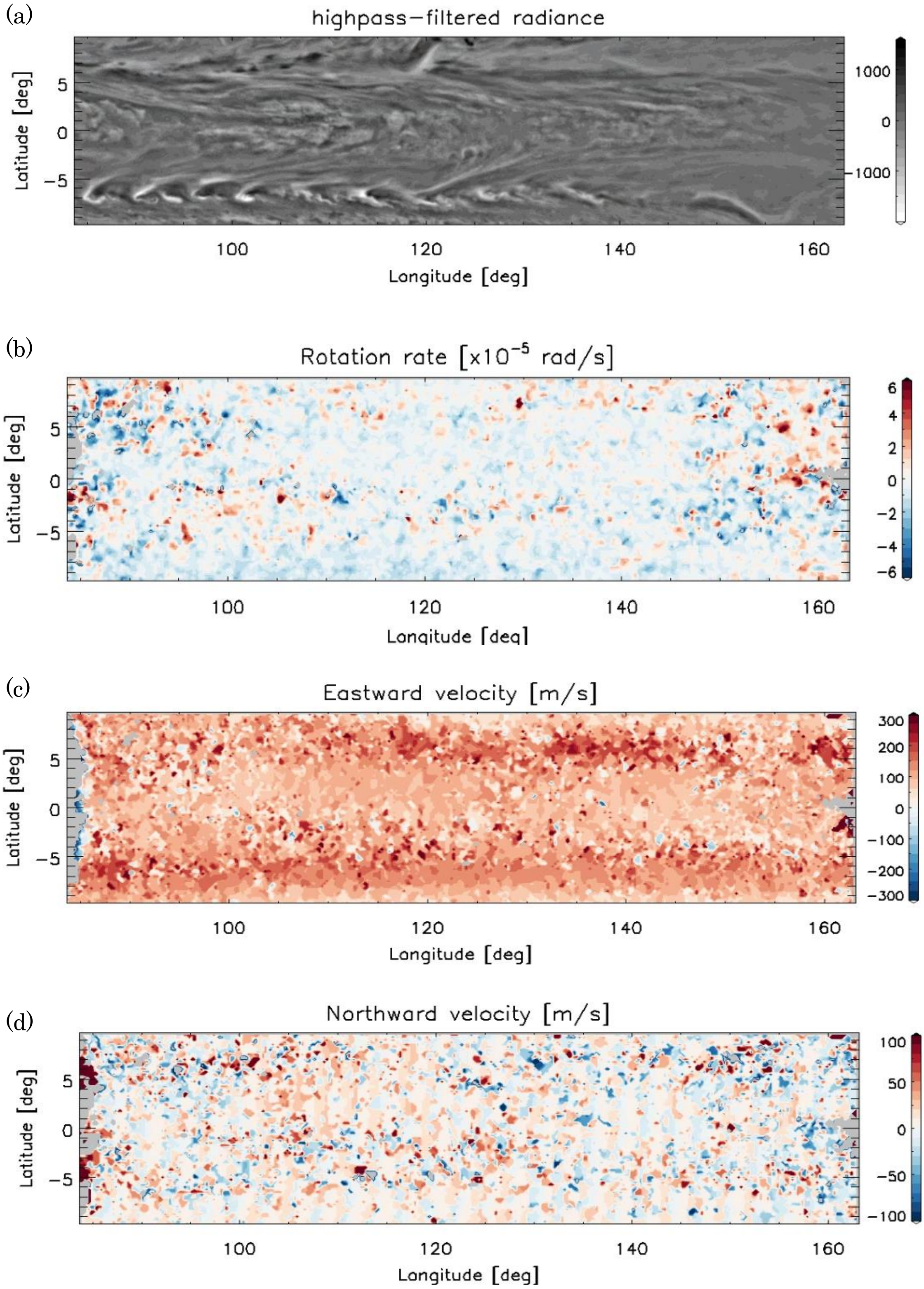

Figure 31. Same as Figure 30, but for the images taken at 22:04 and 23:00 on December 11, 2000.

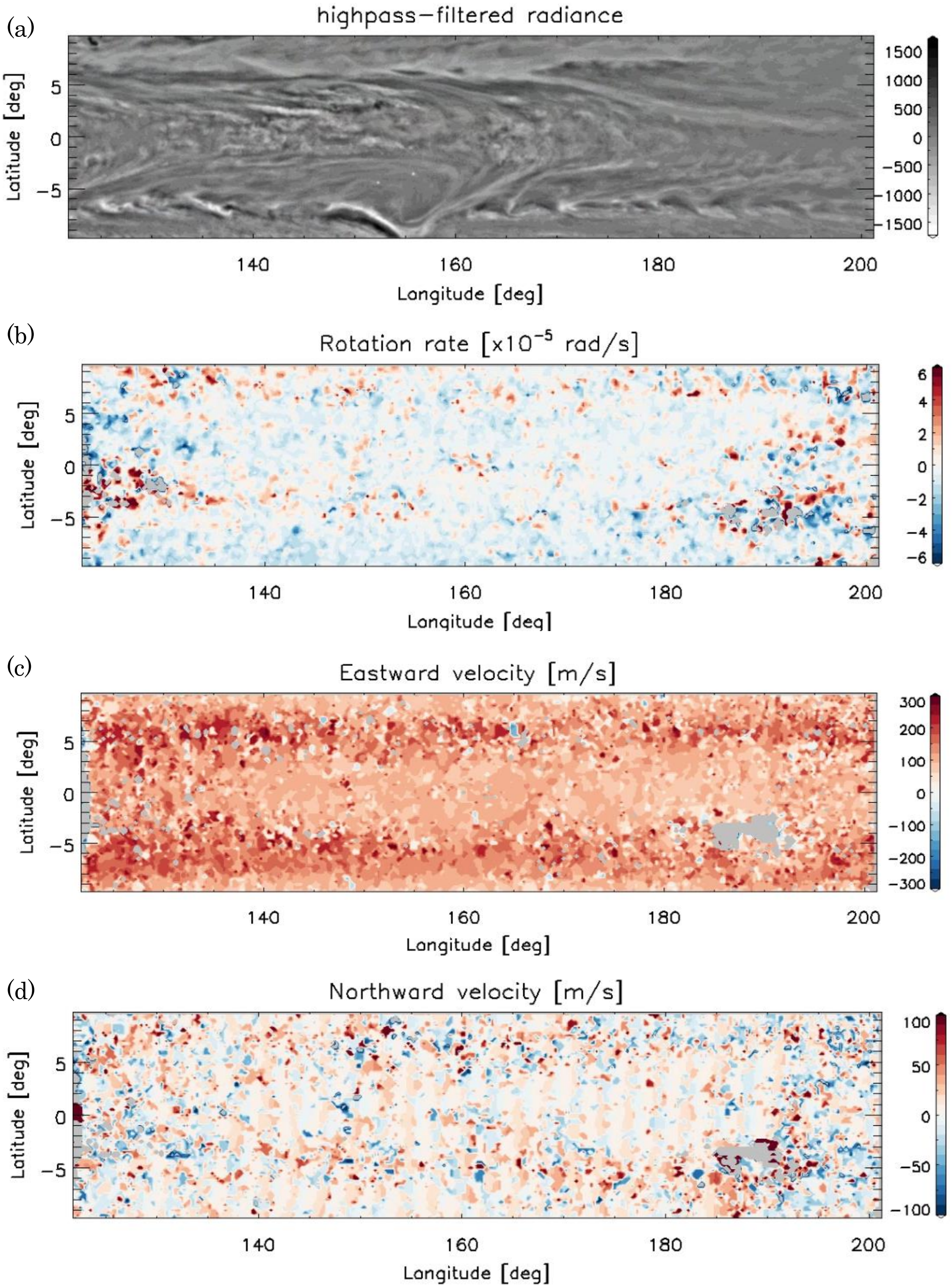

Figure 32. Same as Figure 30, but for the images taken at 23:07 on December 11, 2000 and 00:03 on December 12, 2000.

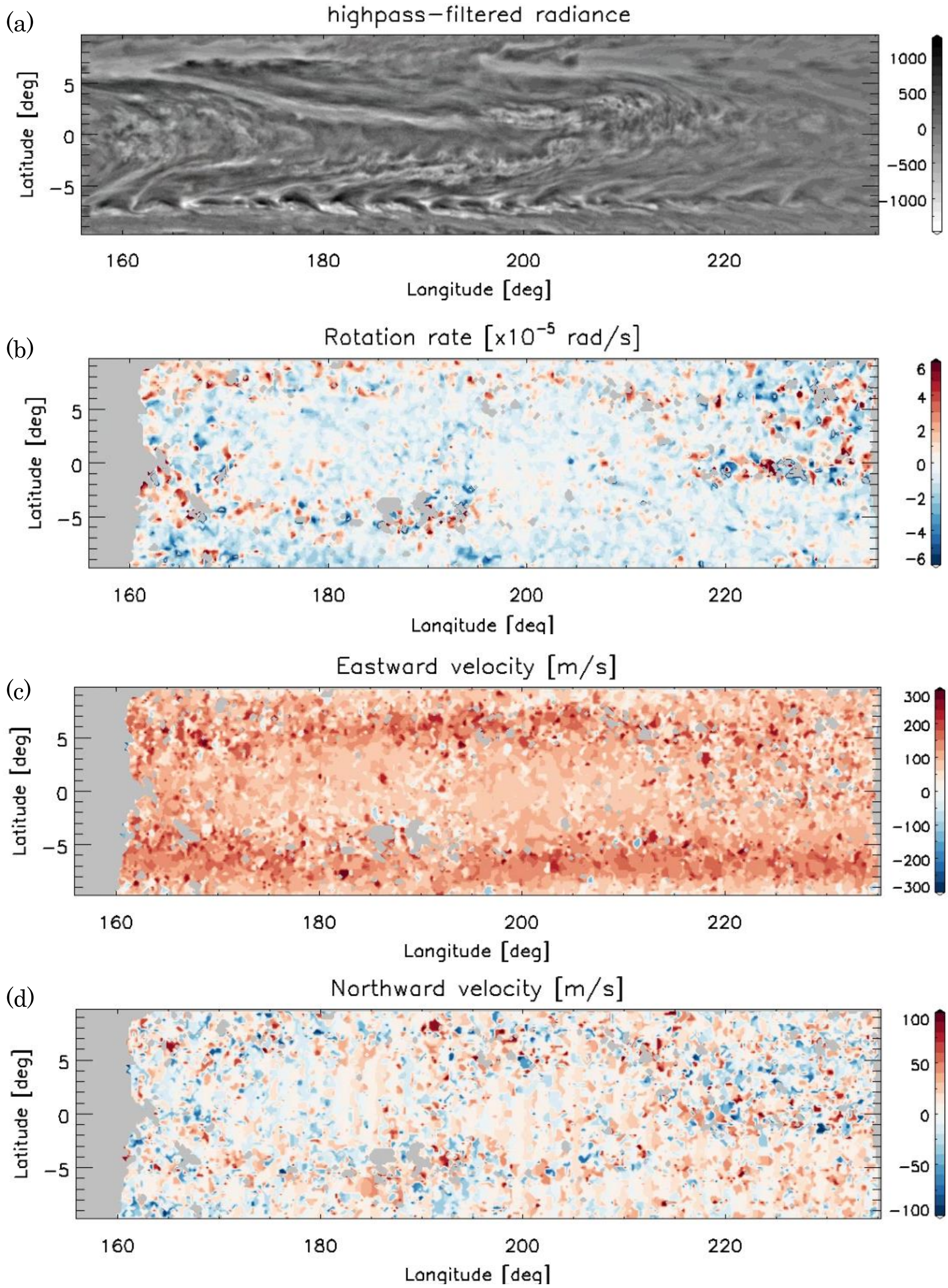

Figure 33. Same as Figure 30, but for the images taken at 00:03 and 01:06 on December 12, 2000.

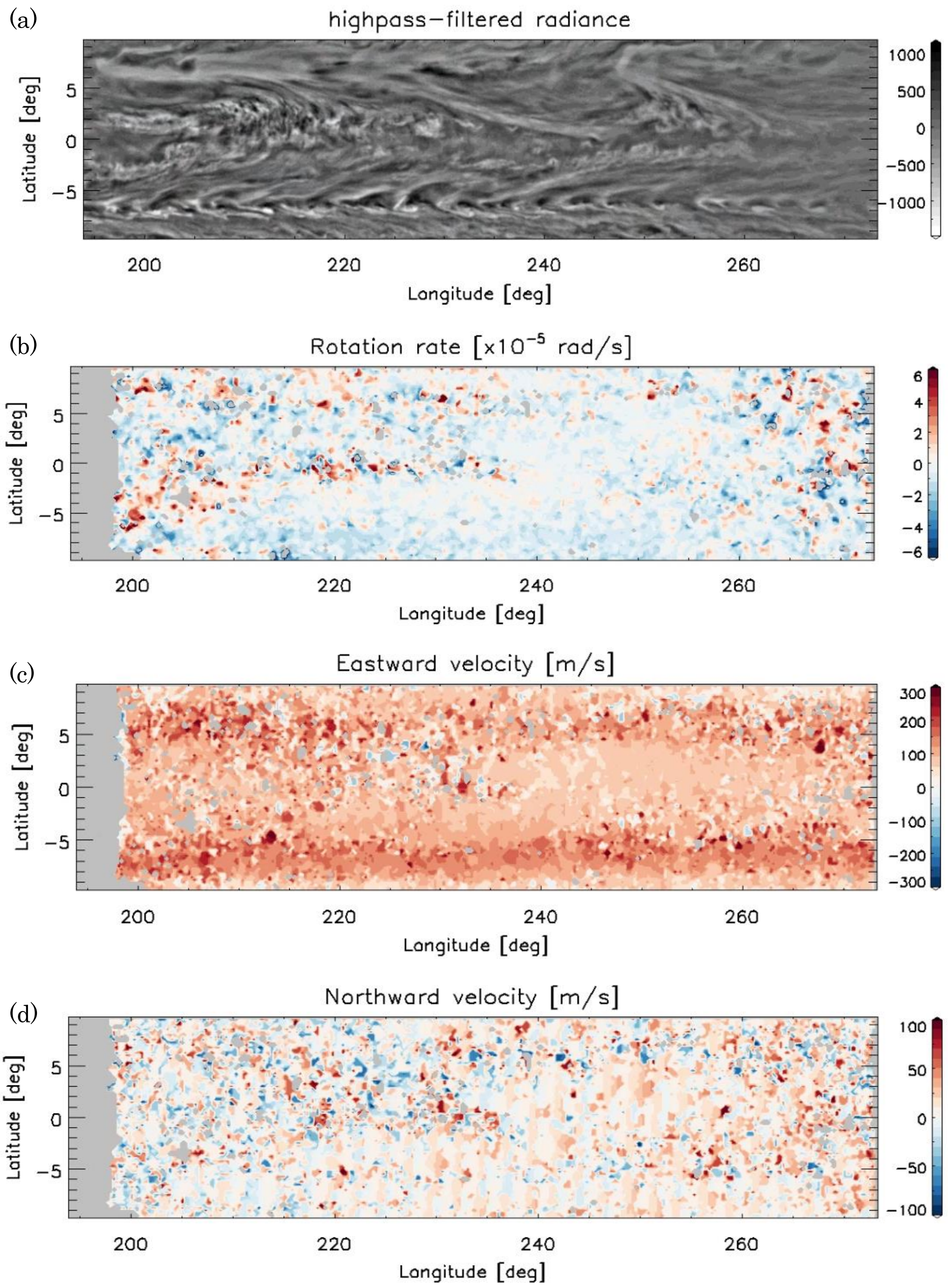

Figure 34. Same as Figure 30, but for the images taken at 01:06 and 02:09 on December 12, 2000.

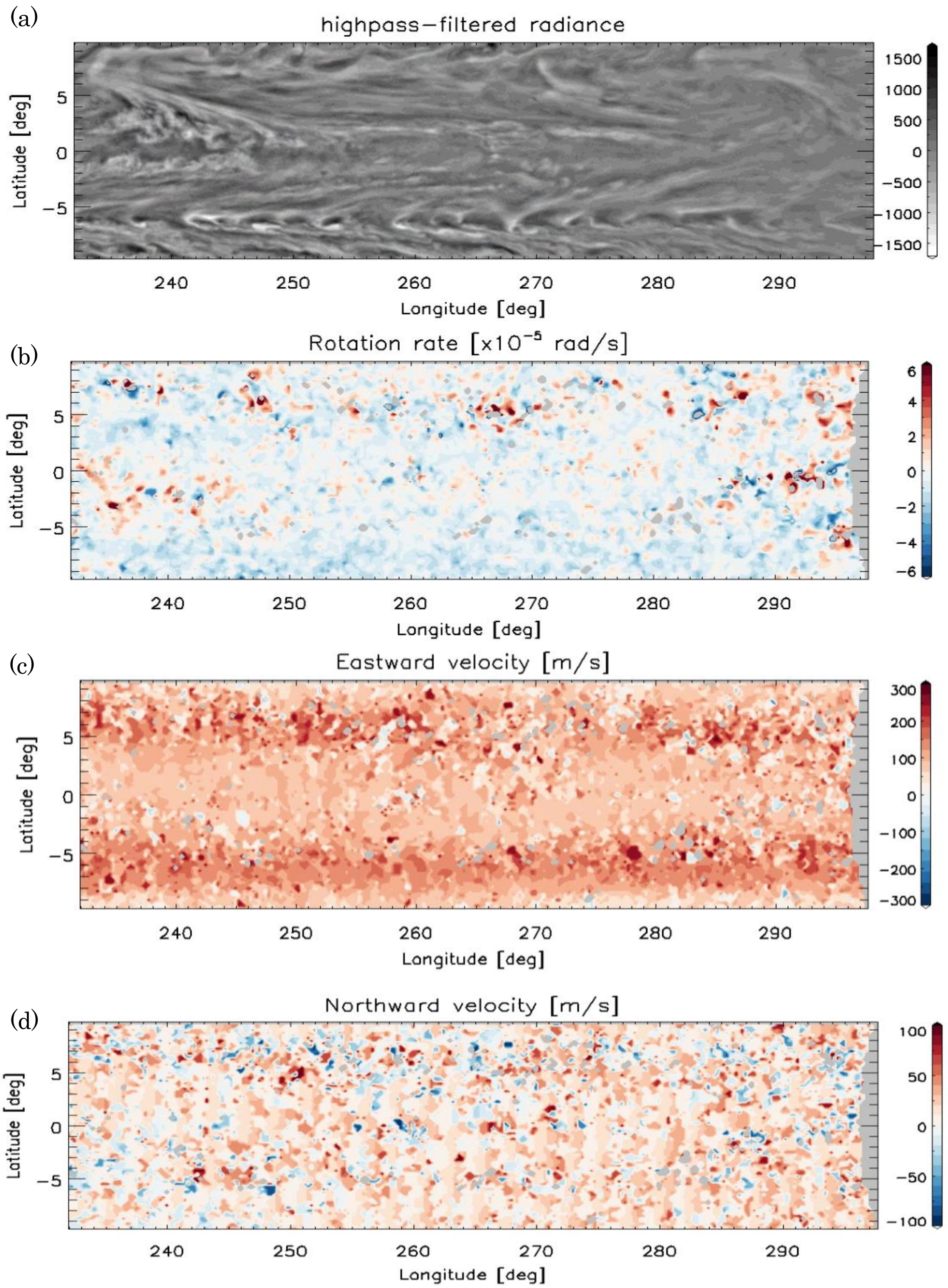

Figure 35. Same as Figure 30, but for the images taken at 02:09 and 03:12 on December 12, 2000.

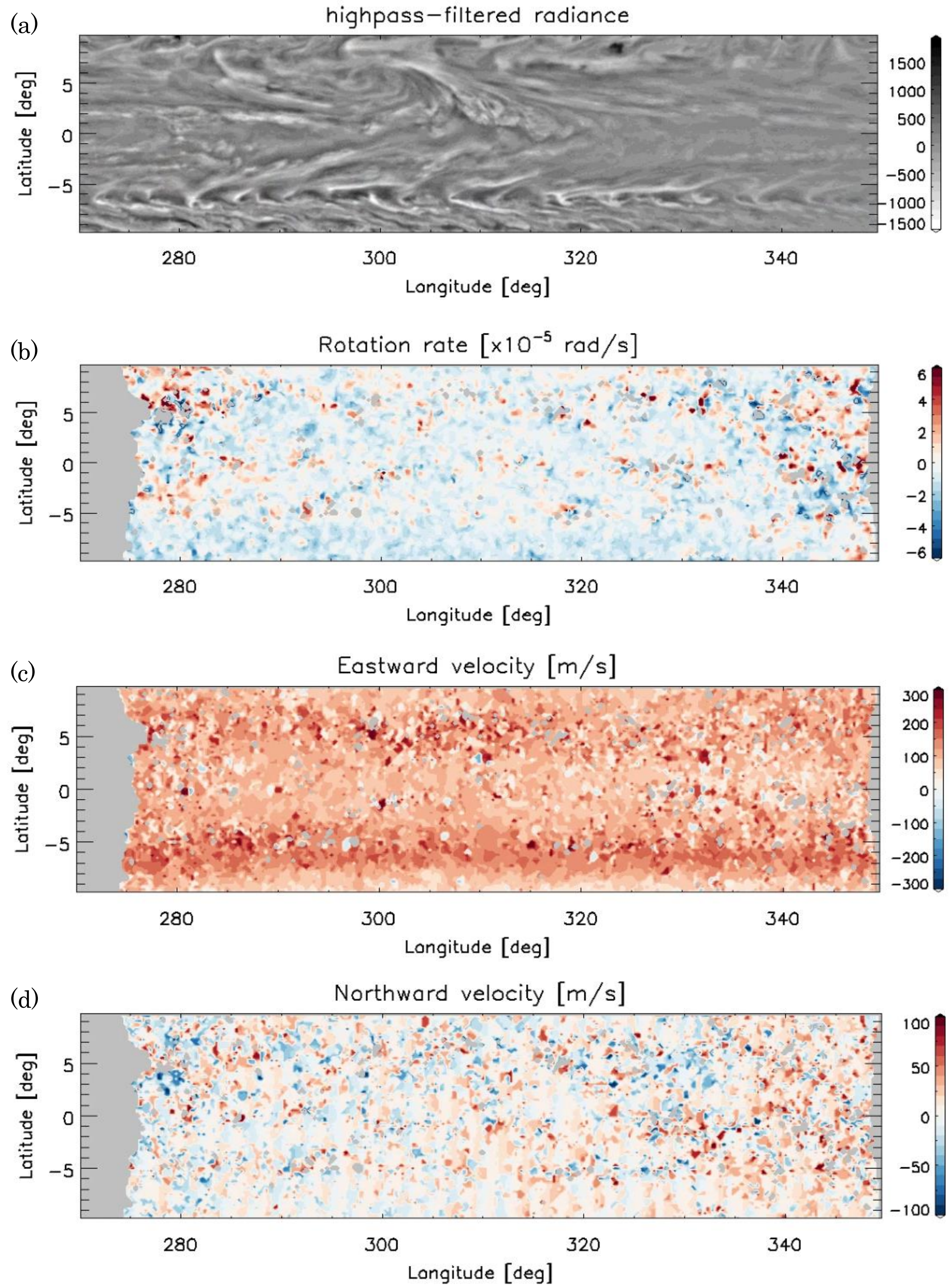

Figure 36. Same as Figure 30, but for the images taken at 03:12 and 04:15 on December 12, 2000.

To evaluate to what extent the obtained rotation rate reflects real atmospheric variations, the spatial spectra of the rotation rate are examined: random noise has a flat spectrum, while real dynamical processes are expected to have a red spectrum in which larger eddies have larger amplitudes through nonlinear interaction (Nastrom and Gage 1985). Figure 37 shows the Lomb-Scargle periodograms (Lomb, 1976; Scargle, 1982) of the longitudinal distributions of the rotation rate at four latitude band. This method is equivalent to least-squares fitting of sine and cosine functions to the data and allows us to obtain power spectra from unevenly sampled data with data gaps. Each spectrum is the average of 20 spectra of longitudinal cross sections evenly sampled from each 5°-width latitudinal band. For comparison, Figure 38 shows the average of 20 Lomb-scargle spectra of random data having the same length as the rotation rate used in Figure 39. The random data shows almost flat (white) spectrum as expected, while the rotation rate shows a red spectrum represented by a power law up to the wavelength of ~4° and a flattening at longer wavelengths. The rapid decline of the power on the short wavelength side is partly attributed to the underestimation of the amplitude for scales smaller than the tracking region (section 3). The result suggests that most of the observed small-scale structures of the rotation rate are not noise arising from analysis error but real atmospheric disturbances.

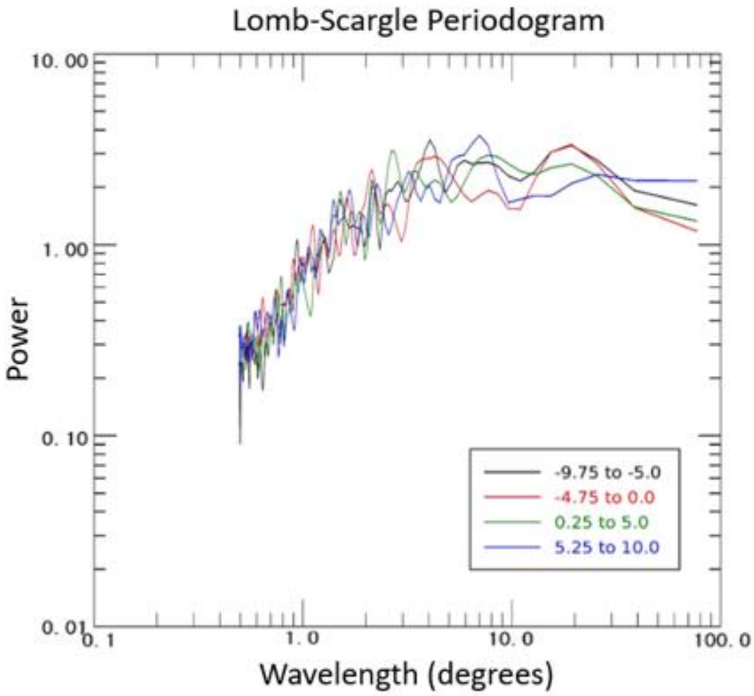

Figure 37. Lomb-Scargle periodograms of the longitudinal cross sections of the rotation rate at four different latitude bands obtained from the data shown in Figure 30. Each spectrum is the average of 20 spectra.

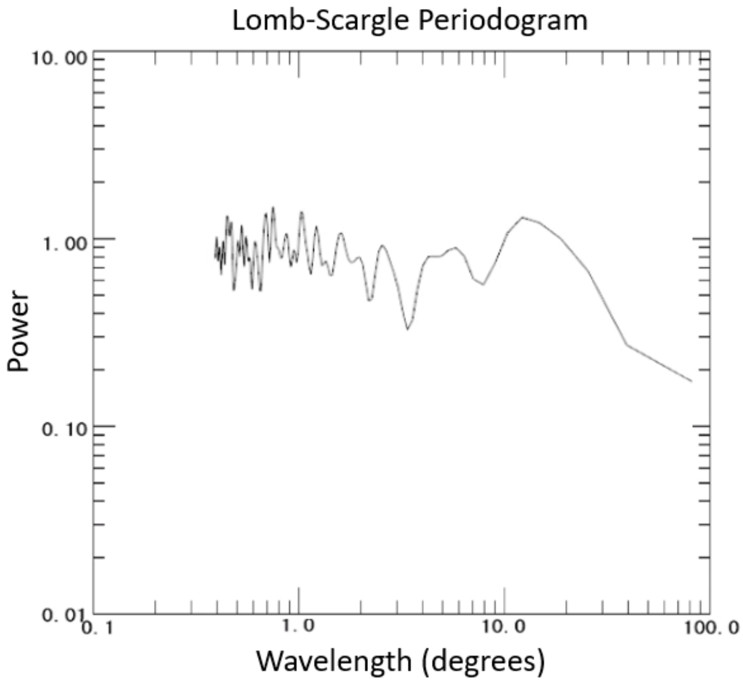

Figure 38. Lomb-Scargle periodogram of random data.

4.2 Cloud tracking for Venus

4.2.1 Data set

The newly-developed method was applied to Venus using ultraviolet (365-nm) images taken by the Ultraviolet Imager (UVI) onboard JAXA's Akatsuki spacecraft.

The data was downloaded from JAXA's data archive (https://darts.isas.jaxa.jp/pub/doi/VCO-00016.html). Cloud tracking was performed using images taken at a time interval of about 2 hours on August 3, 2016. The images have been mapped onto the longitude-latitude coordinate with grid intervals of 0.125° both in the latitude and the longitude. In this study, cloud tracking was performed using 365-nm images taken at a time interval of approximately 2 hours, and clouds rotate by about 7.5° during this time considering the mean zonal wind speed associated with the superrotation of the atmosphere (Schubert et al. 1980). Cloud tracking was performed in regions where the incident angle is less than 70°, the emission angle is less than 65° and latitude is within ± 50° because cloud tracking is difficult at high latitudes where streak patterns are dominant. As a pre-process, high-pass filter is applied. The images were smoothed by a Gaussian filter with HWHM of 16 × 16 pixels that correspond to 2° longitude and latitude for Venus, and the smoothed image is subtracted from the original to produce an image in which fine structures are emphasized. The size of the tracking region is 64×64 pixels, that correspond to 8° ×8° in latitude and longitude.

4.2.2 Results

The results are shown in Figures 39-48. As for the results from the data taken on November 16, 2018, the first 10 sets are shown in Figures 49-58. Each figure shows the image after high-pass processing, the velocity obtained by cloud tracking and the rotation rate. From these results, the rotation rate shows a hemispherically-symmetric structure with anticlockwise rotation in the northern hemisphere and clockwise rotation in the southern hemisphere. This is attributed to the increase of the angular velocity of the zonal flow with latitude up to 60° latitude in both hemispheres (Limaye 2007). In addition to this asymmetry, small-scale vortices are ubiquitously seen with larger amplitudes in the middle latitude than in the low latitude and change their distribution with time. The amplitude of the small-scale structures in the rotation rate is typically

1.0×10^{-5} rad s^{-1}, which is greater than the expected error (section 3). The zonal velocity is westward and around 100 m s^{-1}, being consistent with the superrotation. The meridional velocity shows planetary-scale (> 1000 km) structures.

Figures 59 and 60 show mosaics of the cloud images and the rotation rate maps constructed by utilizing the advection of the patterns by the superrotaion, whose recurrence period is ~4 Earth days. The characteristics mentioned before, i.e. the anticlockwise/clockwise rotation in the northern/southern hemisphere and the existence of small-scale vortices in the middle latitude, are ubiquitously seen over the whole cloud cover. The spatial pattern of the rotation rate does not notable correlation with the cloud pattern.

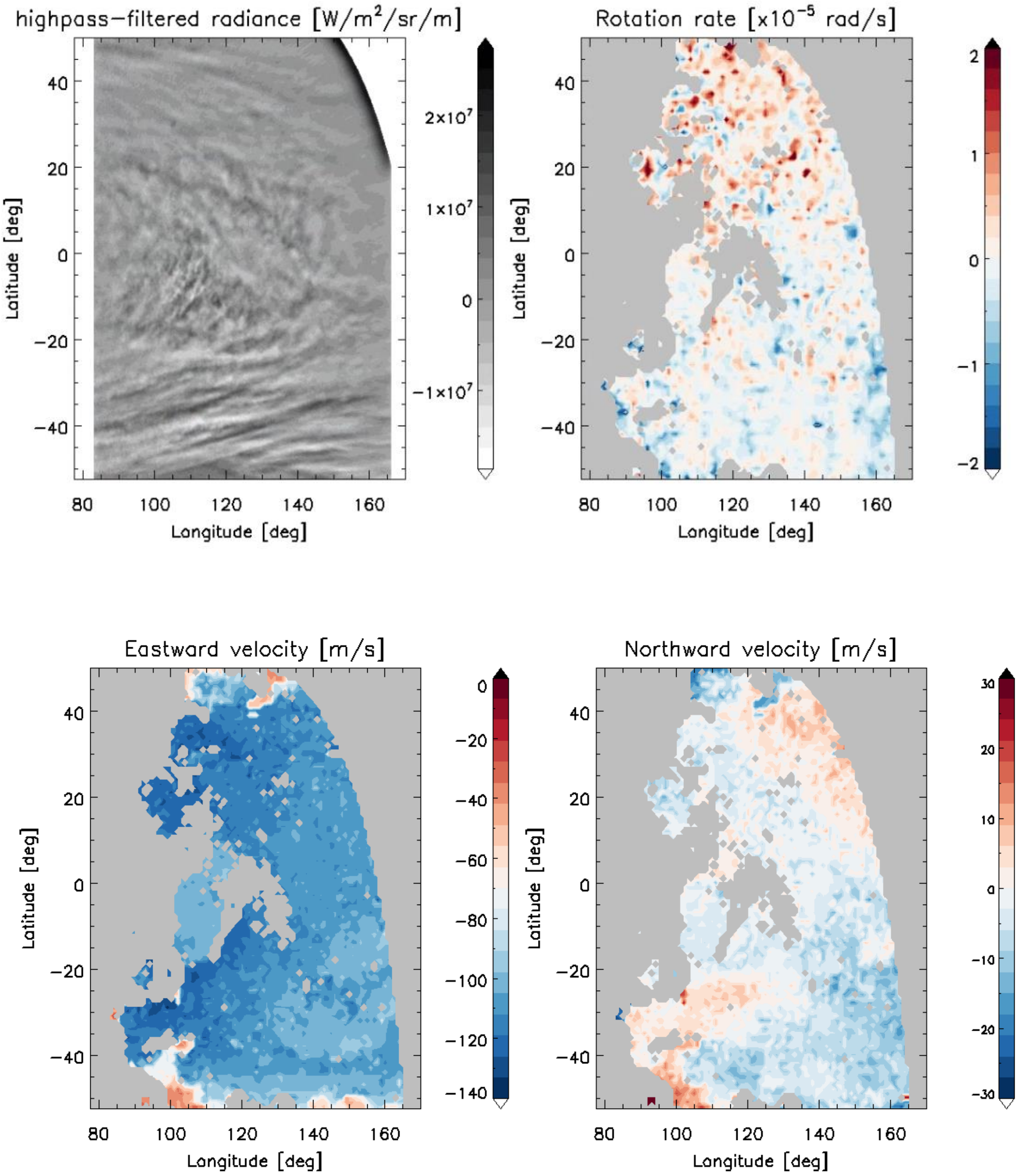

Figure 39. (top left) High-pass processed 365-nm image of Venus, (top right) the rotation rate obtained by the proposed method, (bottom left) the zonal velocity obtained by cloud tracking and (bottom right) the meridional velocity. A pair of images taken at 04:17 and 06:17 on August 3, 2016 were used.

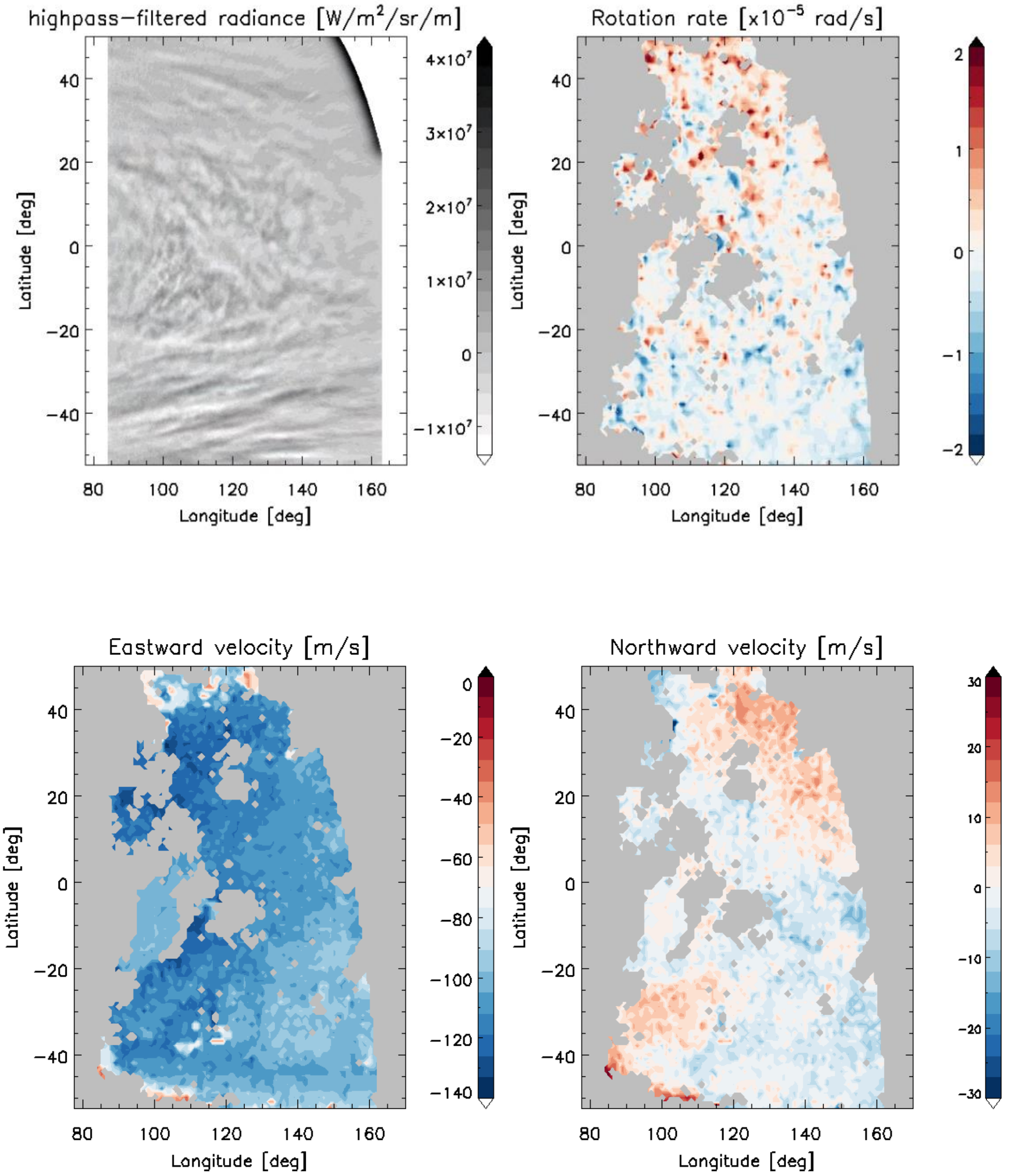

Figure 40. Same as Figure 39, but for the images taken at 06:17 and 08:17 on August 3, 2016.

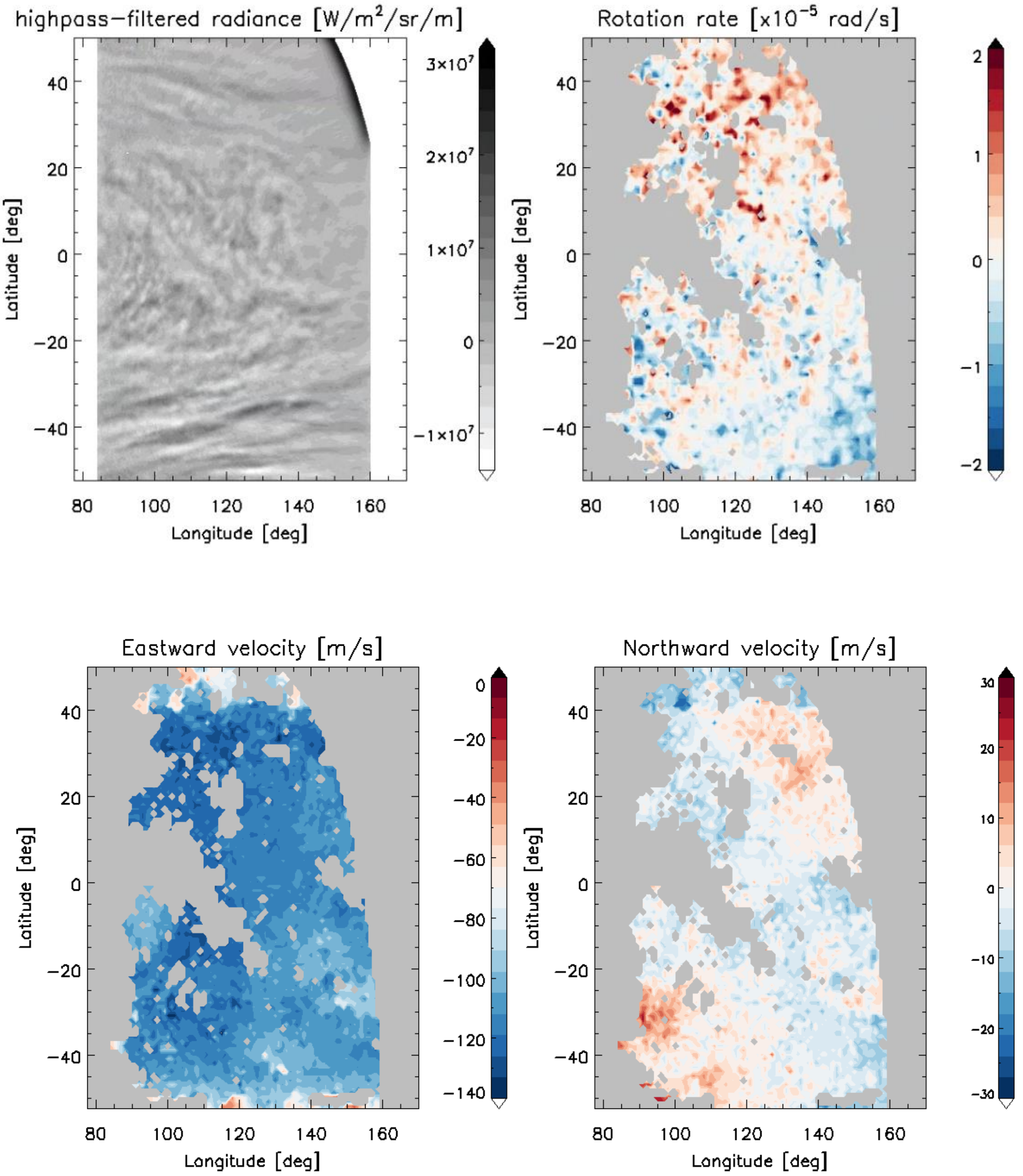

Figure 41. Same as Figure 39, but for the images taken at 08:17 and 10:17 on August 3, 2016.

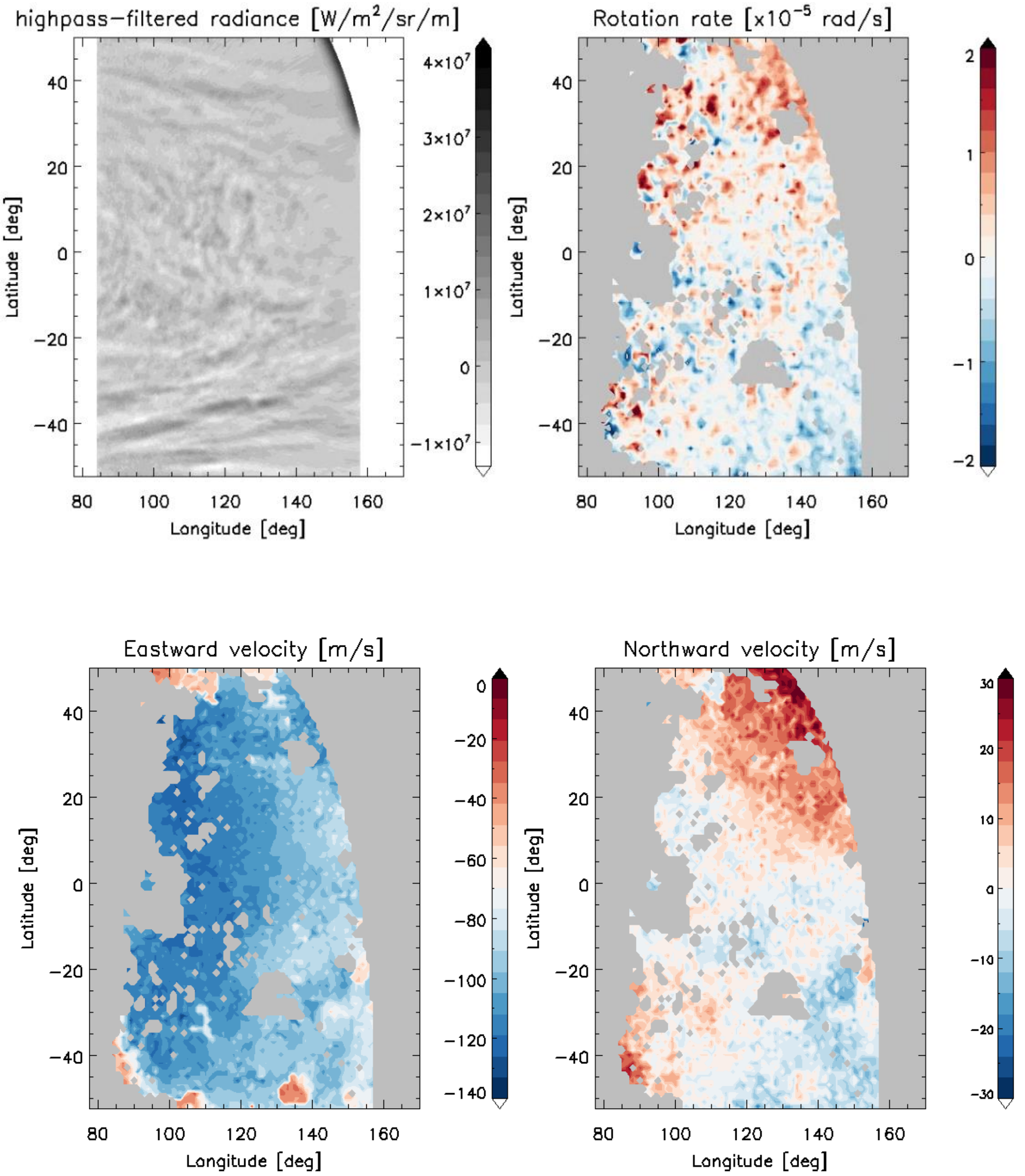

Figure 42. Same as Figure 39, but for the images taken at 10:17 and 12:17 on August 3, 2016.

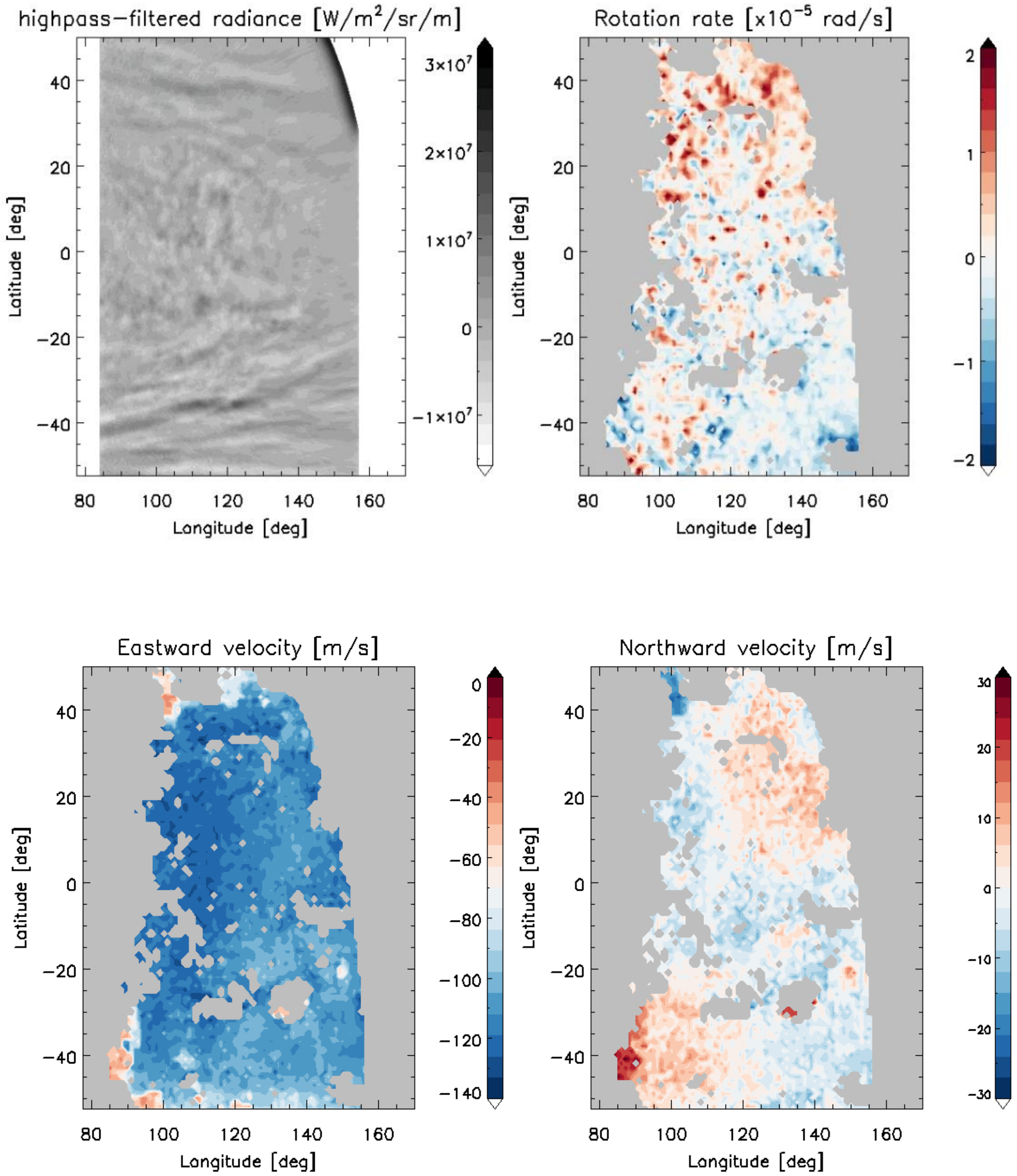

Figure 43. Same as Figure 39, but for the images taken at 12:17 and 14:17 on August 3, 2016.

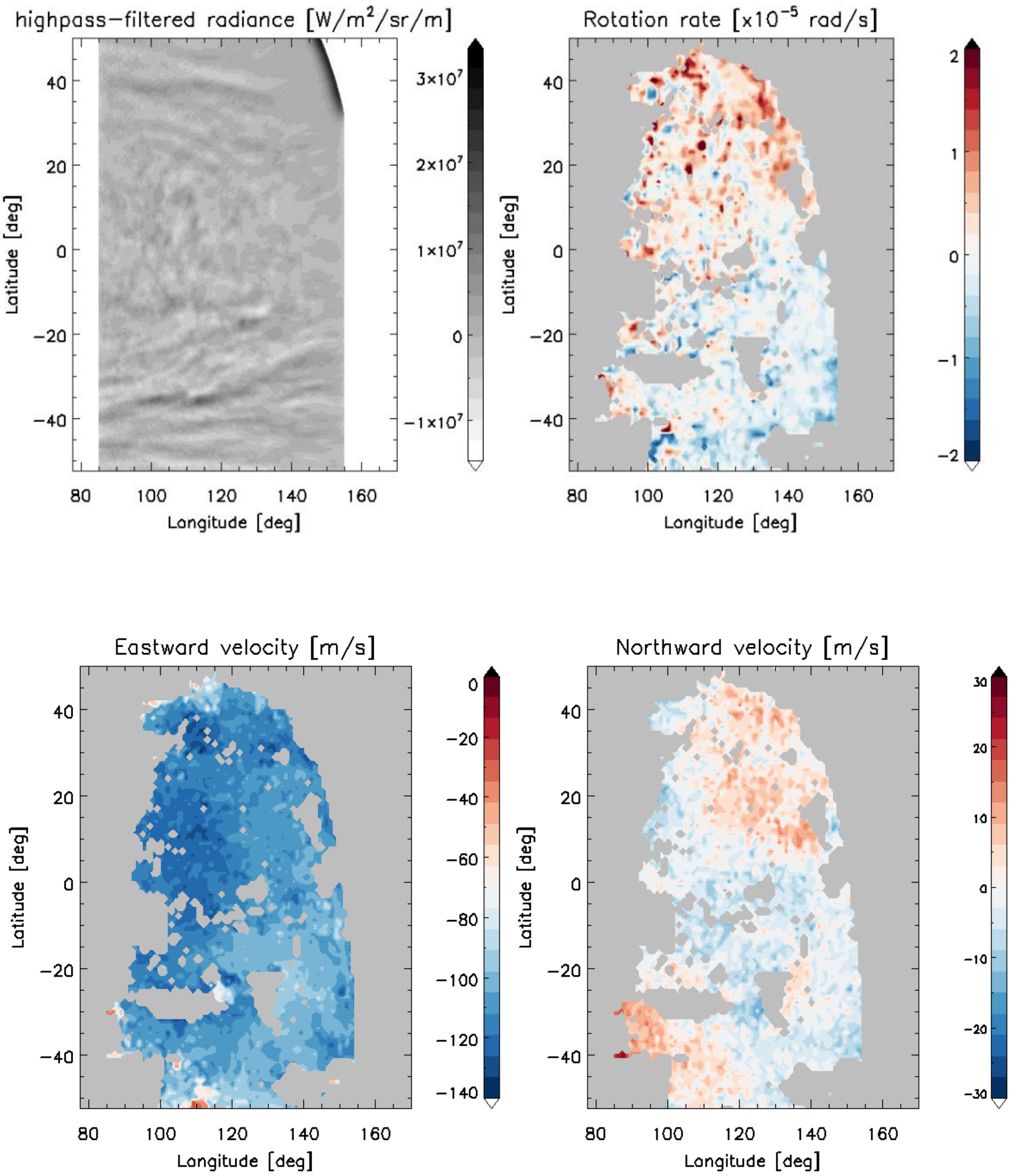

Figure 44. Same as Figure 39, but for the images taken at 14:17 and 16:17 on August 3, 2016.

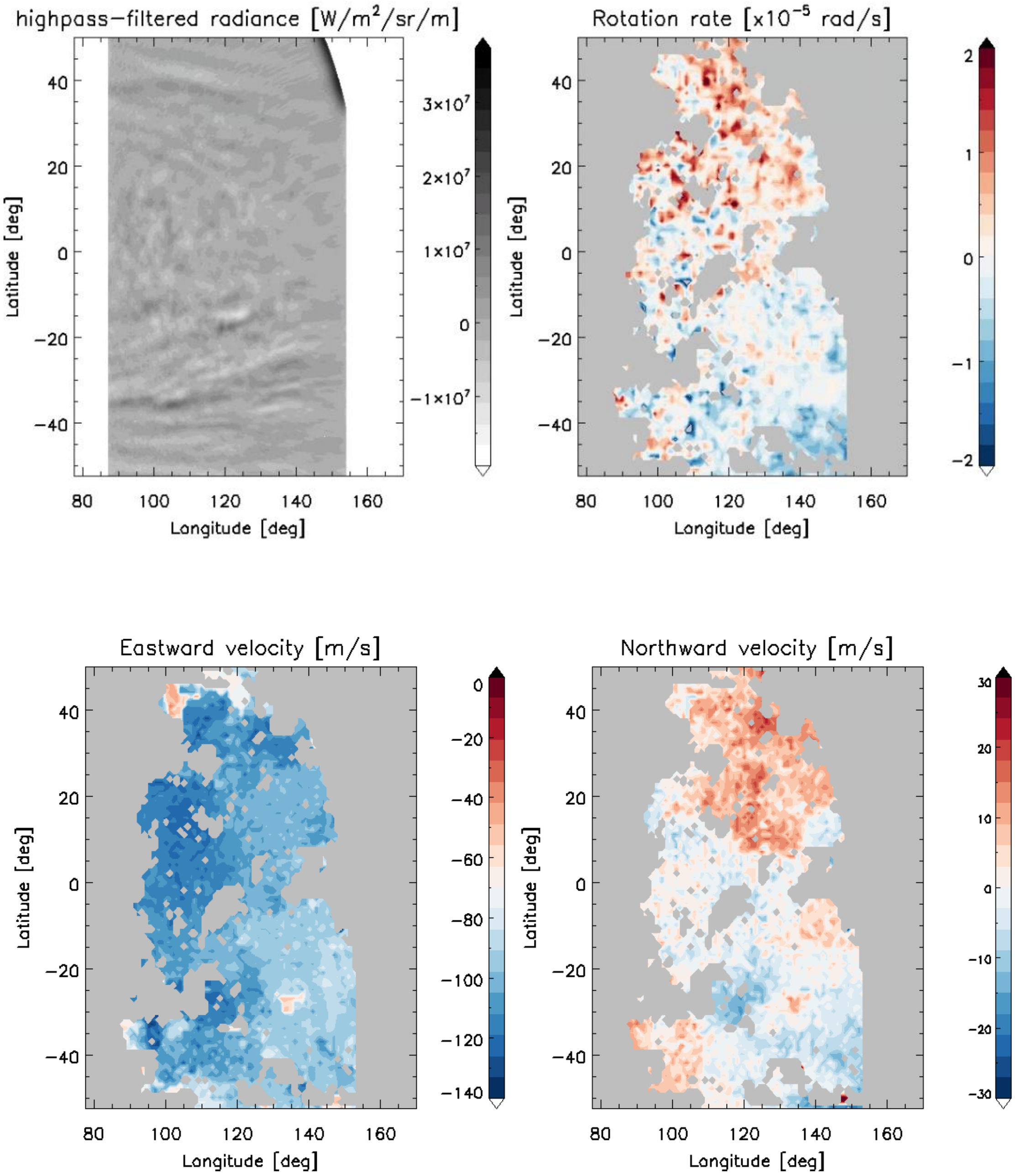

Figure 45. Same as Figure 39, but for the images taken at 16:17 and 18:17 on August 3, 2016.

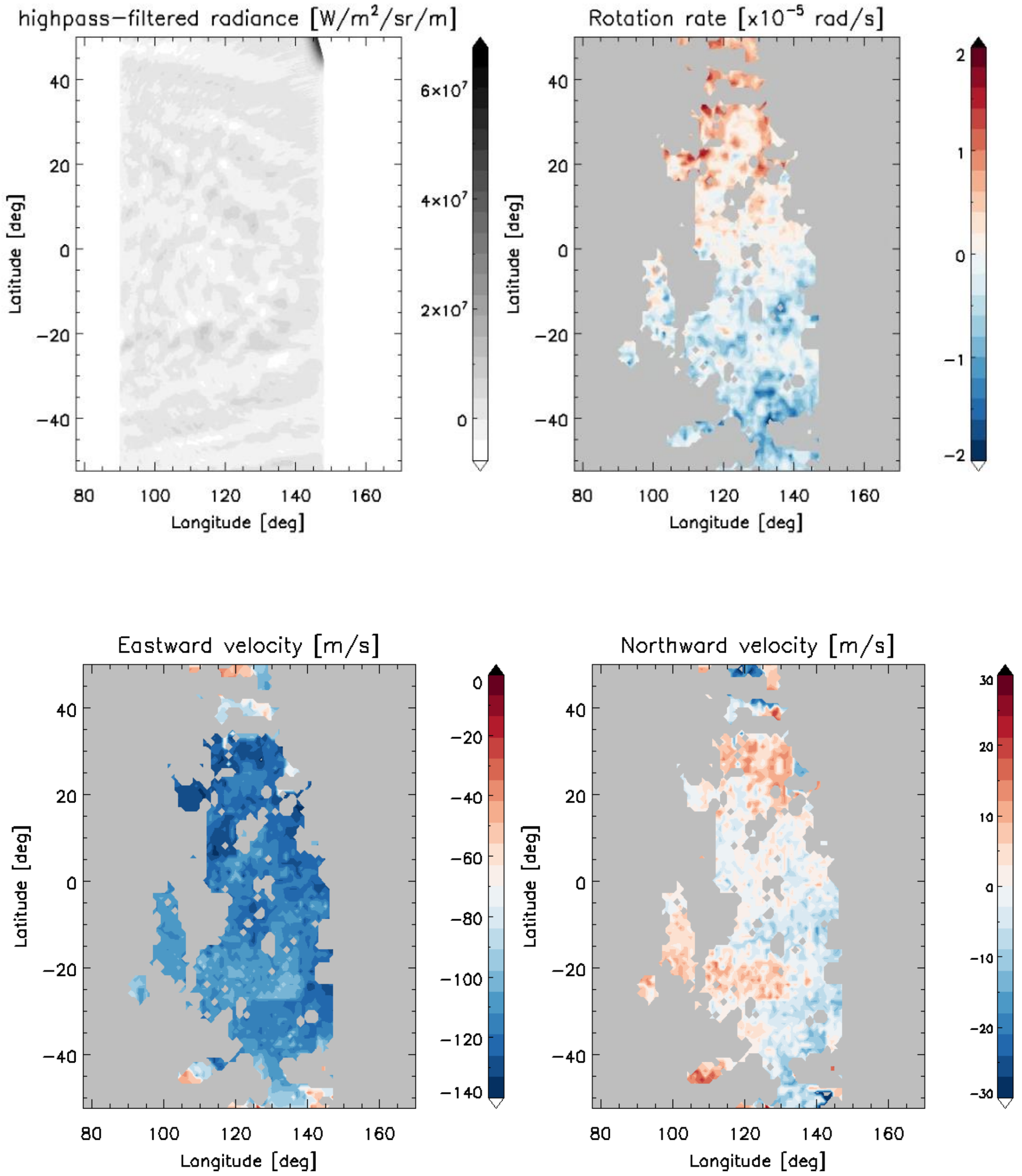

Figure 46. Same as Figure 39, but for the images taken at 11:17 and 13:17 on August 4, 2016.

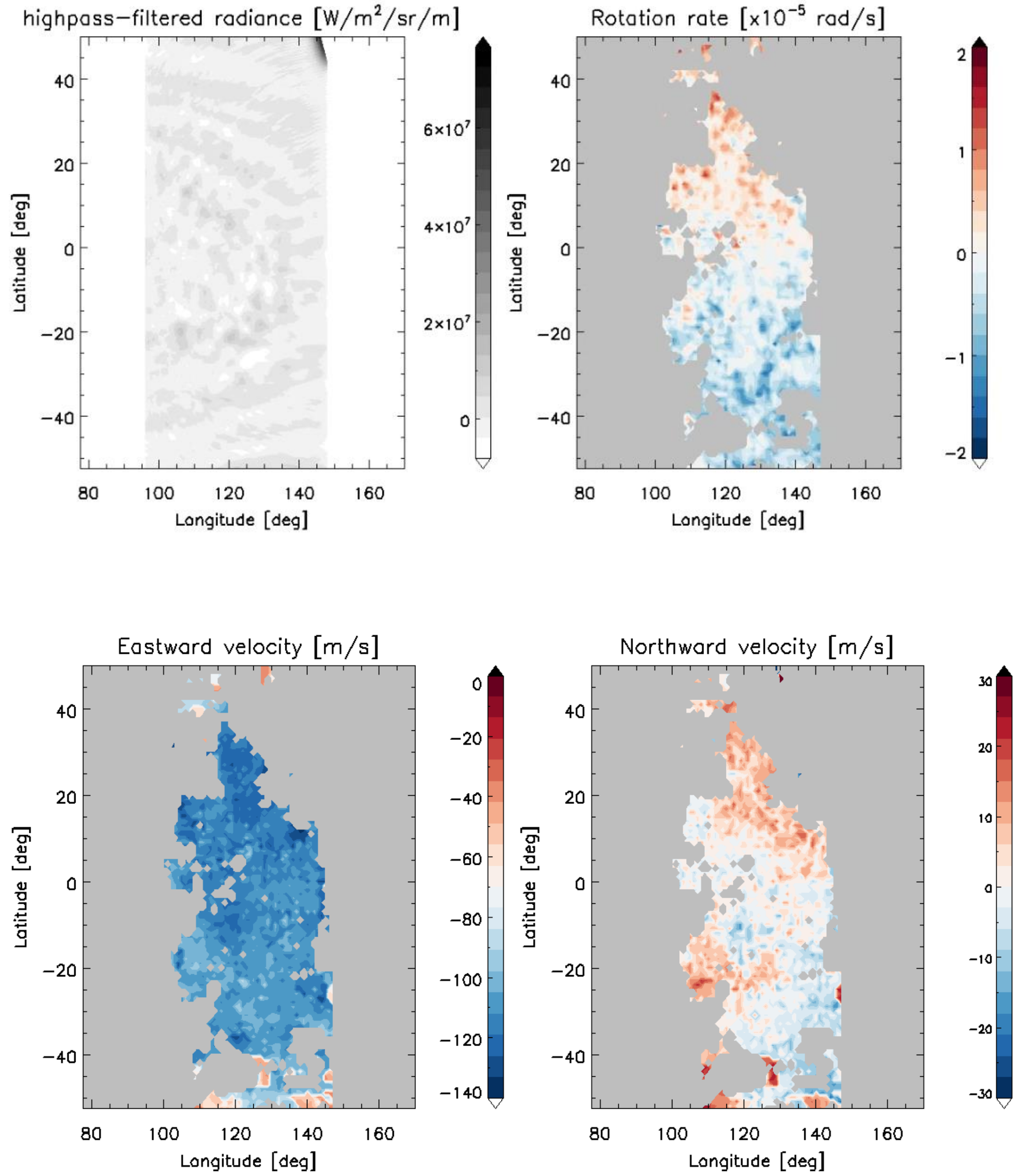

Figure 47. Same as Figure 39, but for the images taken at 13:17 and 15:17 on August 4, 2016.

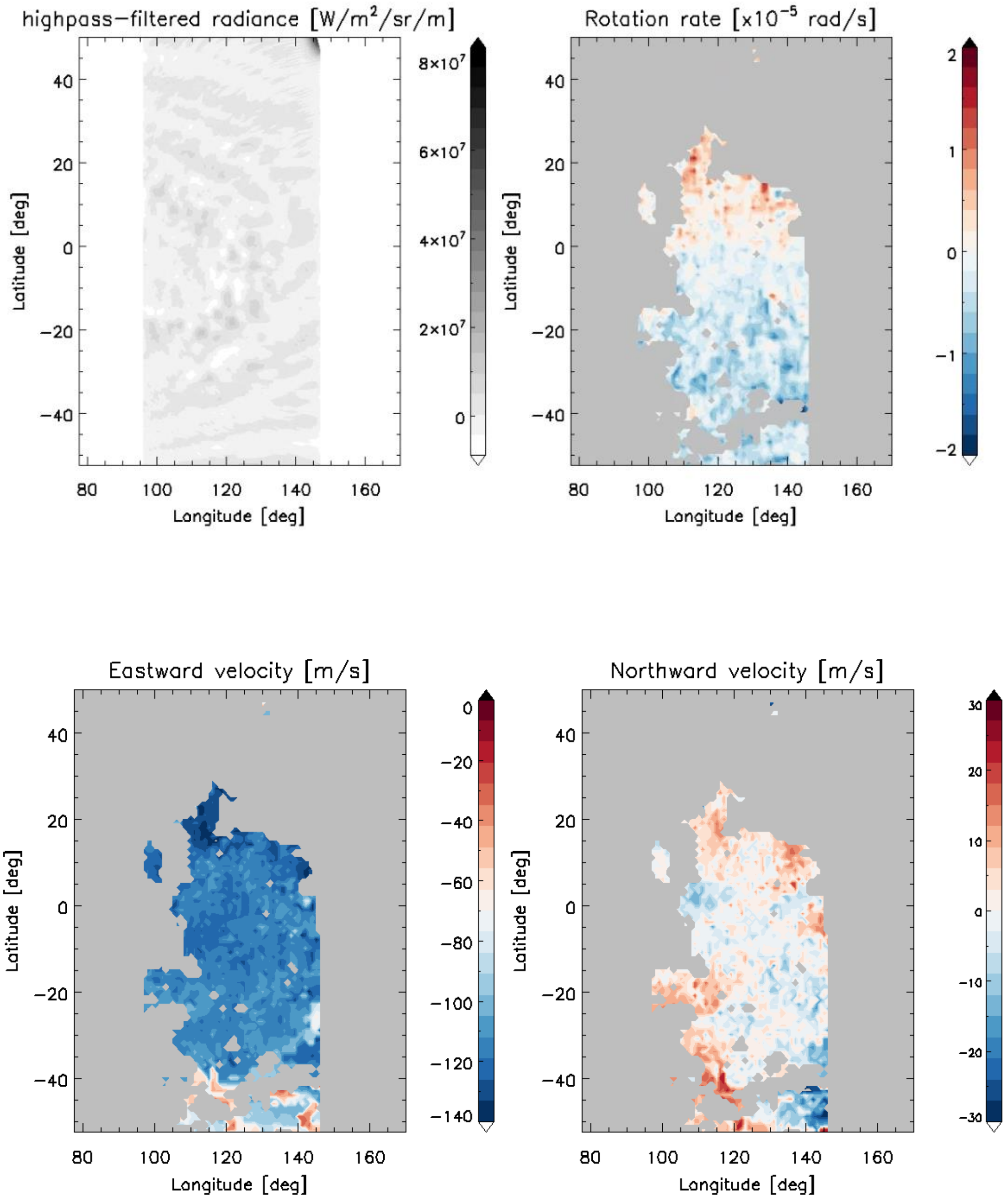

Figure 48. Same as Figure 39, but for the images taken at 15:17 and 17:17 on August 4, 2016.

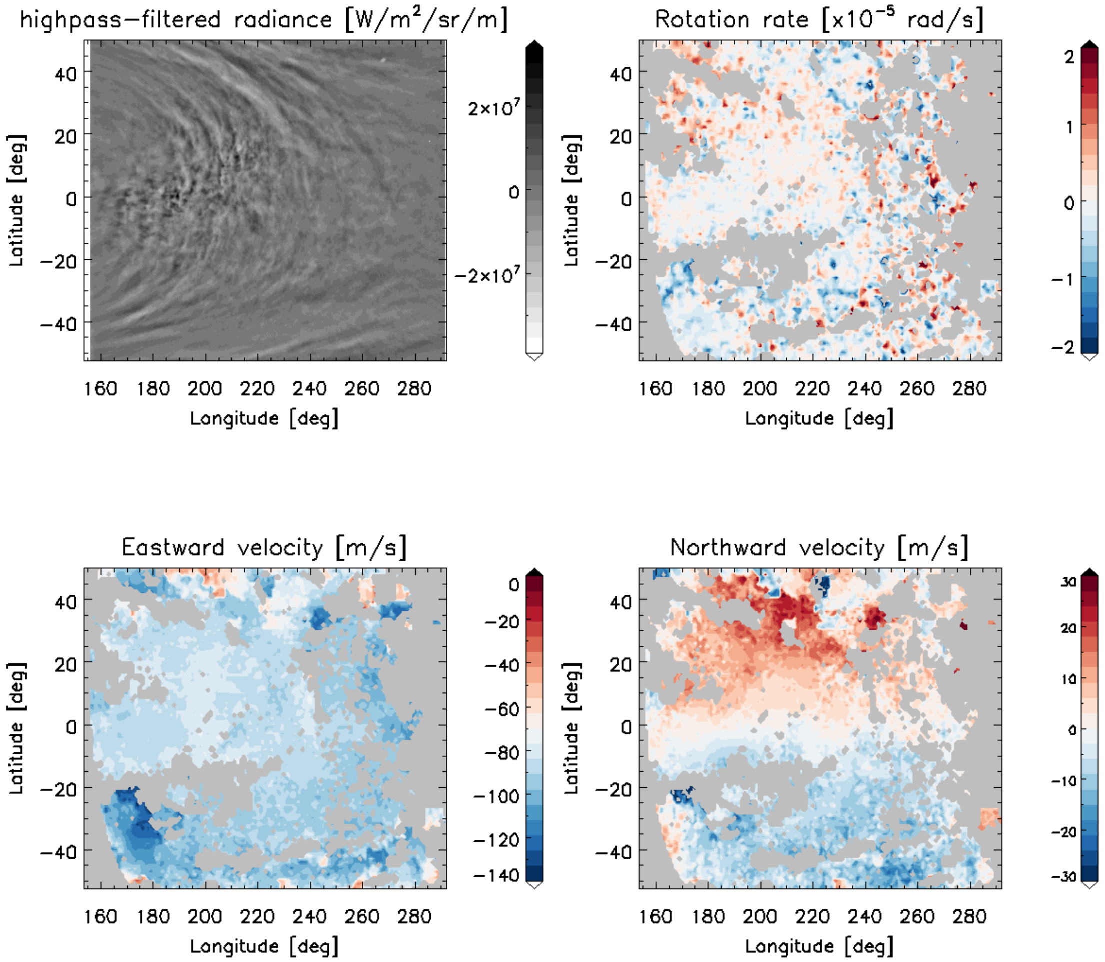

Figure 49. Same as Figure 39, but for the images taken at 03:04 and 05:04 on November 16, 2018.

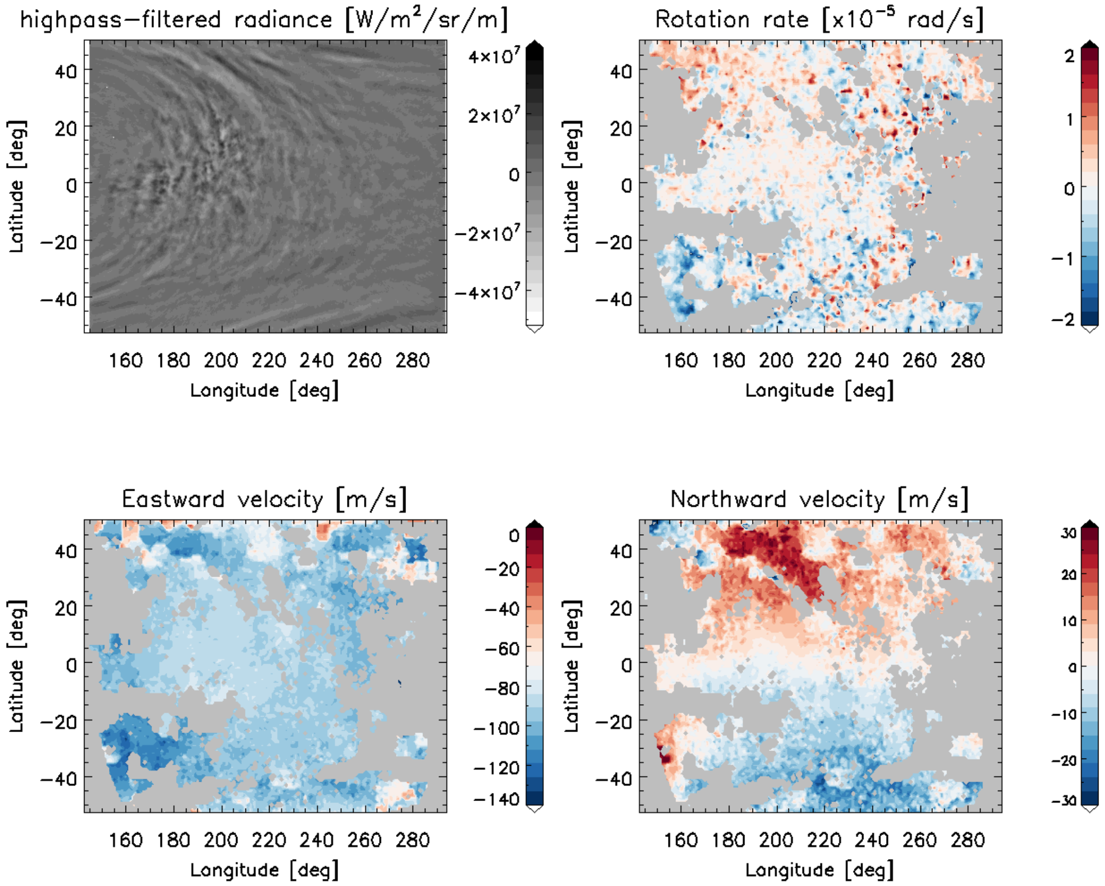

Figure 50. Same as Figure 39, but for the images taken at 07:04 and 09:04 on November 16, 2018.

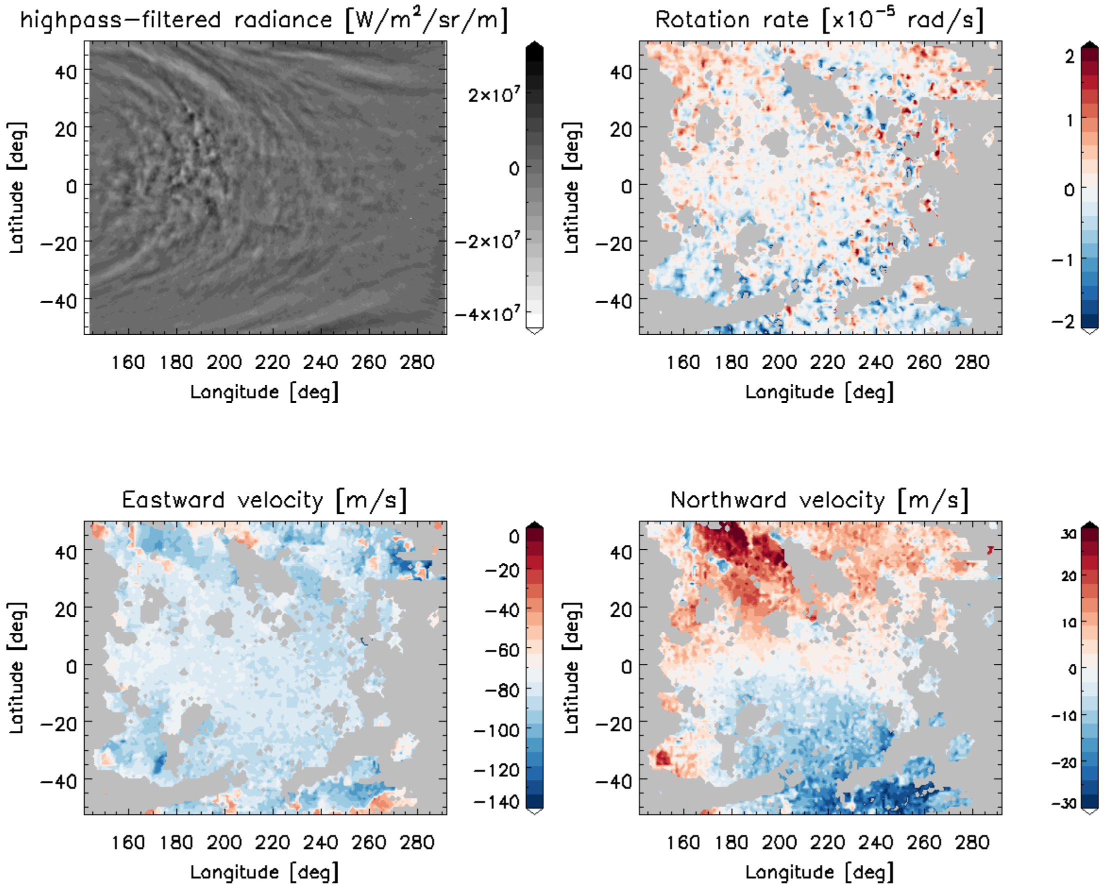

Figure 51. Same as Figure 39, but for the images taken at 11:04 and 13:04 on November 16, 2018.

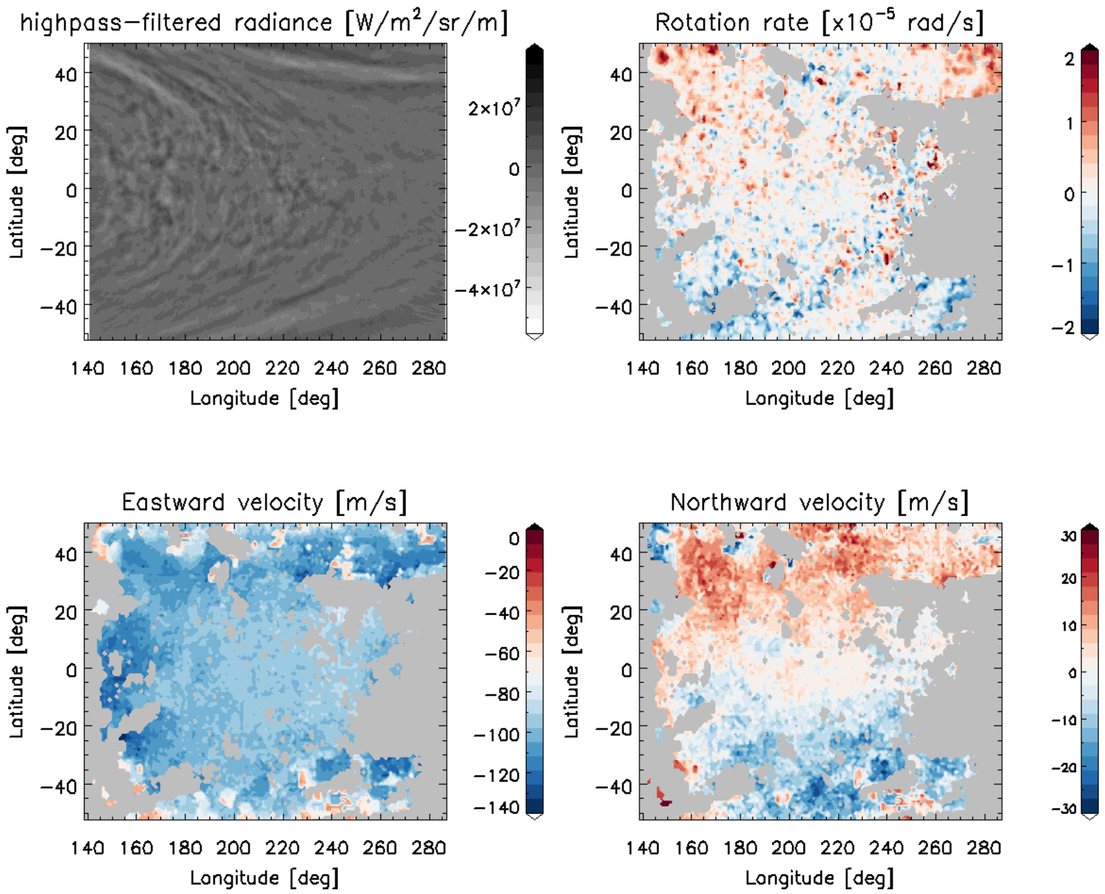

Figure 52. Same as Figure 39, but for the images taken at 15:04 and 17:04 on November 16, 2018.

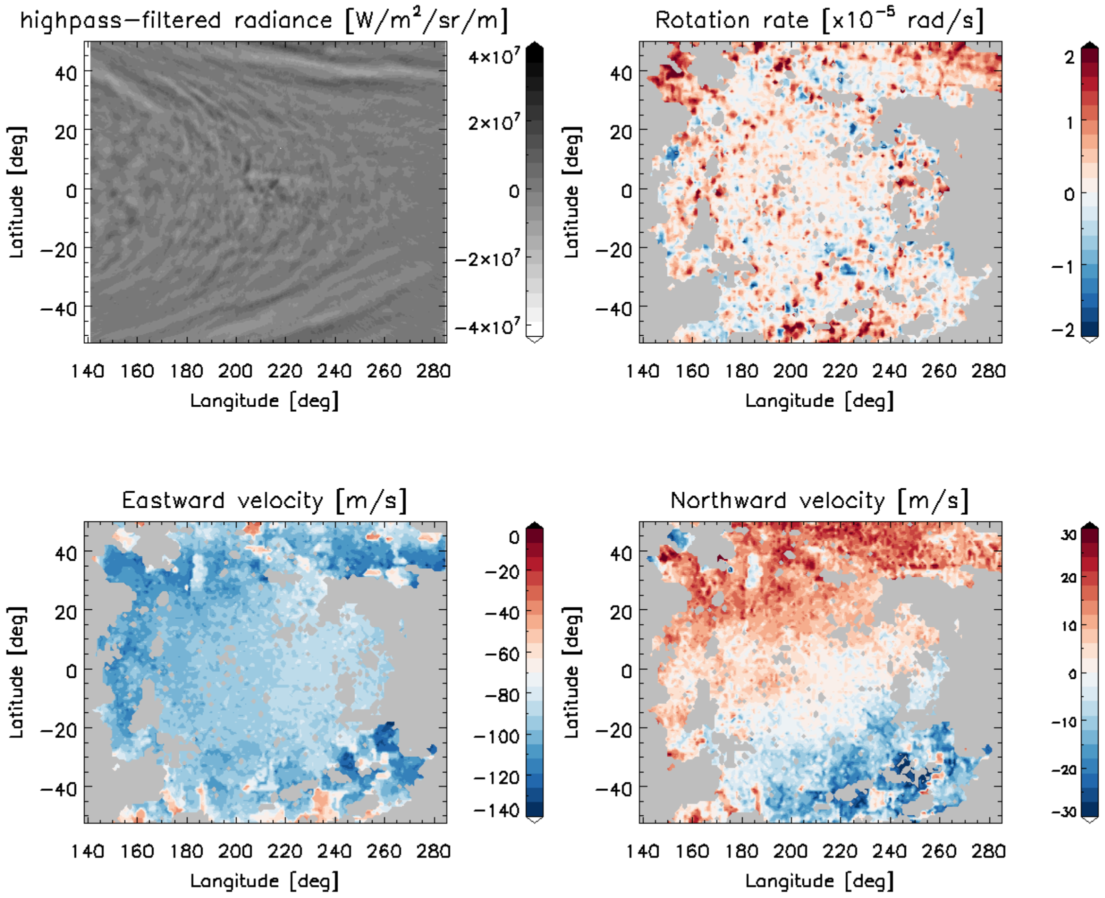

Figure 53. Same as Figure 39, but for the images taken at 19:04 and 21:04 on November 16, 2018.

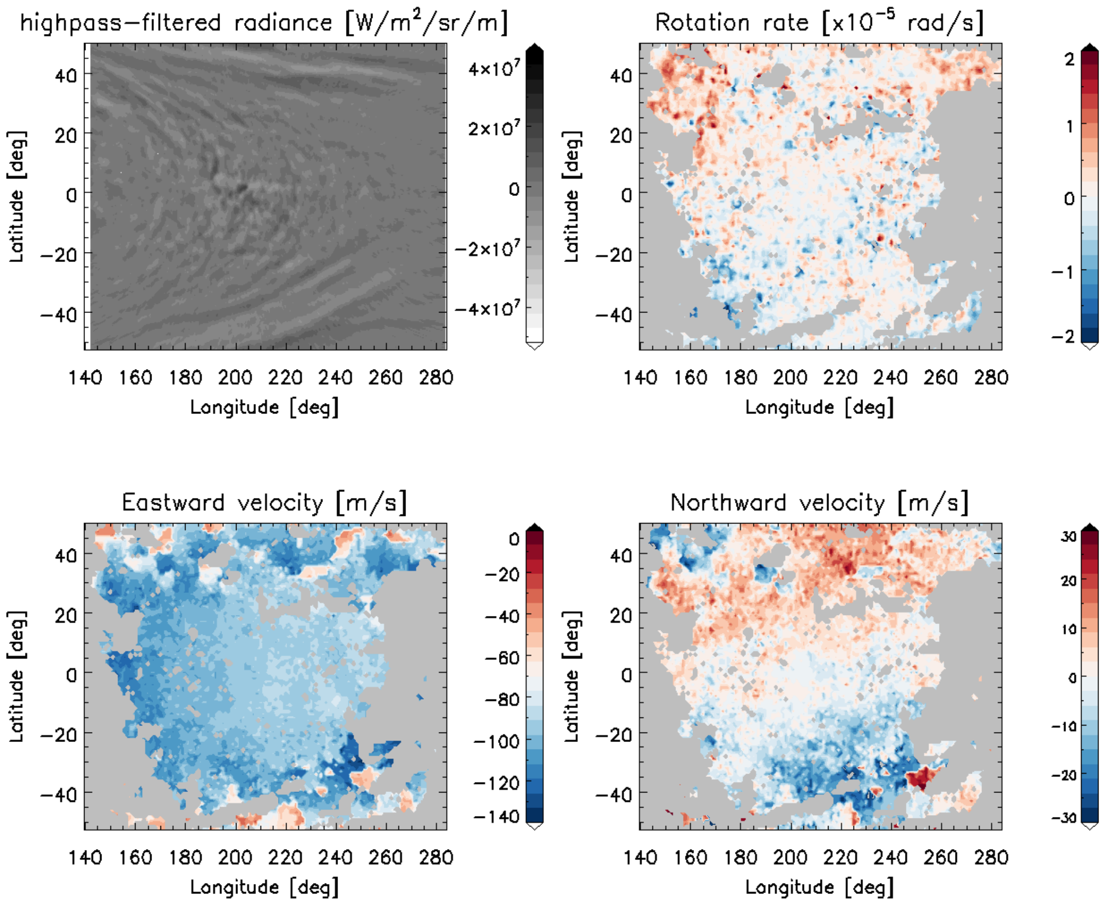

Figure 54. Same as Figure 39, but for the images taken at 23:04 on November 16, 2018 and 01:04 on November 17, 2018.

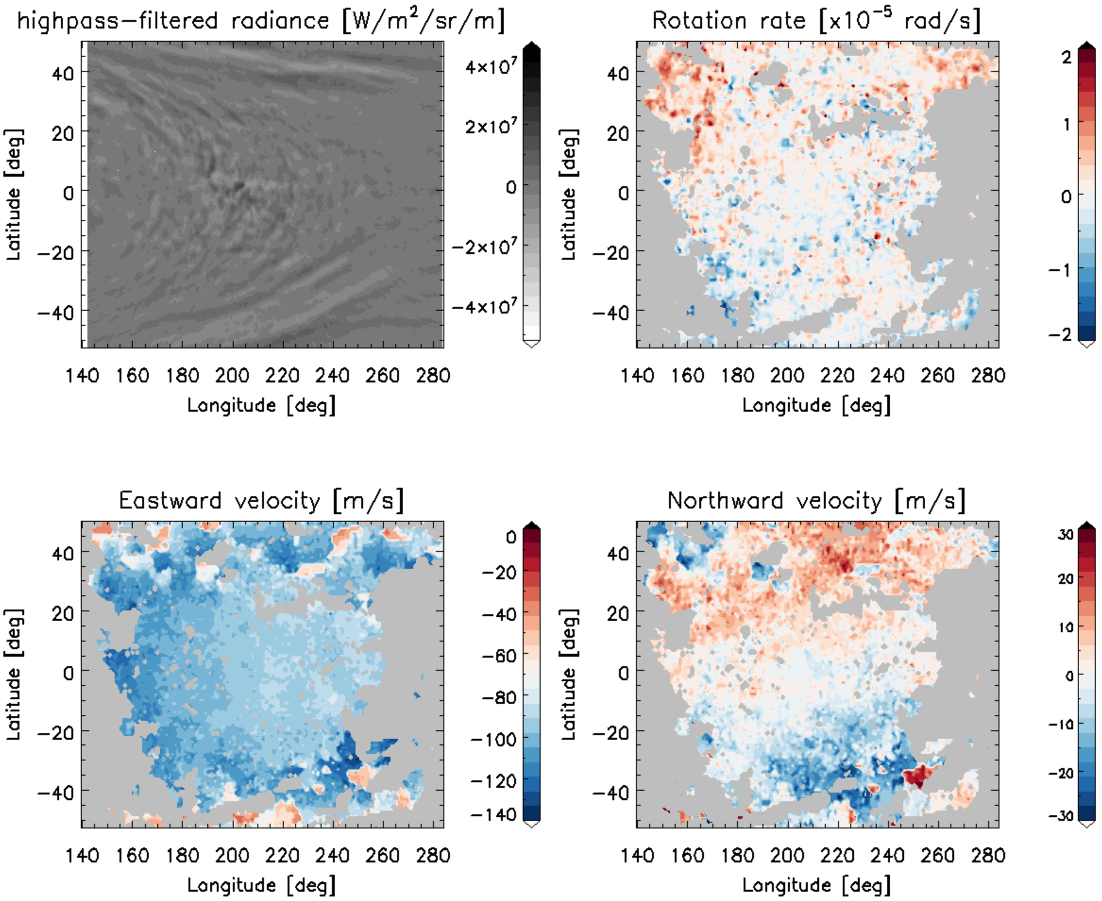

Figure 55. Same as Figure 39, but for the images taken at 03:04 and 05:04 on November 17, 2018.

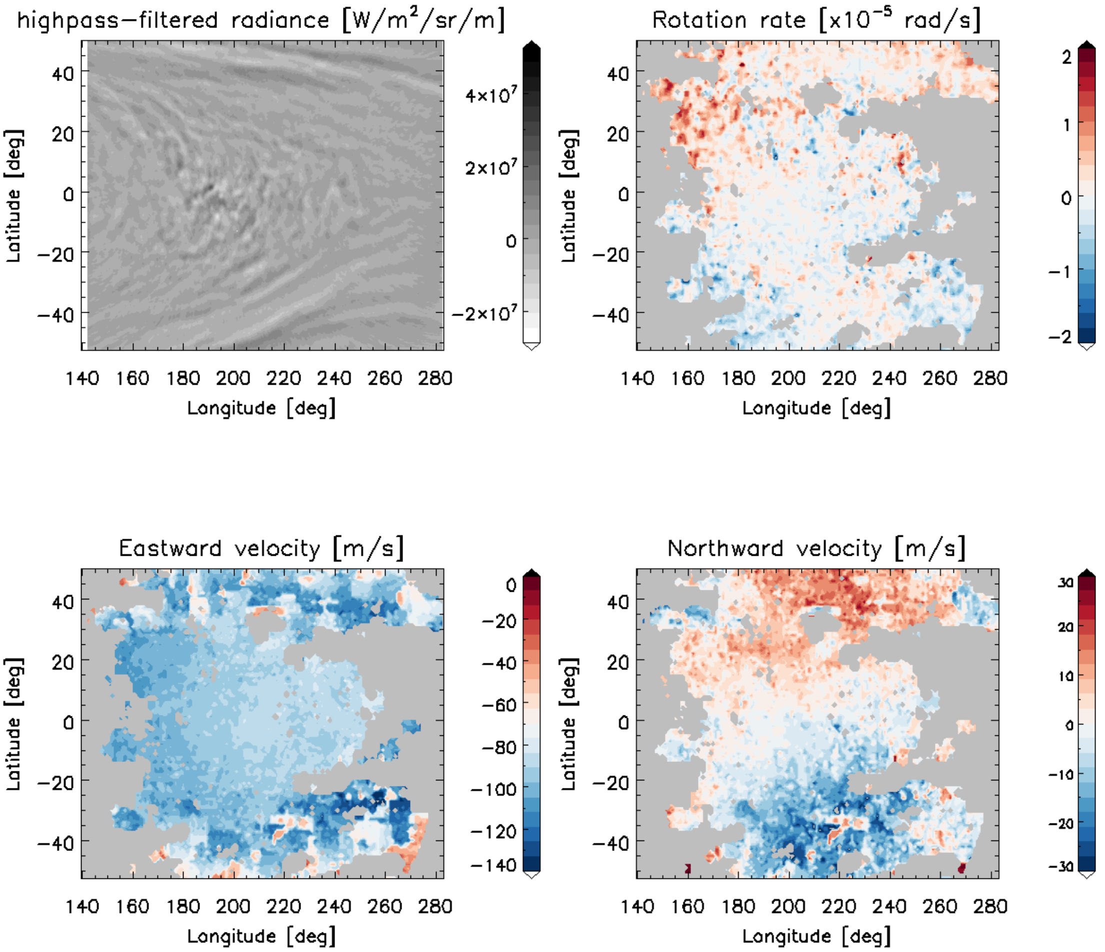

Figure 56. Same as Figure 39, but for the images taken at 07:04 and 09:04 on November 17, 2018.

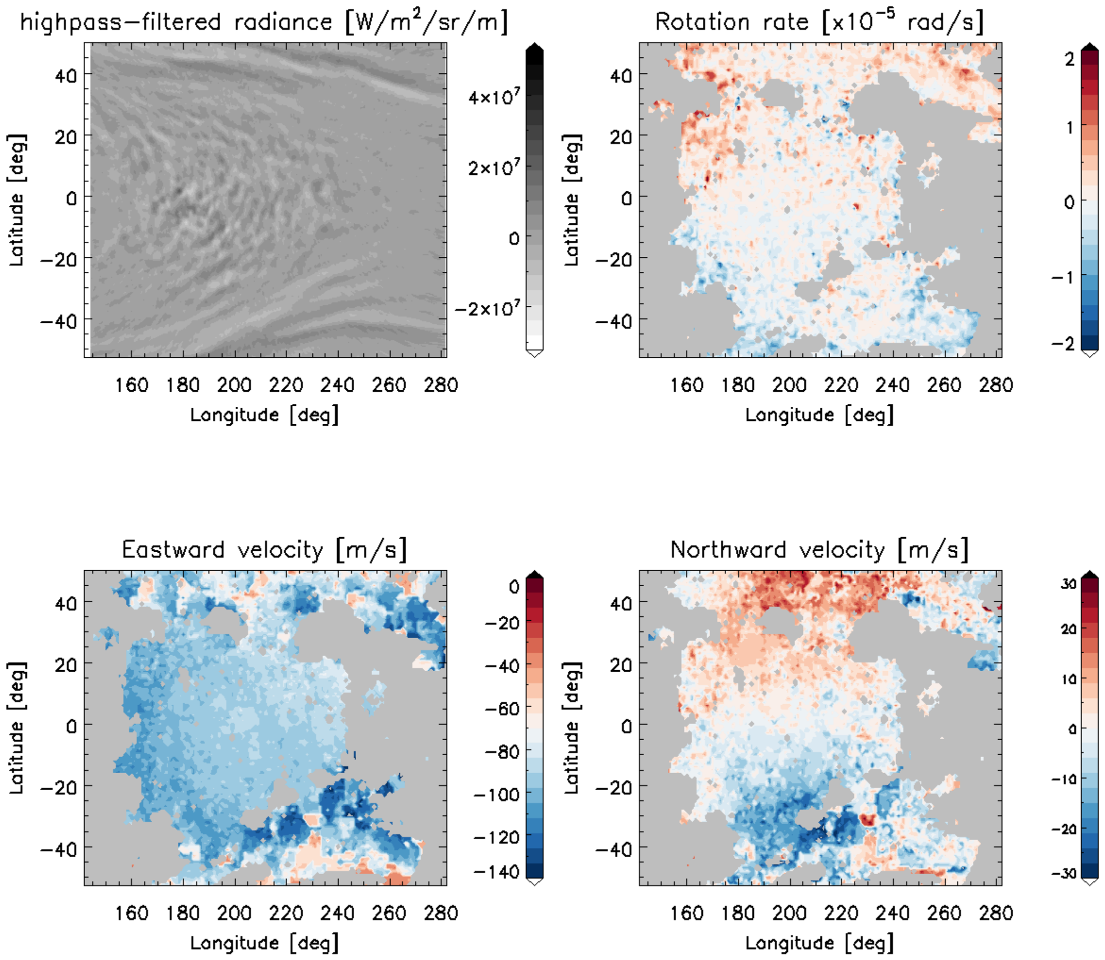

Figure 57. Same as Figure 39, but for the images taken at 11:04 and 13:04 on November 17, 2018.

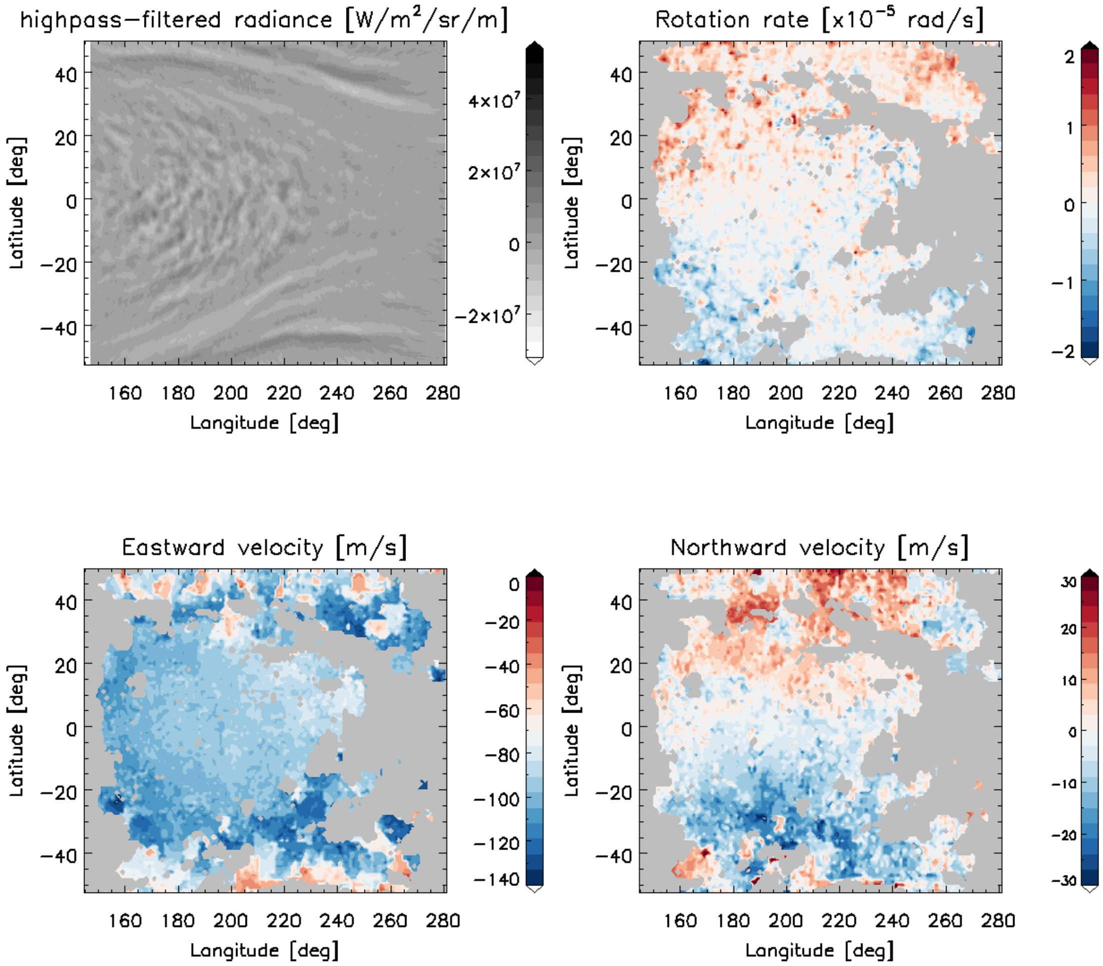

Figure 58. Same as Figure 39, but for the images taken at 15:04 and 17:04 on November 17, 2018.

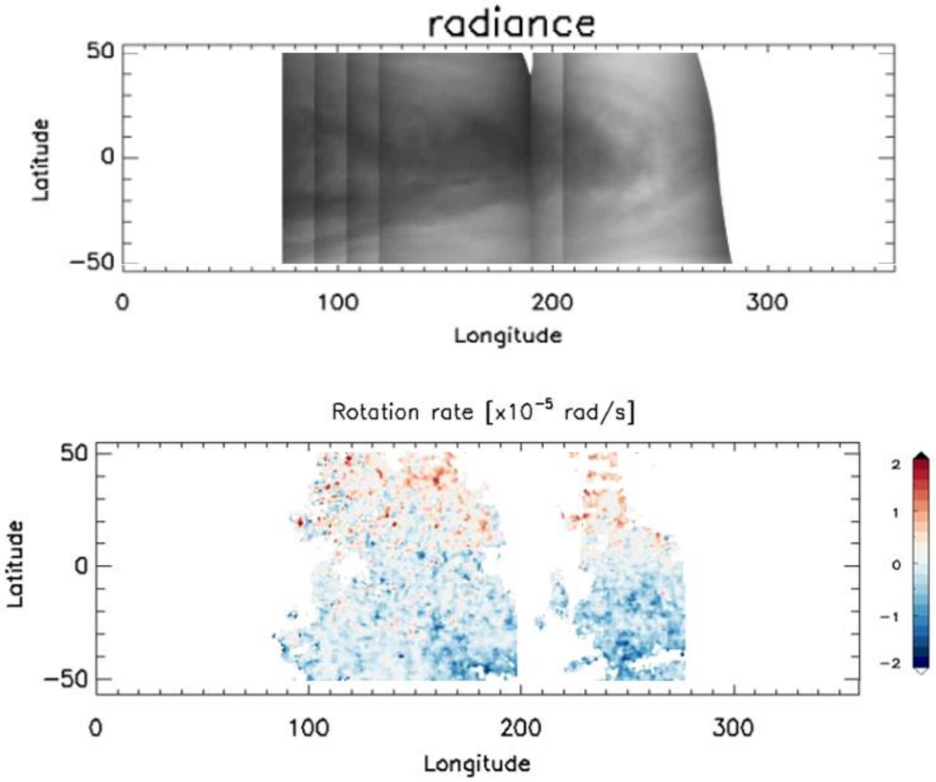

Figure 59. (top) Mosaics of ultraviolet images taken in 04:17 on August 3, 2016 to 17:17 on August 4, 2016 and (bottom) a mosaic of the rotation rate obtained for the same period.

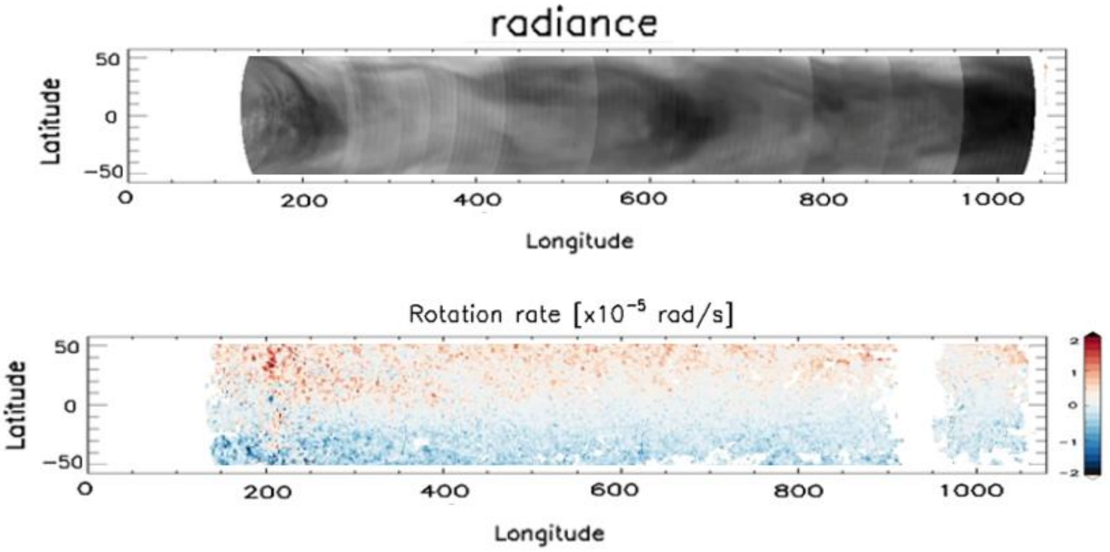

Figure 60. (top) Mosaics of ultraviolet images taken in 03:04 on November 16, 2018 to 03:04 on November 25, 2018 and (bottom) a mosaic of the rotation rate obtained for the same period.

5. Discussion

The discovery of small-scale vortices (~1° in latitude and logitude) on Jupiter in this study was made possible not only by the direct detection of rotation but also by the relatively small effective size of the tracking region. In the previous studies using cloud tracking, which revealed the multiple jet structure that is correlated with the cloud color's striped structure (e.g., Rogers 1995; Fletcher et al. 2020), the kinetic energy spectrum and rotational winds around the Great Red Spot (Galperin et al. 2014), the movement of clouds with a scale of about 1° was tracked. Since these studies considered only parallel movements of individual cloud features, the vortex scale that can be observed was larger than twice the size of the tracking region (Choi et al. 2007). In my study, the effective size of the tracking region is determined by the full width at half maximum of the Gaussian filter used in the two-dimensional FFT (section 4.1) and is about 0.8° × 0.8°. Moreover, since the rotation of the tracking region is directly measured in the proposed method, the minimum size of the vortices observed corresponds to this effective size.

The vortex chains observed by the new tracking method has an important implication for Jupiter's large-scale dynamics. Jupiter is known to have a prograde (eastward) jet stream with a maximum speed of about 100 m/s in the equatorial region at latitudes 10˚S-10˚N and alternating zonal jets at higher latitudes (Figure 61) (Porco et al. 2003; Galperin et al. 2014). Two models have been proposed to explain the strong zonal winds observed at Jupiter: the shallow model and the deep model (Kaspi et al. 2020). The shallow model has been developed to study the motion of thin atmospheric layers like those of the terrestrial planets. This model relies on the assumption that the fluid motion seen on the surface of Jupiter's cloud is shallow and is dynamically decoupled from the deep interior. The model suggests that the narrow zonal jets are generated by the upscale energy cascade in two-dimensional geostrophic turbulence powered by small-scale vortices that are produced by convection involving water vapor condensation (Ingersoll et al. 2004). However, this mechanism tends to produce a strong westward equatorial jet that is inconsistent with observations, although the direction of the equatorial wind seems to depend on the radiative relaxation schemes (Scott and Polvani 2008). Galperin et al. (2014) studied the kinetic energy spectrum of cloud-tracked winds and suggested that an inverse energy cascade of two-dimensional turbulence occurs to supply energy to the alternating zonal jets (Figure 62). The small-scale vortices detected in my study may comprise some part of the kinetic energy spectrum around the high-wavenumber end. The deep model was first proposed by Busse (1970) based on Taylor-Proudman theorem in fluid mechanics. In the model, convectively-generated Taylor columns aligned along the rotation axis are formed inside, and the nonlinear interaction of these columns can generate the equatorial jet and the high-latitude multiple jets (Busse 1970, 1976, 1983, 1994). Recent gravity measurements suggest that the jets seen on the cloud surface do not penetrate the whole planet but extend down to ~3000 km deep (Kaspi et al.2018). Schneider and Liu (2009) proposed a mixture of the shallow model and the deep model. They argued, based on numerical experiments, that vortices created in the equatorial region by internal convective heat flux excite Rossby waves, which propagate from the equatorial region to higher latitudes in a shallow layer. Since Rossby waves possess retrograde (westward) momentum, their propagation toward higher latitudes induces eastward acceleration of the equatorial atmosphere, thereby creating an equatorial jet. The jet structure extends to the interior as a Taylor column. Figure 63 shows the results of Jupiter's atmospheric simulation by Schneider and Liu (2009), indicating the existence of chains of vortex generation regions in the equatorial region (Figure 63b), that lead to generation of Rossby waves and the equatorial jet (Figure 63d). In my study, many small eddies were found to be distributed in the equatorial region similarly to the numerical simulation. The horizontal scale of the vortex is ~2000 km and typical magnitude of the vorticity is $2.0\text{-}5.0 \times 10^{-5}$ s^{-1} in the numerical model, while the size of the vortex is ~1000 km and the magnitude of the rotation rate is ~3.0×10^{-5} rad s^{-1} in my analysis. Considering that the rotation rate is 1/2 of the vorticity (Eq. 7), the observed quantities are comparable to those in the model. These similarities support the proposed mechanism, which have not been compared with observations. As described above, the vortex chains observed in this study may play key roles in the generation of zonal jets through wave excitation or inverse cascade of kinetic energy; these processes will occur in a shallow layer, being consistent with the shallow model. However, at the same time, the resultant jets can extend to deep levels along the rotation axis, following the concept of the deep model.

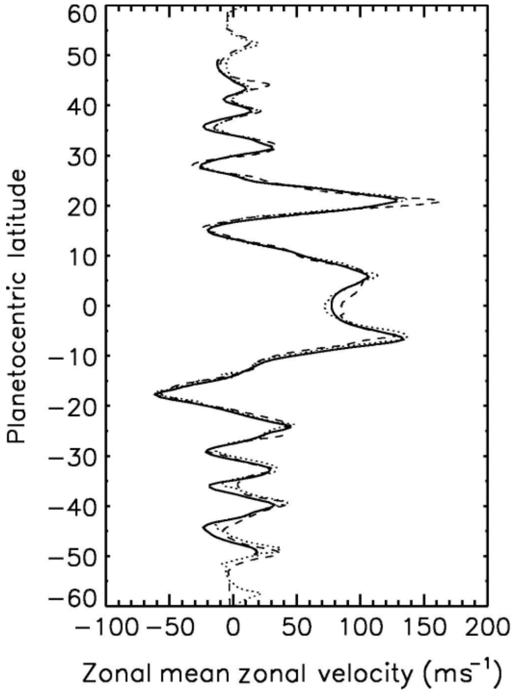

Figure 61. Zonal-mean zonal velocity at the cloud top of Jupiter obtained by cloud tracking (Galperin et al. 2014). Results by Galperin et al. (2014) (black), Poroco et al. (2003) (dotted) and Limaye (1986) (dashed).

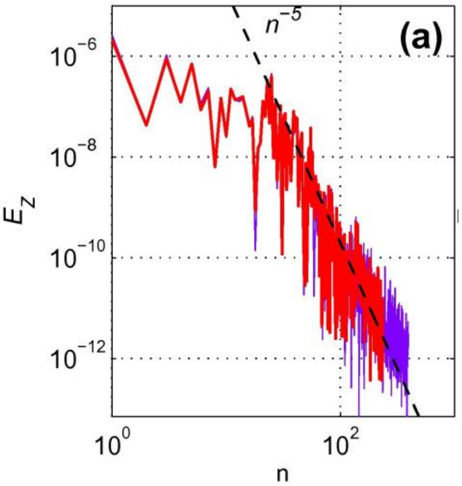

Figure 62. Zonal kinetic energy spectra of cloud-tracked winds of Jupiter (Galperin et al. 2014).

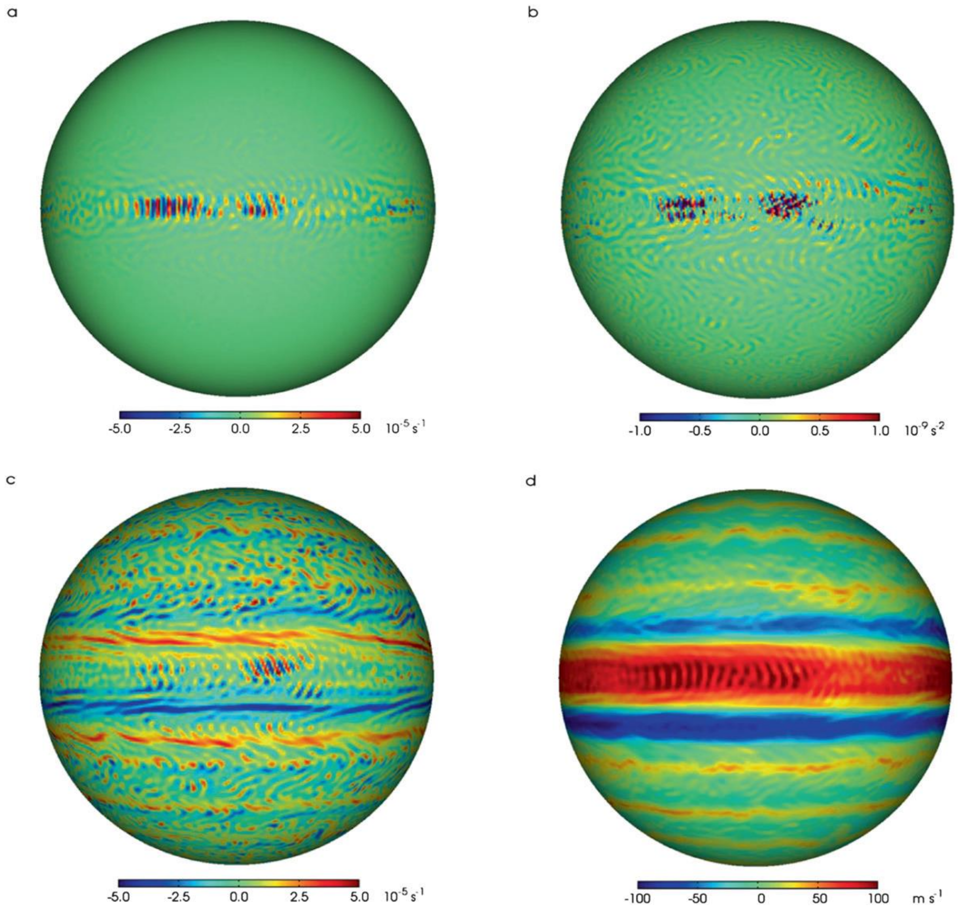

Figure 63. A snapshot of flow fields at 0.65 bar in a numerical simulation of Jupiter's atmosphere: (a) horizontal divergence, (b) Rossby wave source, (c) relative vorticity of horizontal flow, and (d) zonal velocity (Schneider and Liu 2009).

The new method was also applied to successive ultraviolet images of Venus taken by Akatsuki spacecraft. The obtained rotation distribution largely shows a reflection symmetry with respect to the equator such that anticlockwise rotation exists in the northern hemisphere and clockwise rotation exists in the southern hemisphere. This is attributed to the increase of the angular velocity of the mean zonal flow with latitude up to ~60° latitude in both hemispheres (Rossow et al. 1990), i.e., a positive vorticity in the northern hemisphere and a negative vorticity in the southern hemisphere. The rotational rate in the mid-latitude obtained in this study is $\sim 1.0 \times 10^{-5}$ rad s^{-1}, which is broadly consistent with the vorticity calculated from the cloud-tracked velocity (Travis 1978) and that from the thermal wind obtained from radio occultation temperatures (Piccialli et al. 2012).

The confirmation of the influence of the large-scale differential rotation on the local rotation of small-scale cloud patterns on Venus has an important implication for the influence of the background wind on the cloud morphology. Venus's cloud layer shows small-scale streaky features at mid-latitudes (Figure 64), and the origin of such cloud patterns is poorly understood (Rossow et al. 1980; Titov et al. 2012). Smith and Gierasch (1996) proposed that the streaky features at mid-latitudes are formed by the stretching of patchy clouds, which are presumably created by convection at low latitudes, by the latitudinal shear of the background zonal flow, but this scenario has not been confirmed by observations. Considering that the shearing motion of cloud patterns is observed as a local rotation in this method, the result suggests that the small-scale streaky features are created by the deformation of clouds by large-scale winds. This finding will help to understand the processes of cloud formation and material transport on Venus.

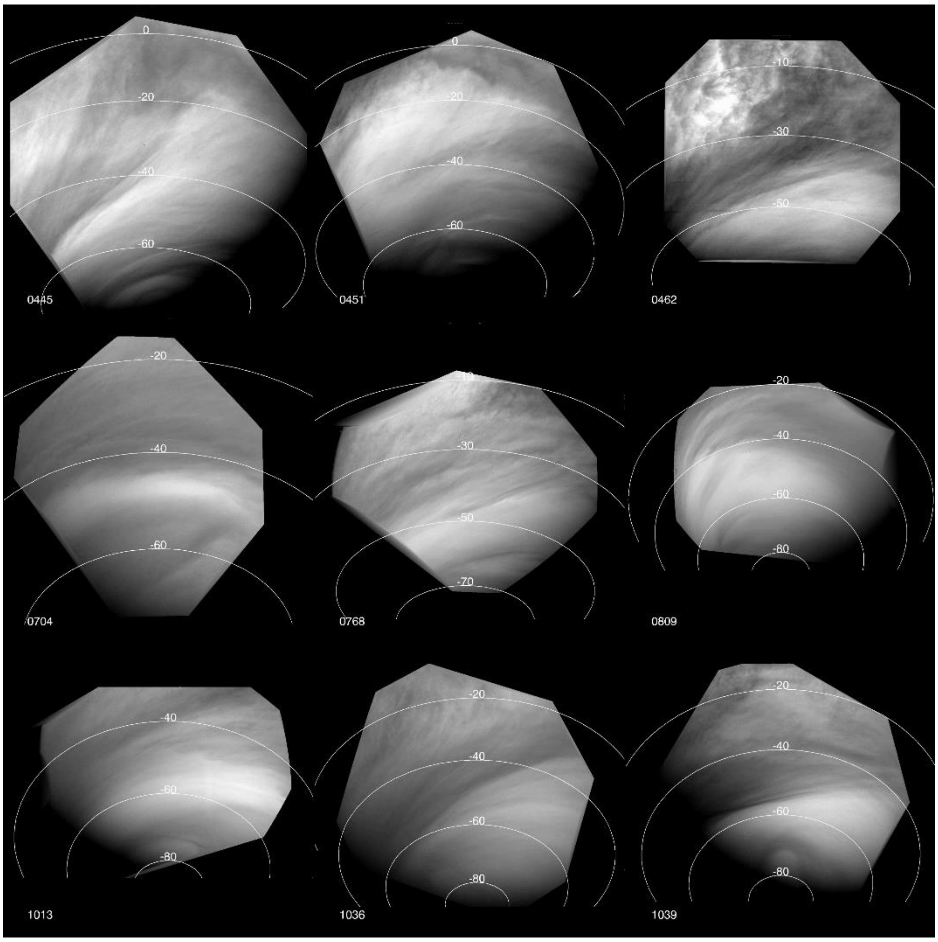

Figure 64. UV (365 nm) images of the mid-latitude of the southern hemisphere of Venus taken by VMC onboard Venus Express (Tiotv et al. 2012).

Typical amplitudes of rotation rate of small vortices are $\sim 1.0 \times 10^{-5}$ rad s^{-1} in Venus and $\sim 3.0 \times 10^{-5}$ rad s^{-1} in Jupiter. The difference in the vortex distribution between Jupiter and Venus might be attributed to the difference in the planetary parameters; the horizontal scale of the vortices is determined by the Rossby number such that larger Rossby numbers favor larger eddies (Williams 1988), and the Rossby number basically increases with decreasing the Coriolis parameter (rotation rate). Jupiter rotates at high speed (~10 h), while Venus rotates at low speed (243 days), so the Coriolis force is large on Jupiter and small on Venus. This means that the scale of the horizontal vortex tends to be much smaller than the planetary scale on Jupiter and is as large as the planetary scale on Venus. Therefore, it is anticipated that the vortex motion at small scales is predominant on Jupiter and inactive on Venus. It is also expected that convective activity driven in the deep atmosphere can reach the cloud top on Jupiter, while convective activity does not reach the cloud top on Venus because the region around the cloud top is stably stratified (Imamura et al. 2014). Therefore, horizontal divergence due to convective activity can create small vortices on Jupiter, while the mechanism does not work on Venus.

6. Summary

In this study, I applied the rotation invariant phase-only correlation method to fluid motions for the first time. Whereas the conventional cross correlation method or the phase only correlation method can only track parallel movements of characteristic patterns, the rotation invariant phase-only correlation method can also track rotations of the patterns. In the previous studies, the rotational motion in a fluid has been measured using the vorticity calculated from the parallel translation vectors obtained by cloud tracking; on the other hand, using this method, rotational motions can be obtained directly from the local rotation of the patterns.

I performed some tests using simulated images assuming rigid body rotation, irrotational vortex, and sinusoidal disturbances in the latitudinal and longitudinal directions. It was demonstrated that this method is effective in detecting small scale vortex motions that are difficult to derive from the velocity field. In the case of a large-scale rotating motion in which the spatial scale of the disturbance is larger than the size of the tracking area, the rotation rate can be obtained accurately. When the scale of the velocity structure is smaller than the size of the tracking region, the rotation rate is underestimated, while the spatial pattern of the rotation rate can still be obtained.

The method was first applied to successive images of Jupiter taken by Cassini spacecraft. As a result, the band structure peculiar to Jupiter was confirmed in the velocity field and small vortices were found to be connected in the equatorial region in the zonal direction. The size of the vortex is about 1° (about 1250 km) in latitude and longitude direction. It is found that the vortex motion is not active everywhere but distributed in regions where streak patterns are less prominent in cloud images. The series of vortices observed in this study supports the model proposed by Schneider and Liu (2009).

The new method was also applied to successive images of Venus taken by Akatsuki spacecraft. As a result, the obtained rotation distribution largely shows a reflection symmetry with respect to the equator. This is attributed to the increase of the angular velocity of the mean zonal flow with latitude up to ~60° latitude in both hemispheres. This is a result that suggests that the large-scale differential rotation influences the local rotation of small-scale cloud patterns and the small-scale streaky features are created by the deformation of clouds by large-scale winds. This result is consistent with the suggestion by Smith and Gierasch (1996), who argued that the streaky cloud pattern is created by the deformation of clouds by the background wind shear.

As compared to the observations of small-scale eddies by cloud tracking conducted so far (e.g. Galperin et al. 2014; Garate-Lopez et al. 2015), the newly-developed method has extracted even smaller scale eddies, thereby extending the spectral coverage. The method has enabled investigation of the interaction between different scales in a wider wavelength range. The method would also enable studies of mesoscale weather systems such as deep convection and also studies of upward energy cascade from small-scale convective storms to planetary scale motions in planetary atmospheres.

Acknowledgments

The author would like to thank Professor Takeshi Imamura for his great assistance for this study. His comments, suggestions and encouragement were a great help to the author. Thanks to Professor Ichiro Yoshikawa, Lecturer Kazuo Yoshioka and other members of astrobiology group in the University of Tokyo for insightful comments and encouragement. This study was supported by JSPS Grant-in-Aid for JSPS Fellows Grant Number JP 18J12011.

References

Aoki, T., Ito, K., Shibahara, T., Nagashima, S., 2007. High-Accuracy Machine Vision Using Phase-Only Correlation. IEICE ESS FUNDAMENTALS REVIEW 1, 30–40. doi:10.1587/essfr.1.1_30

Beebe, R.F., Ingersoll, A.P., Hunt, G.E., Mitchell, J.L., Müller, J.-P., 1980. Measurements of wind vectors, eddy momentum transports, and energy conversions in Jupiter's atmosphere from Voyager 1 images. Geophysical Research Letters 7, 1–4. doi:10.1029/GL007i001p00001

Belton, M.J.S., Gierasch, P.J., Smith, M.D., Helfenstein, P., Schinder, P.J., Pollack, J.B., Rages, K.A., Ingersoll, A.P., Klaasen, K.P., Veverka, J., Anger, C.D., Carr, M.H., Chapman, C.R., Davies, M.E., Fanale, F.P., Greeley, R., Greenberg, R., III, J.W.H., Morrison, D., Neukum, G., Pilcher, C.B., 1991. Images from Galileo of the Venus Cloud Deck. Science 253, 1531–1536. doi:10.1126/science.253.5027.1531

Bougher, S.W., Hunten, D.M., Phillips, R.J., 1997. Venus II--geology, Geophysics, Atmosphere, and Solar Wind Environment. University of Arizona Press.

Busse, F.H., 1994. Convection driven zonal flows and vortices in the major planets. Chaos: An Interdisciplinary Journal of Nonlinear Science 4, 123–134.

Busse, F.H., 1983. A model of mean zonal flows in the major planets. Geophysical & Astrophysical Fluid Dynamics 23, 153–174.

Busse, F.H., 1976. A simple model of convection in the Jovian atmosphere. Icarus 29, 255–260.

Busse, F.H., 1970. Thermal instabilities in rapidly rotating systems. Journal of Fluid Mechanics 44, 441–460.

Choi, D.S., Banfield, D., Gierasch, P., Showman, A.P., 2007. Velocity and vorticity measurements of Jupiter's Great Red Spot using automated cloud feature tracking. Icarus 188, 35–46. doi:10.1016/j.icarus.2006.10.037

Dowling, T.E., Ingersoll, A.P., 1988. Potential vorticity and layer thickness variations in the flow around Jupiter's Great Red Spot and White Oval BC. Journal of the atmospheric sciences 45, 1380–1396.

Fletcher, L.N., Kaspi, Y., Guillot, T., Showman, A.P., 2020. How Well Do We Understand the Belt/Zone Circulation of Giant Planet Atmospheres? Space Science Reviews 216, 30. doi:10.1007/s11214-019-0631-9

Galperin, B., Young, R.M.B., Sukoriansky, S., Dikovskaya, N., Read, P.L., Lancaster, A.J., Armstrong, D., 2014. Cassini observations reveal a regime of zonostrophic macroturbulence on Jupiter. Icarus 229, 295–320. doi:10.1016/j.icarus.2013.08.030

Garate-Lopez, I., Garc??a Mu??oz, A., Hueso, R., S??nchez-Lavega, A., 2015. Instantaneous three-dimensional thermal structure of the South Polar Vortex of Venus. Icarus 245, 16–31. doi:10.1016/j.icarus.2014.09.030

Horinouchi, T., Kouyama, T., Lee, Y.J., Murakami, S. ya, Ogohara, K., Takagi, M., Imamura, T., Nakajima, K., Peralta, J., Yamazaki, A., Yamada, M., Watanabe, S., 2018. Mean winds at the cloud top of Venus obtained from two-wavelength UV imaging by Akatsuki. Earth, Planets and Space 70. doi:10.1186/s40623-017-0775-3

Horinouchi, T., Murakami, S., Satoh, T., Peralta, J., Ogohara, K., Kouyama, T., Imamura, T., Kashimura, H., Limaye, S.S., Mcgouldrick, K., 2017. Equatorial jet in the lower to middle cloud layer of Venus revealed by Akatsuki 10. doi:10.1038/NGEO3016

Hueso, R., Peralta, J., Sánchez-Lavega, A., 2012. Assessing the long-term variability of Venus winds at cloud level from VIRTIS-Venus Express. Icarus 217, 585–598. doi:10.1016/j.icarus.2011.04.020

Ikegawa, S., Horinouchi, T., 2016. Improved automatic estimation of winds at the cloud top of Venus using superposition of cross-correlation surfaces. Icarus 271, 98–119. doi:10.1016/j.icarus.2016.01.018

Imai, M., Kouyama, T., Takahashi, Y., Yamazaki, A., Watanabe, S., Yamada, M., Imamura, T., Satoh, T., Nakamura, M., Murakami, S., Ogohara, K., Horinouchi, T., 2019. Planetary-Scale Variations in Winds and UV Brightness at the Venusian Cloud Top: Periodicity and Temporal Evolution. Journal of Geophysical Research: Planets 124, 2635–2659. doi:10.1029/2019JE006065

Imamura, T., Higuchi, T., Maejima, Y., Takagi, M., Sugimoto, N., Ikeda, K., Ando, H., 2014. Inverse insolation dependence of Venus' cloud-level convection. Icarus 228, 181–188. doi:https://doi.org/10.1016/j.icarus.2013.10.012

Ingersoll, A.P., Beebe, R.F., Collins, S.A., Hunt, G.E., Mitchell, J.L., Muller, P., Smith, B.A., Terrile, R.J., 1979. Zonal velocity and texture in the jovian atmosphere inferred from Voyager images. Nature 280, 773–775. doi:10.1038/280773a0

Ingersoll, A.P., Beebe, R.F., Mitchell, J.L., Garneau, G.W., Yagi, G.M., Müller, J.-P., 1981. Interaction of eddies and mean zonal flow on Jupiter as inferred from Voyager 1 and 2 images. Journal of Geophysical Research: Space Physics 86, 8733–8743. doi:10.1029/JA086iA10p08733

Ingersoll, A.P., Dowling, T.E., Gierasch, P.J., Orton, G.S., Read, P.L., Sánchez-Lavega, A., Showman, A.P., Simon-Miller, A.A., Vasavada, A.R., 2004. Dynamics of Jupiter's atmosphere.

Kaspi, Y., Galanti, E., Hubbard, W.B., Stevenson, D.J., Bolton, S.J., Iess, L., Guillot, T., Bloxham, J., Connerney, J.E.P., Cao, H., 2018. Jupiter's atmospheric jet streams extend thousands of kilometres deep. Nature 555, 223–226.

Kaspi, Y., Galanti, E., Showman, A.P., Stevenson, D.J., Guillot, T., Iess, L., Bolton, S.J., 2020. Comparison of the Deep Atmospheric Dynamics of Jupiter and Saturn in Light of the Juno and Cassini Gravity Measurements. Space Science Reviews 216, 84. doi:10.1007/s11214-020-00705-7

Khatuntsev, I. V., Patsaeva, M. V., Titov, D. V., Ignatiev, N.I., Turin, A. V., Limaye, S.S., Markiewicz, W.J., Almeida, M., Roatsch, T., Moissl, R., 2013. Cloud level winds from the Venus Express Monitoring Camera imaging. Icarus 226, 140–158. doi:10.1016/j.icarus.2013.05.018

Kouyama, T., Imamura, T., Nakamura, M., Satoh, T., Futaana, Y., 2013. Long-term variation in the cloud-tracked zonal velocities at the cloud top of Venus deduced from Venus Express VMC images. Journal of Geophysical Research E: Planets 118, 37–46. doi:10.1029/2011JE004013

Kouyama, T., Imamura, T., Nakamura, M., Satoh, T., Futaana, Y., 2012. Horizontal structure of planetary-scale waves at the cloud top of Venus deduced from Galileo SSI images with an improved cloud-tracking technique. Planetary and Space Science 60, 207–216. doi:10.1016/j.pss.2011.08.008

Laing, A., Evans, J.L., 2011. Introduction to Tropical Meteorology. The COMET Program.

Limaye, S.S., 2007. Venus atmospheric circulation: Known and unknown. Advances in Space Research 10, 91–101. doi:10.1016/0273-1177(90)90170-5

Limaye, S.S., 1986. Jupiter: New estimates of the mean zonal flow at the cloud level. Icarus 65, 335–352. doi:10.1016/0019-1035(86)90142-9

Limaye, S.S., Suomi, V.E., 1981. Cloud Motions on Venus: Global Structure and Organization. Journal of the Atmospheric Sciences 38, 1220–1235. doi:10.1175/1520-0469(1981)038<1220:cmovgs>2.0.co;2

Lomb, N.R., 1976. Least-squares frequency analysis of unequally spaced data. Astrophysics and Space Science 39, 447–462. doi:10.1007/BF00648343

Mitchell, J.L., Beebe, R.F., Ingersoll, A.P., Garneau, G.W., 1981. Flow fields within Jupiter's Great Red Spot and white oval BC. Journal of Geophysical Research: Space Physics 86, 8751–8757.

Nastrom, G.D., Gage, K.S., 1985. A climatology of atmospheric wavenumber spectra of wind and temperature observed by commercial aircraft. Journal of the Atmospheric Sciences 42, 950–960. doi:10.1175/1520-0469(1985)042<0950:ACOAWS>2.0.CO;2

Nikaido, A., Ito, K., Aoki, T., Kosuge, E., Kawamata, R., 2006. A dental radiograph registration algorithm using phase-based image matching for human identification, in: 2006 International Symposium on Intelligent Signal Processing and Communications, ISPACS'06. pp. 375–378. doi:10.1109/ISPACS.2006.364907

Ogohara, K., Takagi, M., Murakami, S. ya, Horinouchi, T., Yamada, M., Kouyama, T., Hashimoto, G.L., Imamura, T., Yamamoto, Y., Kashimura, H., Hirata, N., Sato, N., Yamazaki, A., Satoh, T., Iwagami, N., Taguchi, M., Watanabe, S., Sato, T.M., Ohtsuki, S., Fukuhara, T., Futaguchi, M., Sakanoi, T., Kameda, S., Sugiyama, K. ichiro, Ando, H., Lee, Y.J., Nakamura, M., Suzuki, M., Hirose, C., Ishii, N., Abe, T., 2017. Overview of Akatsuki data products: definition of data levels, method and accuracy of geometric correction. Earth, Planets and Space 69. doi:10.1186/s40623-017-0749-5

Oyama, R., Wada, A., Sawada, M., 2016. Intensification of Typhoon Danas (1324) Captured by MTSAT upper tropospheric atmospheric motion vectors. Scientific Online Letters on the Atmosphere 12, 135–139. doi:10.2151/sola.2016-029

Peralta, J., Muto, K., Hueso, R., Horinouchi, T., Sánchez-Lavega, A., Murakami, S., Machado, P., Young, E.F., Lee, Y.J., Kouyama, T., Sagawa, H., McGouldrick, K., Satoh, T., Imamura, T., Limaye, S.S., Sato, T.M., Ogohara, K., Nakamura, M., Luz, D., 2018. Nightside Winds at the Lower Clouds of Venus with Akatsuki /IR2: Longitudinal, Local Time, and Decadal Variations from Comparison with Previous Measurements. The Astrophysical Journal Supplement Series 239, 29. doi:10.3847/1538-4365/aae844

Piccialli, A., Tellmann, S., Titov, D. V., Limaye, S.S., Khatuntsev, I. V., Pätzold, M., Häusler, B., 2012. Dynamical properties of the Venus mesosphere from the radio-occultation experiment VeRa onboard Venus Express. Icarus 217, 669–681. doi:10.1016/j.icarus.2011.07.016

Porco, C.C., West, R.A., McEwen, A., Del Genio, A.D., Ingersoll, A.P., Thomas, P., Squyres, S., Dones, L., Murray, C.D., Johnson, T. V, 2003. Cassini imaging of Jupiter's atmosphere, satellites, and rings. Science 299, 1541–1547.

Rogers, J.H., 1995. The giant planet Jupiter. Cambridge University Press.

Rossow, W.B., Del Genio, A.D., Eichler, T., 1990. Cloud-tracked winds from Pioneer Venus OCPP images. Journal of the Atmospheric Sciences. doi:10.1175/1520-0469(1990)047

Scargle, J.D., 1982. Studies in astronomical time series analysis. II - Statistical aspects of spectral analysis of unevenly spaced data. The Astrophysical Journal 263, 835–853. doi:10.1086/160554

Schneider, T., Liu, J., 2009. Formation of jets and equatorial superrotation on Jupiter. Journal of the Atmospheric Sciences 66, 579–601. doi:10.1175/2008JAS2798.1

Schubert, G., Covey, C., Genio, A. Del, Elson, L.S., Keating, G., Seiff, A., Young, R.E., Apt, J., Counselman, C.C.I., Kliore, A.J., Limaye, S.S., Revercomb, H.E., Sromovsky, L.A., Suomi, V.E., Taylor, F., Woo, R., von Zahn, U., 1980. Structure and Circulation of the Venus Atmosphere. Journal of Geophysical Research: Space Physics 85, 8007–8025. doi:http://dx.doi.org/10.1029/JA085iA13p08007

Scott, R.K., Polvani, L.M., 2008. Equatorial superrotation in shallow atmospheres. Geophysical Research Letters 35.

Smith, M.D., Gierasch, P.J., 1996. Global-scale winds at the Venus cloud-top inferred from cloud streak orientations. Icarus 123, 313–323.

Titov, D. V., Markiewicz, W.J., Ignatiev, N.I., Song, L., Limaye, S.S., Sanchez-Lavega, A., Hesemann, J., Almeida, M., Roatsch, T., Matz, K.D., Scholten, F., Crisp, D., Esposito, L.W., Hviid, S.F., Jaumann, R., Keller, H.U., Moissl, R., 2012. Morphology of the cloud tops as observed by the Venus Express Monitoring Camera. Icarus 217, 682–701. doi:10.1016/j.icarus.2011.06.020

Travis, L.D., 1978. Nature of the Atmospheric Dynamics on Venus from Power Spectrum Analysis of Mariner 10 Images. Journal of the Atmospheric Sciences 35, 1584–1595. doi:10.1175/1520-0469(1978)035<1584:NOTADO>2.0.CO;2

Williams, G.P., 1988. The dynamical range of global circulations—I. Climate Dynamics 2, 205–260. doi:10.1007/BF01371320

Williams, G.P., 1978. Planetary circulations: 1. Barotropic representation of Jovian and terrestrial turbulence. Journal of the Atmospheric Sciences 35, 1399–1426.